ΕΘΝΙΚΟ ΜΕΤΣΟΒΙΟ ΠΟΛΥΤΕΧΝΕΙΟ

ΣΧΟΛΗ ΕΦΑΡΜΟΣΜΕΝΩΝ ΜΑΘΗΜΑΤΙΚΩΝ ΚΑΙ

ΦΥΣΙΚΩΝ ΕΠΙΣΤΗΜΩΝ

ΤΟΜΕΑΣ ΦΥΣΙΚΗΣ

ΔΙΠΛΩΜΑΤΙΚΗ ΕΡΓΑΣΙΑ

ΤΕΧΝΟΛΟΓΙΑ ΟΡΓΑΝΙΚΩΝ ΦΩΤΟΒΟΛΤΑΪΚΩΝ: ΑΝΑΠΤΥΞΗ ΗΛΙΑΚΩΝ ΚΥΨΕΛΩΝ ΒΑΣΙΣΜΕΝΩΝ ΣΕ ΕΤΕΡΟΔΟΜΕΣ ΘΕΙΟΦΑΙΝΕΙΟΥ-ΦΟΥΛΛΕΡΕΝΙΟΥ (α-6T/C_{60})

ORGANIC PHOTOVOLTAIC TECHNOLOGY: DEVELOPMENT OF ORGANIC SOLAR CELLS BASED ON THIOPHENE-FULLERENE (α-6T/C_{60}) HETEROJUNCTIONS

Κωνσταντίνος Δεσποτέλης

Επιβλέπουσα: Επίκουρη Καθηγήτρια ΕΜΠ Δρ. Δήμητρα Παπαδημητρίου

Αθήνα, Ιούνιος 2013

ΕΘΝΙΚΟ ΜΕΤΣΟΒΙΟ ΠΟΛΥΤΕΧΝΕΙΟ
ΣΧΟΛΗ ΕΦΑΡΜΟΣΜΕΝΩΝ ΜΑΘΗΜΑΤΙΚΩΝ ΚΑΙ ΦΥΣΙΚΩΝ ΕΠΙΣΤΗΜΩΝ
ΤΟΜΕΑΣ ΦΥΣΙΚΗΣ

ΔΙΠΛΩΜΑΤΙΚΗ ΕΡΓΑΣΙΑ
DIPLOMA-THESIS

ΤΕΧΝΟΛΟΓΙΑ ΟΡΓΑΝΙΚΩΝ ΦΩΤΟΒΟΛΤΑΪΚΩΝ: ΑΝΑΠΤΥΞΗ ΗΛΙΑΚΩΝ ΚΥΨΕΛΩΝ ΒΑΣΙΣΜΕΝΩΝ ΣΕ ΕΤΕΡΟΔΟΜΕΣ ΘΕΙΟΦΑΙΝΕΙΟΥ-ΦΟΥΛΛΕΡΕΝΙΟΥ (α-6T/C_{60})

ORGANIC PHOTOVOLTAIC TECHNOLOGY: DEVELOPMENT OF ORGANIC SOLAR CELLS BASED ON THIOPHENE-FULLERENE (α-6T/C_{60}) HETEROJUNCTIONS

Κωνσταντίνος Δεσποτέλης

Supervisor: Επίκουρη Καθηγήτρια ΕΜΠ Δρ. Δ. Παπαδημητρίου
Co-Supervisors: Prof. Dr. M.-Ch. Lux-Steiner (HZB & FU-Berlin)
Dr. K. Fostiropoulos (HZB)
Prof. Dr. M. Kneissl (TU-Berlin)
Dr. P. Vogt (TU-Berlin)

Exams-Committee: Επίκουρη Καθηγήτρια Δ. Παπαδημητρίου
Αναπληρωτής Καθηγητής Κ. Παρασκευαΐδης
Καθηγητής Δημήτριος Μανωλάκος

Αθήνα, Ιούνιος 2013

Περίληψη

Η παρούσα διπλωματική εργασία έχει ως θέμα τους οργανικούς ημιαγωγούς και τις εφαρμογές τους ως χαμηλού κόστους εναλλακτική τεχνολογία για την κατασκευή οργανικών ηλιακών κυψελών. Οι οργανικοί ημιαγωγοί έχουν μεγάλο εύρος εφαρμογών, από το ταχέως και συνεχώς αναπτυσσόμενο πεδίο των φωτοβολταϊκών ως τις διόδους εκπομπής φωτός και τα τρανζίστορ πεδίου. Ηλιακές κυψέλες βασισμένες σε οργανικά μόρια διαθέτουν πολλά πλεονεκτήματα έναντι των μέχρι σήμερα χρησιμοποιούμενων κυψελών που έχουν ως βάση τους ανόργανους ημιαγωγούς. Συγκεκριμένα, είναι φθηνότερες στην κατασκευή τους καθώς τα οργανικά μόρια έχουν μικρό κόστος και απαιτείται πολύ λιγότερος χρόνος επεργασίας μέχρι το τελικό στάδιο κατασκευής τους. Επίσης, μπορούν να αναπτυχθούν επάνω σε εύκαμπτα υλικά και, ως εκ τούτου, να προσαρμοσθούν σε οποιαδήποτε επιφάνεια. Η οικονομική, μαζική παραγωγή τους σε μεγάλης έκτασης πάνελ αποτελεί και το κυριότερο κίνητρο, ώστε να γίνουν ανταγωνιστικές και εμπορεύσιμες.

Στα πλαίσια αυτής της διπλωματικής εργασίας, κατασκευάστηκαν, στα Εργαστήρια του Ερευνητικού Κέντρου HELMHOLTZ του Βερολίνου, οργανικές ηλιακές κυψέλες σε εργαστηριακή κλίμακα και μελετήθηκαν τα ηλεκτρικά και οπτικά χαρακτηριστικά τους, καθώς και η δομή και τα οπτικά χαρακτηριστικά των στρώσεων οργανικών-ημιαγωγών στις οποίες βασίζονται.

Ειδικότερα, τη βάση τους αποτέλεσε η ετεροεπαφή ολιγομερούς θειοφαινείου (a-6T) και φουλλερενίου (C_{60}). Η δομή των συγκεκριμένων μορίων απεικονίζεται στις εικόνες 1 και 2, αντίστοιχα. Η βασική μονάδα του θειοφαινείου, η οποία επαναλαμβάνεται έξι φορές για το σχηματισμό του εξαμερούς, αποτελείται από 4 άτομα άνθρακα και ένα άτομο θείου.

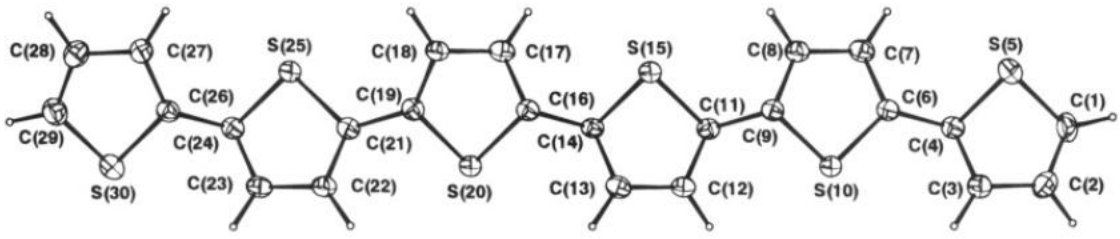

Εικόνα 1 Μοριακή δομή εξαμερούς θειοφαινείου (a-6T).

Το φουλλερένιο αποτελείται από πυκνή, σφαιρική συσκευασία άνθρακα υπό μορφή 20 εξαγωνικών και 12 πενταγωνικών δακτυλίων.

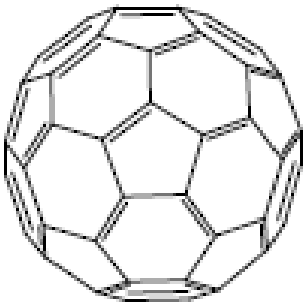

C_{60}

Εικόνα 2 Το μόριο του φουλλερενίου (C_{60})

Τα προαναφερθέντα οργανικά μόρια εξαχνώθηκαν υπό κενό και εναποτέθηκαν υπό μορφή λεπτών στρώσεων σε αγώγιμο υπόστρωμα. Καθ' αυτό τον τρόπο δημιουργήθηκαν αρχικά δείγματα των οποίων η επιφανειακή δομή έγινε εφικτό να αποκαλυφθεί με τη χρήση Μικροσκοπίας Ατομικής Δύναμης. Επίσης, μετρήθηκε η οπτική απορρόφηση του προσπίπτοντος φωτός με Φασματοσκοπία Ορατού-Υπερύθρου.

Στην εικόνα 3, απεικονίζεται η επιφάνεια ενός μεγαλύτερου σε πάχος στρώματος εξαμερούς θειοφαινείου ανεπτυγμένου σε υπόστρωμα διοξειδίου του πυριτίου. Όπως είναι εμφανές, η στρώση χαρακτηρίζεται από ραβδοειδή ανάπτυξη και σχετική ομοιογένεια. Αποτελεί πρόκληση ο τρόπος με τον οποίο μπορεί να καθορίζεται η επιφάνεια μιας στρώσης μεταβάλλοντας τις παραμέτρους κατά την εναπόθεση. Αυτές δύνανται να είναι: η θερμοκρασία του υποστρώματος, ο ρυθμός εξάχνωσης του οργανικού μορίου, το είδος του υποστρώματος, κ.α. Ο έλεγχος της επιφανειακής δομής είναι ιδαίτερης σημασίας καθώς επηρεάζει άμεσα τη μεταφορά φορέων δια μέσου της διεπιφάνειας των οργανικών στρώσεων ως τους συλλέκτες (ηλεκτρόδια) της ηλιακής κυψέλης, η οποία βασίζεται στις στρώσεις αυτές. Για παράδειγμα, λεπτότερες και μεγαλύτερου μήκους «ράβδοι» στην επιφάνεια του θειοφαινείου θα οδηγήσουν σε ευκολότερη μεταφορά των φορέων.

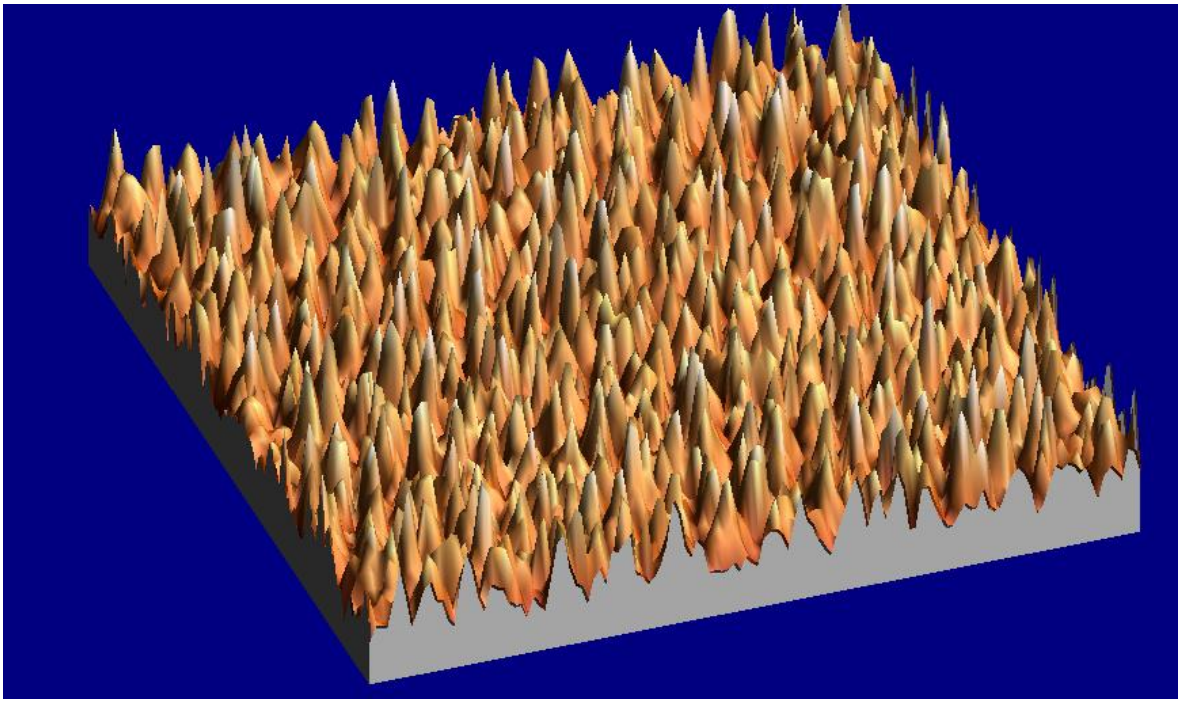

Εικόνα 3 Απεικόνιση της δομής της επιφάνειας λεπτής στρώσης εξαμερούς θειοφαινείου με Μικροσκοπία Ατομικής Δύναμης.

Οι οργανικές ηλιακές κυψέλες, οι οποίες κατασκευάστηκαν, περιλαμβάνουν σειρά στρώσεων, όπως φαίνεται στην εικόνα 4, επάνω σε οπτικώς διαπερατό, αγώγιμο υπόστρωμα ITO ($In_2O_3.SnO_2$). Αρχικά, εναποτέθηκε λεπτή στρώση (30nm) εξαμερούς θειοφαινείου, το οποία δρά ως δότης ηλεκτρονίων. Ως αποδέκτης χρησιμοποιήθηκε λεπτή στρώση (30 nm) φουλλερενίου. Ακολούθως, εξαχνώθηκε ιδιαίτερα λεπτή στρώση (10nm) πολυμερούς με την ονομασία BCP, η οποία συμβάλλει στον εγκλωβισμό των εξιτονίων (ζευγών ηλεκτρονίων-οπών τα οποία προκύπτουν κατά τις μεταβάσεις δότη-αποδέκτη). Η διαδικασία ολοκληρώθηκε με την εξάχνωση επαφών αλουμινίου (100 nm).

Εικόνα 4 Σχηματική αναπαράσταση οργανικής ηλιακής κυψέλης α-6T/C60.

Συγκεκριμένα, δυο εμπρόσθιες μεταλλικές επαφές τοποθετήθηκαν σε άμεση επαφή με το οργανικό στρώμα και μία οπίσθια επαφή σε επαφή με το υπόστρωμα. Καθ' αυτόν τον τρόπο γίνεται εφικτή η αποκόμιση δύο ξεχωριστών ηλεκτρικών μετρήσεων από την ίδια ηλιακή κυψέλη με χρήση κάθε φορά της κοινής οπίσθιας και μιας εκ των δύο εμπρόσθιων επαφών αλουμινίου. Στην εικόνα 5, παρουσιάζεται φωτογραφία μιας από τις οργανικές ηλιακές κυψέλες α-6T/C60, οι οποίες κατασκευάστηκαν.

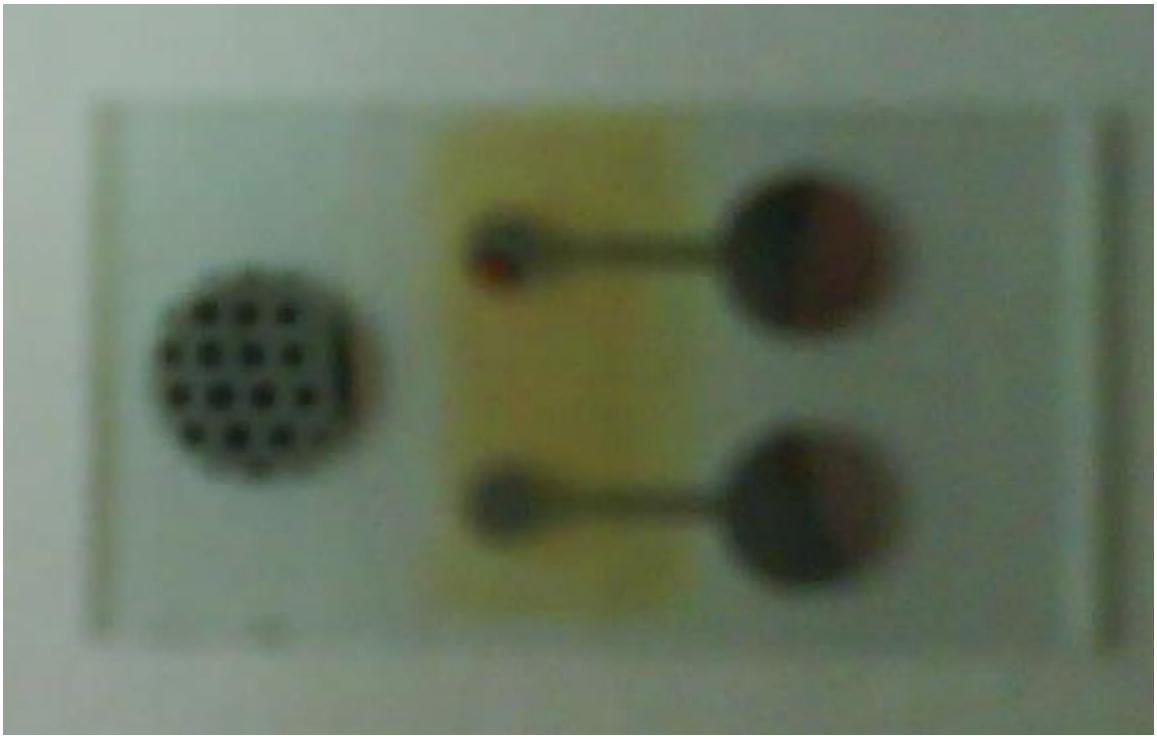

Εικόνα 5 Φωτογραφία ηλιακής κυψέλης α-6T/C60 που κατασκευάστηκε στα πλαίσια της παρούσας Διπλωματικής εργασίας.

Σε αυτό το σημείο αξίζει να αναφερθεί, ότι για την πραγματοποίηση μετρήσεων οπτικής απορρόφησης αναπτύχθηκαν δείγματα για κάθε ένα ξεχωριστό στάδιο κατασκευής της οργανικής ηλιακής κυψέλης. Με αυτό τον τρόπο, προσδιορίστηκε το ποσοστό στο οποίο κάθε υλικό ξεχωριστά συμβάλλει στην απορρόφηση του προσπίπτοντος φωτός. Στην εικόνα 6, παρουσιάζονται τα αποτελέσματα των μετρήσεων φασματοσκοπίας Ορατού-Υπερύθρου και συγκρίνονται με το τελικό στάδιο κατά το οποίο απορροφά η ηλιακή κυψέλη ολοκληρωμένη. Αξιοσημείωτο είναι, ότι η απορρόφηση της κυψέλης εμφανίζεται μειωμένη σε σχέση με το τελευταίο στάδιο, γεγονός που πιθανόν να οφείλεται σε απώλειες του προσπίπτοντος φωτός επάνω στις επαφές αλουμινίου. Επίσης, μειωμένη

διαπιστώθηκε ότι είναι η απορρόφηση στρώματος θειοφαινείου, το οποίο είχε εναποτεθεί σε υπόστρωμα θερμαινόμενο στους 90^{o}C.

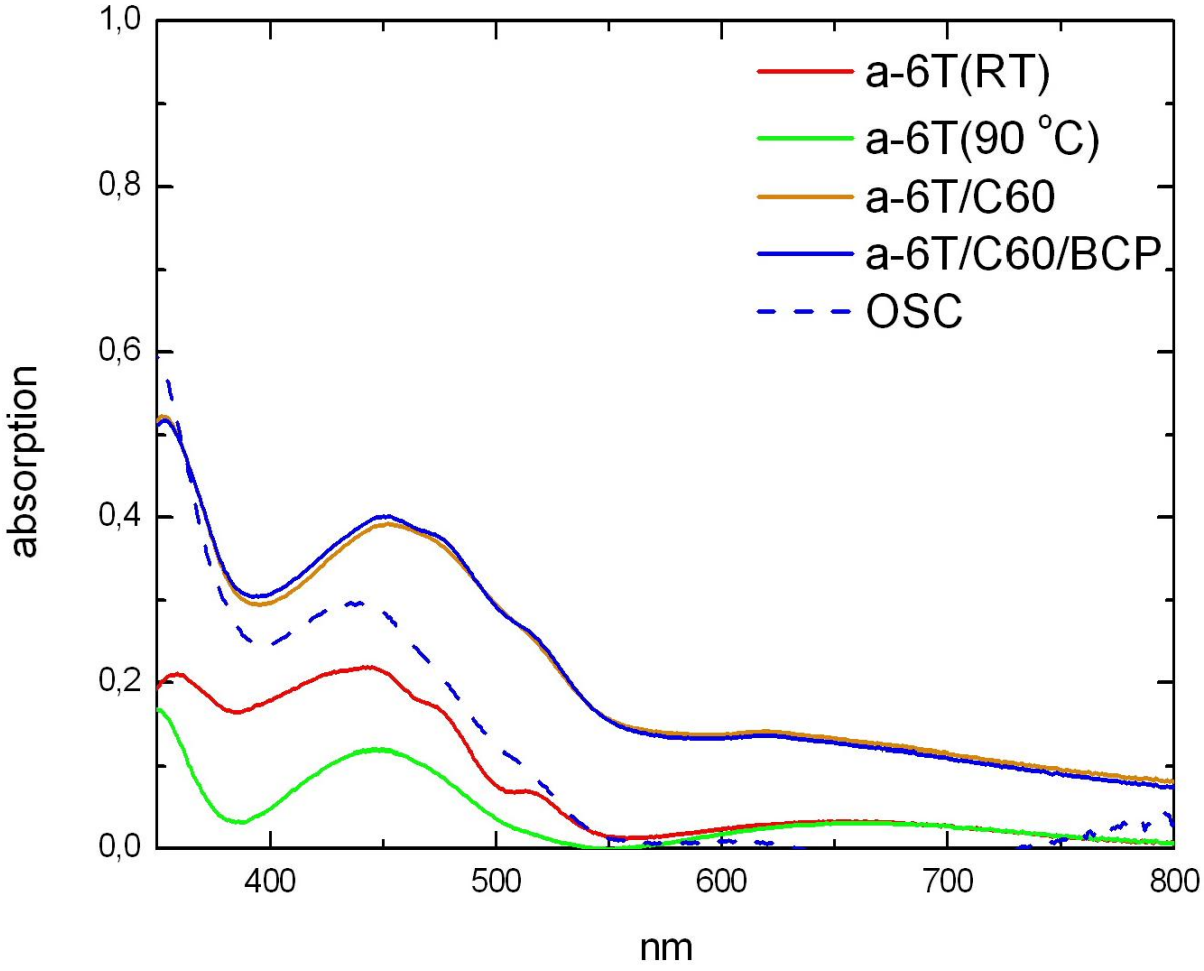

Εικόνα 6 Οπτική απορρόφηση ηλιακής κυψέλης α-6T/C60 και των επί μέρους τμημάτων της στα διάφορα στάδια ανάπτυξης της κυψέλης. Σύγκριση της απορρόφησης λεπτής στρώσης α-6T (RT) αναπτυγμένης σε μη-θερμαινόμενο υπόστρωμα με την απορρόφηση στρώσης α-6T (90 ^{o}C) που εναποτέθηκε σε υπόστρωμα θερμαινόμενο στους 90 ^{o}C.

Τελικό στάδιο χαρακτηρισμού των οργανικών ηλιακών κυψελών αποτέλεσαν οι ηλεκτρικές μετρήσεις της απόδοσής τους. Η μέγιστη απόδοση ανήλθε σε η=0.76%. Παρά τη σχετικά περιορισμένη απόδοση, σημαντική ήταν η επαναληψιμότητα των αποτελεσμάτων η οποία υποδεικνύει την σταθερότητα των οργανικών κυψελών, οι οποίες κατασκευάστηκαν. Στην εικόνα 7, παρουσιάζονται οι χαρακτηριστικές ρεύματος-τάσης μιας εκ των οργανικών ηλιακών κυψελών. Συγκεκριμένα, η μπλε καμπύλη αντιστοιχεί σε μέτρηση υπό πλήρη απουσία φωτός, όπου η κυψέλη οφείλει να λειτουργεί ως μια δίοδος, ενώ η πράσινη καμπύλη προκύπτει κατά την ακτινοβόληση της κυψέλης με φως. Αξίζει να σημειωθεί, επίσης, ότι οι χαρακτηριστικές καμπύλες υπέδειξαν την ύπαρξη δομικών

ατελειών, «παγίδων», οι οποίες δεσμεύουν εξιτόνια με άμεση επίδραση στην ηλεκτρική απόδοση της κυψέλης.

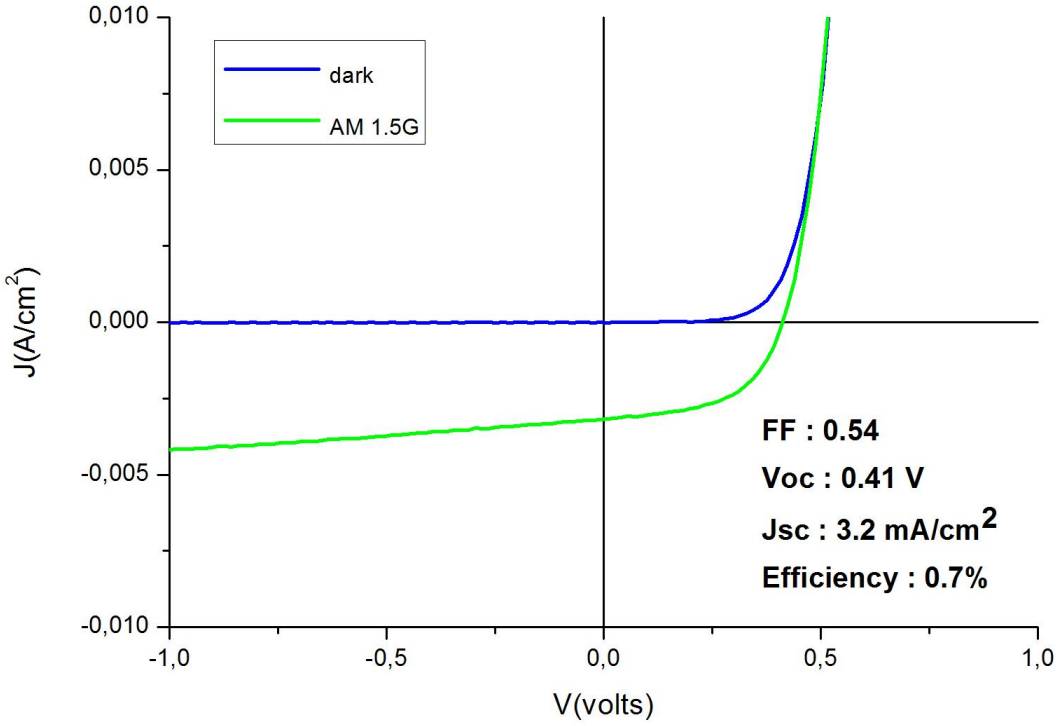

Εικόνα 7 Χαρακτηριστική καμπύλη ρεύματος-τάσης της ηλιακής κυψέλης.

Επιπροσθέτως, στην παρούσα διπλωματική εργασία, κατέστη δυνατή η εξοικείωση του συγγραφέα της, στο Πολυτεχνείο του Βερολίνου, με υψηλής ακριβείας πειραματικές μεθόδους Φυσικής Επιφανειών, ιδιαίτερα Μικροσκοπία Φαινομένου Σήραγγα, με την οποία μπορεί να ανιχνευθεί, σε πειραματικές διατάξεις υπερύψηλου κενού (10^{-12} mbar), και να απεικονιστεί ο προσανατολισμός οργανικών μορίων εναποτεθημένων σε διαφορετικές επιφανειακές αναδομήσεις ανόργανων ημιαγωγών. Η γνώση και ιδανικά ο έλεγχος του προσανατολισμού των μορίων ενός οργανικού ημιαγωγού είναι μεγάλης σημασίας: Καθορίζει και βελτιώνει πολλές από τις ιδιότητες του υλικού όπως και των κατασκευασμένων από αυτό ηλεκτρονικών διατάξεων.

Συμπληρωματικά, στο Εθνικό Μετσόβιο Πολυτεχνείο, διερευνήθηκε η δυνατότητα προσδιορισμού της ενέργειας μετάβασης HOMO-LUMO, η οποία είναι χαρακτηριστική για μοριακούς ημιαγωγούς, με υψηλής ευαισθησίας και ακριβείας Φασματοσκοπία Ηλεκτρικής Διαμόρφωσης, η οποία εφαρμόζεται με ιδιαίτερη επιτυχία σε ηλιακές κυψέλες λεπτών υμενίων ανόργανων ημιαγωγών παρέχοντας πληροφορίες για τα ενεργειακά χάσματα όλων των επί μέρους τμημάτων της κυψέλης.

Acknowledgements

My deepest gratitude goes to my Professor Dr. D. Papadimitriou first of all for her trust and for giving me the opportunity to work inside exceptional European research groups at Technische Universität Berlin (TUB) and Helmholtz-Zentrum Berlin für Materialien und Energie (HZB)**.** Her continuous guidance and support was essential during this diploma thesis and I should thank her for.

I am grateful to Professor Dr. M.-Ch. Lux-Steiner, director of the Institute for Heterogeneous Materials Systems at Helmholtz-Zentrum Berlin für Materialien und Energie (HZB), for giving me the chance to work in such a superior experimental environment. To special thanks I am obliged to Dr. K. Fostiropoulos, head of the Organic Solar Cells group. He introduced me to organic molecules and their application in Organic Solar Cells.

I greatly acknowledge Professor Dr. M. Kneissl and Professor Dr. A. Hoffmann for letting me be member of their workgroups at Technische Universität Berlin (TUB) during this diploma thesis. I am deeply grateful to Dr. P. Vogt for introducing me to an admirable experimental setup and laboratory. I feel obliged to thank Dr. T. Bruhn and PhD candidate L. Riele for their support and patience during my training at Technische Universität Berlin (TUB).

I would also like to thank all the members of both groups, that I worked with, for their support during the elaboration of this thesis independently of being minimal or played a considerable role.

I should also thank Dr. K. Anestou and PhD candidate G. Roupakas for their support at the NTUA LAB-facilities.

This diploma thesis would not have been possible without the continuous support of my family and I hope that one day I will become equal to their expectations.

This Diploma-thesis has been elaborated with the financial support of the **ERASMUS-LLP (Life Long Learning) Programme** between the National Technical University of Athens and the Technical University of Berlin.

Abstract

The present diploma thesis is focused on organic semiconductors and their possible applications in organic solar cells (OSCs). In fact, the alpha-sexithiophene (a-6T) molecule has been used as active component in a-6T/C60 organic solar cells (OSCs) processed by standard vacuum thermal evaporation techniques. Atomic Force Microscopy (AFM) imaging revealed rod-like growth of a-6T films. Different samples have been produced corresponding to the specific stages during the fabrication process of an organic solar cell and the optical absorbance was measured at each stage of the layer stack. UV-VIS spectroscopic measurements were also performed on a-6T films grown on heated substrates and were indicative of lower absorbance. Electrical measurements performed on the completed OSCs and well reproducible I-V characteristics are evidence of the structural stability of the developed OSCs with conversion efficiencies up to 0.76%. Higher conversion efficiencies are targeted by appropriate orientation of the a-6T molecular chains. An experimental method of using Scanning Tunneling Microscopy (STM) in order to verify molecular orientation of molecules deposited on different inorganic semiconductor surfaces is presented.

Table of Contents

Chapter 1 Introduction

About 60 years after the invention of the Si-based transistor, recent years have seen the first devices where organic materials are used as active components. Organic field-effect transistors (OFETs), organic light-emitting diodes (OLEDs), and organic solar cells (OSCs), have transitioned from scientific curiosities to potentially important technologies for consumer electronics and renewable energy converted from sunlight. For that cause, great collaborative efforts have been made by device physicists, material scientists, and chemists, during the past couple of decades. Subsequently, development of organic materials has taken place and a growing number of products that rely on such materials are in commercial production.

Organic materials possess a number of advantages over conventional inorganic Si and Ge semiconductor devices. Thin film formation, light weight, large area, mechanical flexibility, high brightness and contrast, wide viewing angle and lower power consumption are all desirable properties for electronic devices. As for the fabrication costs, the fact, that organic materials are compatible with roll-to-roll processing, could lead to very cheap large area devices, compared to the inorganic ones. The technological promise of these unique characteristics establishes organic electronics to the forefront of research efforts and enormous progress has been made in both, experimental and theoretical investigations. [1]-[2] Currently inorganic semiconductors still dominate the electronics industry. Nevertheless, the inherent attributes of the organic materials just described continue to drive their further development.

The central components for organic electronic devices are organic semiconductors. With the term organic semiconductor, we refer to all organic materials that have semiconductor properties. In contrast to inorganic materials (covalence bond), the solid state structure of organic semiconductors is based on weak interactions, principally van-der-Waals and dipole-dipole interactions, between neighboring molecules/polymer chains. [1]

Organic semiconductors are typically π-conjugated molecules comprised primarily of carbon, hydrogen, and other elements such as nitrogen, sulfur, silicon, boron, phosphorus, selenium, etc. Aromatic hydrocarbon and alkenes are typical building blocks for π-conjugated molecules, but heterocylics such as pyrrole, furane, thiophene, and pyridine are also important constituents. Depending on the molecular size, these organic semiconductors can be classified into small molecules, oligomers, and polymers.

Oligomers contain only a few repeat-units per molecule, whereas polymers contain many repeat-units per molecule. Typical polymer molecules contain hundreds or thousands of units per molecule. Polymers can be more easily processed and are generally considered to be better suited for mass production. The handling of oligomers, on the contrary, needs more effort but allows preparation of very well ordered films of high purity. [2]

Organic semiconducting polymers include intrinsically conductive polymers (ICPs) and light emitting polymers (LEPs) possessing electronic band gaps that allow for the emission of visible light. Organic polymers contain long chain block bone which normally gives rise to disordered structures. In contrast, small organic molecules possess extended π-conjugation that can form well-ordered crystalline structures and thus allow for the preparation of high purity, highly ordered thin films by sublimation techniques. Some oligomers may be processable by solution techniques. Although it is not yet clear which class of organic materials will dominate future organic electronics, the devices that have so far reached the market are mainly made from oligomers. In addition, the high-quality films of oligomers can serve as model systems that will ultimately make it possible to also understand the properties of polymers, in particular the mechanisms governing charge transport. The frequently used small organic semiconductors include pentacene, anthracene, rubrene, Alq3, and sexithiophene. The close packing of the molecules in the solid enhances the π-orbital overlap in the material, origin of its semiconducting and transport properties. [1]

In this thesis we focus on growth of thin films made by oligomers with complementary p- and n-type semiconducting behaviors, which are promising candidates for commercial organic electronic devices.

In order to understand the properties of these materials we need to review their molecular structure and understand the origin of the energy levels for electrons and holes as well as the mechanisms for electron and hole transport. The electrical and optical properties of the π-conjugated molecules are determined by the highest occupied molecular orbital (HOMO) and the lowest unoccupied molecular orbital (LUMO). The HOMO and LUMO energy levels represent the ionization potential and electron affinity, respectively, characterizing the materials abilities to donate and accept electrons. In other words, materials with high HOMO levels usually function as electron-donating and hole-transport media, while those with low LUMO levels function as electron-accepting and electron-transport media. Some materials that have both high HOMO levels and low LUMO levels exhibit bipolar transport characteristics, *i.e.*, they are capable of transporting both holes and

electrons. Increasing HOMO levels of hole-transport materials facilitates hole injection from anodes to lower the operation voltage for electronic devices. However, materials with high-lying HOMO levels are prone to oxidation by ambient air and hence are less stable. Lowering the LUMO levels of electron-transport materials allows for the fabrication of electronic devices using stable high-work-function cathode metals. Furthermore, the LUMO-HOMO energy gap, E_G, dictates the positions of the absorption and emission bands of conjugated molecules. [2]

Charge-carrier injection from a metal electrode into an organic thin film or from one organic thin film into another, and charge-carrier transport within the organic thin films, all are important parameters for device operation. Thus, organic electronic performance relies largely on the morphology, structure, ordering and thermal stability of the thin films and the properties of the interfacial layers. For instance, thin films showing highly ordered structure and high crystallinity normally have a better performance. For the morphological aspect, the thin films exhibiting large domains and less grain boundaries have higher charge mobility.

The organic/dielectric interface is a *must* of all organic devices. The metal-organic interfaces occur, e.g., at the metal contacts of OFETs where they influence the charge carrier injection in the organic film. In some devices, such as organic solar cells, or OLEDs, or ambiplolar transistors, organic-organic heterojunctions are basic elements, thus a comprehensive survey of the organic-organic interface is crucial for technological applications. [1]

The aim of this thesis is to investigate the growth of molecular layers on solid substrates, perform a basic research on morphology, structure and ordering of organic thin films and proceed with the fabrication of devices such as organic solar cells (OSCs). Of great significance is the study of properties that these devices exhibit and in which way, a better operation, with higher power conversion efficiencies, can be achieved.

In chapter 2, a more profound analysis of organic semiconductors and their general aspects is made. Furthermore, the theoretical background of thin film growth of the specific organic materials used is given and the very important role that orientation effects play on organic electronic devices and their performance is demonstrated.

Chapter 3 is entirely based on organic solar cells. At the beginning, a short flashback on these devices is made, followed by an in-depth analysis of their operation.

The properties and characteristics of organic solar cells based on alpha-sexithiophene, known from the literature, are reported.

Chapter 4 presents all the theoretical information of Atomic Force Microscopy and Scanning Tunneling Microscopy analytical methods and the basic principles of their operation. Methods that have been used in the present work for the optical characterization of samples and devices are also introduced.

Chapter 5 includes technical specifications of the laboratories where the experiments have been performed, in particular, the **National Technical University of Athens (NTUA), Helmholtz-Zentrum Berlin für Materialien und Energie (HZB)**, **Technische Universität Berlin** (**TUB), and Max Planck Institute in Golm (MPIG),** inclusive images of the experimental setups and systems.

In chapter 6, all the experimental results of organic solar cells based on alpha-sexithiophene (a-6T) and Fullerene (C60) are presented, analyzed and compared with the theoretical ones. Step by step, the whole procedure, from substrate preparation, through thin film growth, to a complete device, is demonstrated.

Chapter 7, reports the details and results of STM measurements on PbPc organic semiconductor molecules, carried out at **Technische Universität Berlin** (**TUB) by Experimental Nanophysics and Photonics Group, under the leadership of Prof. Dr. M. Kneissl and the supervision of Dr. P. Vogt. Published research of Dr. T. Bruhn and Phd candidate L.Riele have been used for reference**.

Finally, in chapter 8, the results of this thesis are summarized and conclusions are drawn.

Chapter 2 Materials

This chapter is divided into three sections and focuses on organic materials and their semiconducting properties. In section 1, the basic principles of organic semiconductors are given extensively and the organic semiconductors investigated in this thesis are presented. Thin film growth by Physical Vapor Deposition (PVD) and the influence of growth parameters on this process are discussed in section 2. Finally, in section 3, the very important role, that orientation effects play during layer growth, is discussed and associated with the specific characteristics that organic materials exhibit.

2.1 Basic Principles of Organic Semiconductors

Electrically conductive organic molecules, as electronic materials were understood in the 1970s, constitute now a new family of organic semiconductors that have the essential properties needed to produce technologically advanced electronic devices. Conductive oligomers/polymers, however, have electrical properties that are orders of magnitude significantly different from those of typical inorganic semiconductors and they may be processed at much lower (mild) temperatures. They can be used to make solar cells and light emitting devices as well as transistors and other electronic devices.

In order to understand the properties of these materials, we need to review their molecular structure and understand the origin of the energy levels for electrons and holes as well as the mechanisms for electron and hole transport. We will compare these to inorganic materials to highlight the distinctive properties that must be considered in order to make use of conjugated polymers/oligomers in semiconductor devices. [3]

Organic semiconductors consist of aromatic backbones with feature of 'π-conjugated bonds'. The carbon atom forms three sp^2 hybrids with 120° to each other in a plane and the remaining p-orbital is perpendicular to this plane. A σ-bond between two carbons forms by overlapping of two sp^2-orbitals and sideways overlap of p orbitals gives rise to formation of π-bond. **Figure (2.1)** depicts the orbitals and bonds for two sp^2 hybridized carbon atoms. If carbon atoms form larger molecules, typically with benzene rings as the basic units, the π-bonds become delocalized and form a π-system which often extends over the molecule. The band gap for organic semiconductors corresponds to the energy difference between the highest occupied molecular orbital (HOMO) and the lowest unoccupied molecular orbital (LUMO), which greatly impacts the optical and electrical properties. [1]

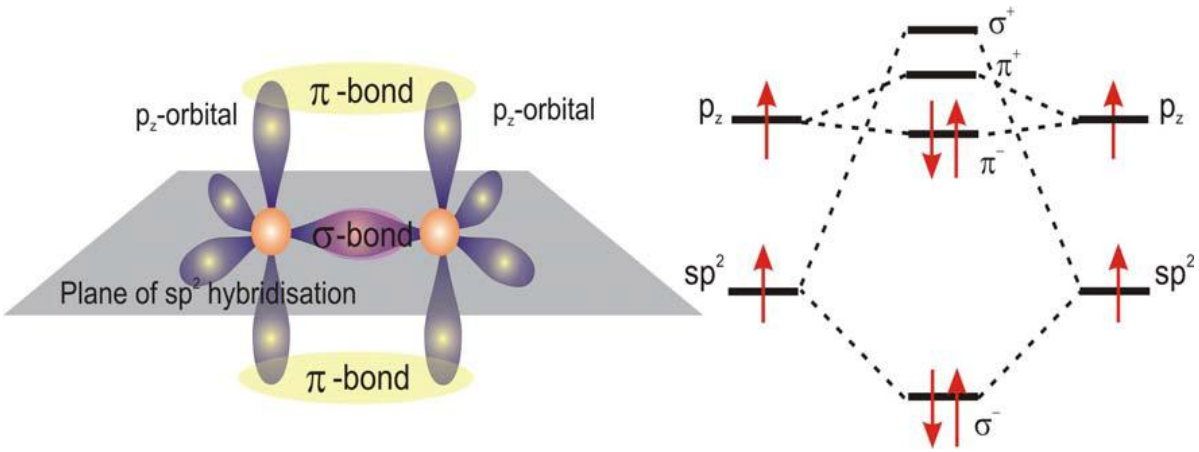

Figure 2.1 Scheme of the orbitals and bonds for two sp^2-hybridized carbon atoms [1]

Unlike inorganic semiconductors, the structure arrangement of organic semiconductors is based on weak van der Waals and dipole-dipole interactions. The electronic transport includes an intramolecular and an intermolecular transport. The transport within the molecule is very efficient due to the conjugated electrons but limits to small distances. The intermolecular charge hopping between adjacent molecules is slower and depends drastically on efficient intermolecular π-orbital overlap. [1]

Since a chain of closely spaced carbon atoms is created, there are as many π electrons as carbon atoms in the chain, and there is a spatial overlap of these individual π electrons. The π electron at each atom interacts with all the other π electrons in the chain to form a number of energy bands. These bands are collectively referred to as π *–sub-bands.* Electrical conductivity also arises as a result of these π electron sub-bands since the electrons they contain become delocalized. As with inorganic semiconductors the Pauli Exclusion Principle forces the π electrons to occupy a range of energy levels leading to the formation of bands. [3]

In addition we can regard such a conjugated molecule as a periodic potential in which the π electrons exist, which means that the Kronig–Penney[1] model would predict energy bands and energy gaps. The length scale of one period in the periodic potential corresponds to the length of one mer on the polymer chain. **Figure (2.2)** shows a band diagram of a molecular solid containing a few molecules. The small potential energy

[1] Principles of solar cells, LEDs, and diodes : the role of the PN junction / Adrian Kitai (§1.3)

barriers represent the separation between atoms or mers within a molecule (mers: repeat units /from the Greek word "meros"), and the large barriers represent the separation between molecules. Intramolecular bonds are normally covalent or conjugated bonds, and intermolecular bonds are much weaker van der Waals bonds. [3]

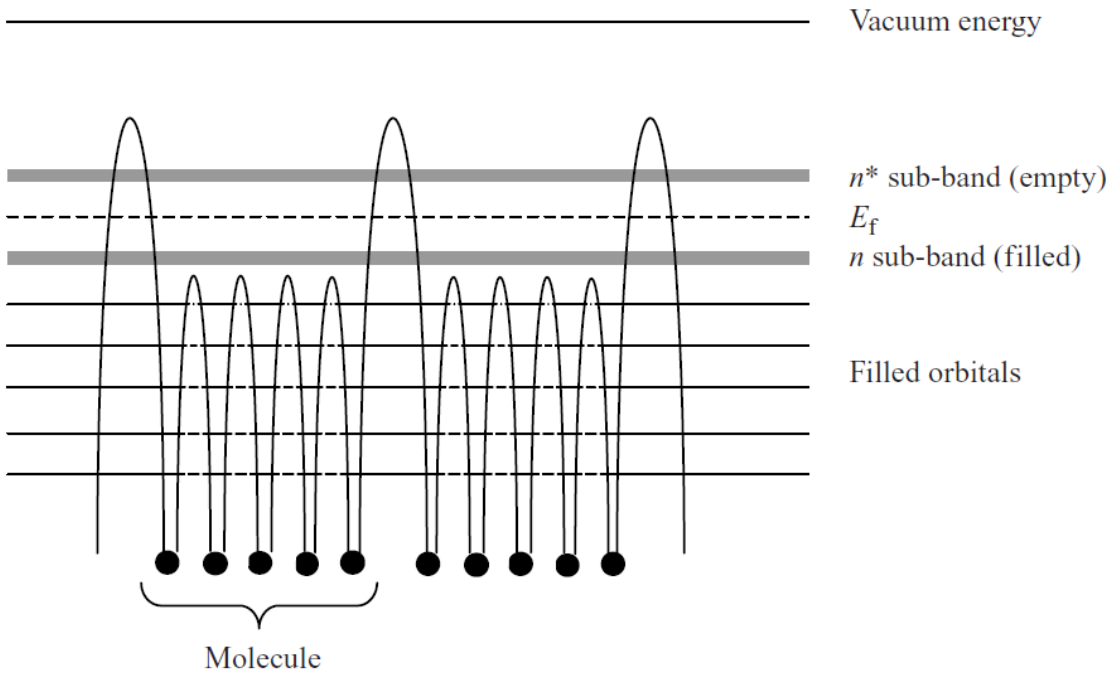

Figure 2.2 Energy levels and bands in a few closely spaced organic molecules. Note the small energy barriers caused by the intramolecular bonding and the larger energy barriers caused by the intermolecular bonding [3]

The energy levels in molecular materials can be related to the energy levels of inorganic semiconductors **(Figure 2.3)**. The energy needed to release an electron from the valence band of an inorganic semiconductor to the vacuum level is denoted as the ionization potential, while the electron affinity denotes the energy gained when an electron is transferred from the vacuum level to the conduction band edge. In molecular materials, electrons can be also liberated from the so-called highest occupied molecular orbital (HOMO) to the vacuum. The energy involved can roughly be estimated on the basis of the electrochemical oxidation potential (*vs.* NHE (Normal Hydrogen Electrode)) of the molecules using the relation: EHOMO ≈ ENHE – Vox, with ENHE = -4.5 V *vs.* vac. In a similar way, the electron affinity can be estimated from the reduction potential of the

molecules using: ELUMO≈ ENHE – Vred. The difference between both energy levels corresponds to the optical band gap of the molecules. Alternative methods to determine the energy levels in molecular layers include: Ultraviolet photoelectron spectroscopy (UPS) and Kelvin probe measurements. The concentration of mobile charge carriers within intrinsic molecular layers, in the dark, at room temperature, is usually small. The resulting conductivity of these layers is therefore relatively small. Intentional doping to form n- or p-type layers is not straightforward, since this causes often degradation of the organic material.

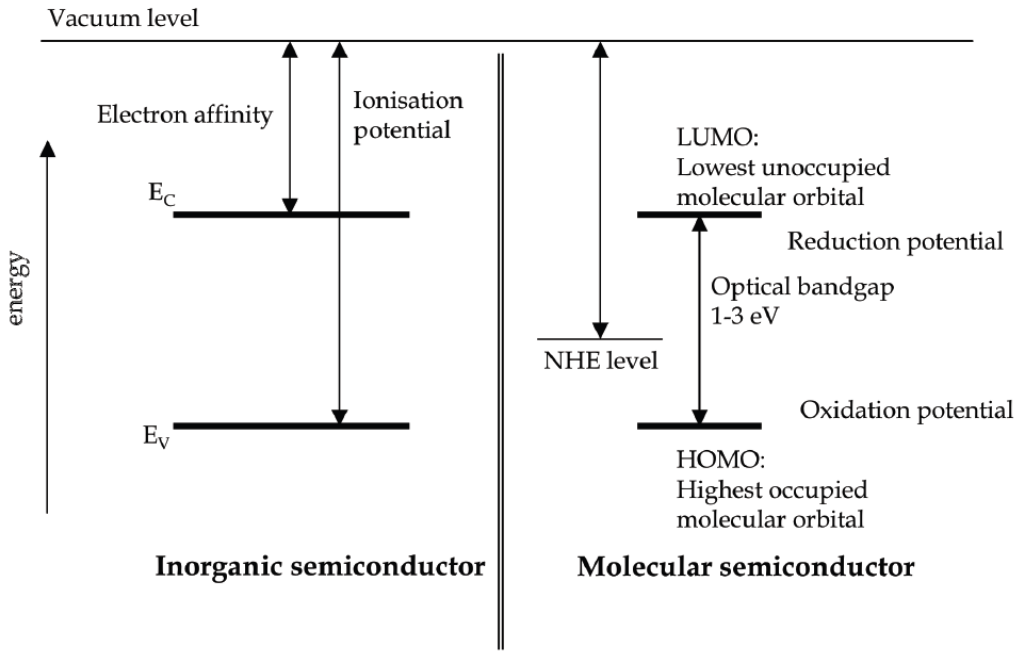

Figure 2.3 Overview of energy levels in inorganic semiconductors (left) and molecular semiconductors (right). [7]

2.1.1 Alpha-Sexithiophene (a-6T)

A highly oriented and continuous organic thin film is an ideal active layer for achieving high performance organic electronic devices. Among π-conjugated semiconductors, one of the most studied systems, both for the fundamental properties and the electronic applications is alpha-sexithiophene: a-6T. Since the first demonstration of oligothiophene based thin film transistors (TFTs), the hole mobility of a-6T has been improved from $10^{-3}cm^2V^{-1}s^{-1}$ up to $4\times10^{-2}cm^2V^{-1}s^{-1}$. Oligothiophene is well known as a good hole-transport material and by changing the number of thiophene rings and making chemical modifications or substitutions, its characteristics relevant to Photovoltaic (PV) applications (such as carrier mobility, energy level, packing, and ordered structure) can be controlled. Of course, to realize the full potential applications (and device performance) in these electronic or optical devices, it is necessary to have a good understanding of both, the electronic structure and physical properties of the system. The latter not only depends on the physical properties of the individual organic molecules but also on their relative orientation, which in turn affects their mutual interaction and thus fundamental film properties, e.g. charge transfer processes and various relaxation mechanisms. Thus, the creation of highly-ordered organic thin films becomes a very compelling topic to study [4].

Sexithiophene was originally investigated as a model system to better describe its parent, polythiophene. Well defined (and then highly-ordered) films of polythiophenes are very difficult to achieve, in part because within the polymerization process, the polythiophenes are likely to develop chemical and/or morphological defects, e.g. intermolecular entanglements and chain twists, causing break in the electronic conjugation. This fractioning leads to an assortment of conjugation lengths within the already non-crystalline (amorphous) polymer structure. Sexithiophene, 6T, is a planar, aromatic organic molecule consisting of six conjugated thiophene rings – each ring possesses four carbon atoms and one sulfur atom. After some initial studies on 6T, however, it became quickly clear that the molecule itself was interesting in that the material (films) could be well controlled and prospectively tailored (chemical structure changes such as side or end substitution) for technological applications. In fact, 6T has since been already used for fabricating devices. Specifically, good control over 6T thin film morphology can be practically achieved through convenient processing techniques, most commonly using vacuum sublimation under ultra-high vacuum (UHV) conditions. The interfacial (organic

film – substrate) properties are also crucial; using UHV is an advantageous technique here, since it assures that no contaminants could interrupt the relationship between the deposited molecules and the substrate. This provides for suitable control of the interface; for our purposes, this is of particular importance, since the substrate serves as a seed to induce a high structural order to be built up from sub-monolayer coverage to thin films [4].

Molecular architecture

As previously described, thiophene is a five-membered sulfur-containing aromatic compound, as sketched in **Figure (2.4)**. The addition of adjacent monomer units, each bonded via the a-carbons – i.e. the carbons neighboring the sulfur atoms – results in oligomers (small chain length polymers) of thiophene (Nt =N-thiophen). In our case, we have a chain of six thiophene monomers as it is shown in **Figure (2.5)**. The two carbon atoms opposite of the sulfur, known as β-carbons, are not affected by the chain length (since they do not directly interact, e.g. in a bridge position, with the neighboring rings). Thiophene rings can be conjugated as cisoid (all sulfur atoms on the same side, then all-cis) or transoid (all alternating, then all-trans); these gas-phase conformations differ by 180° dihedral (torsion) angle, and are very similar in energy. The situation may be different for adsorbed molecules, where this small energy barrier may be overcome by involving the carbon and sulfur atoms in surface bonding. It is exactly this surface-bonding mechanism, which varies depending on substrate that determines the orientation of the seeding monolayers, and is thus crucial for the formation of long-range ordered multilayers of oligothiophenes (and other large organic molecules) on crystalline surfaces [4].

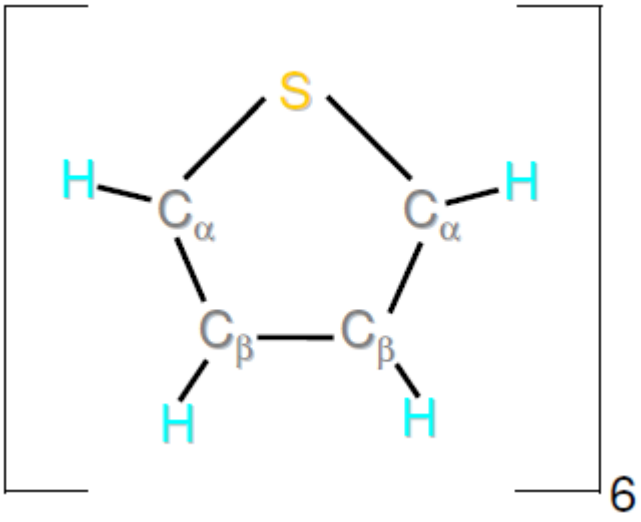

Figure 2.4: Sketch of a thiophene monomer with the atomic nomenclature for the carbon atoms. Sexithiophene consists of six conjugated rings. [4]

Metal substrates are then appreciable templates as they may provide considerable covalent interactions[2] with the organic molecule, and particularly the lateral ordering, at least in the monolayer regime, results from the interplay of both the substrate-adsorbate and the adsorbate-adsorbate interactions. These interactions may also result in different molecular isomers found in the film than those expected (energetically favored) in the gas phase. Finally, in most cases, this balance of interactions leads to commensurate superstructures for the first organic monolayers. Additionally, thiophenes were found to adsorb nondissociatively on many noble metal surfaces; in fact the bonded molecules still exhibit sufficient lateral mobility for two-dimensional ordering. Mobility only, however, doesn't necessarily warrant the formation of an ordered adsorbate monolayer. The substrate must additionally act as a template, e.g. through a particular corrugation structure that forces the assembly of the overlayer. Furthermore, any degree of order also sensitively depends on the experimental parameters (e.g. deposition rate) [4].

Specifically on the Au and Ag single-crystal surfaces, the molecules tend to adsorb in a coplanar geometry (ring planes parallel to the surface); this is attributed to a preferential bonding to the metal via the conjugated π-system[3]. Parallel geometry is often taken as an indication of bonding via the ring π-electrons[4], which may be identified in photoemission by peak shifts of the π-orbital features, or differential shifts of the σ-features towards higher binding energies. This so-called π-stabilization is a general feature of π-bonding of aromatic molecules to metallic surfaces. In fact, although thiophenes have been studied on various substrates (not only metallic), the question of chemical interactions, and likewise of other bonding mechanisms, is still highly debated [5][4].

[2]The bonding mechanism between thiophenes and metals (noble and transition) is generally accepted to strongly involve the substrate d-bands with a charge transfer from the molecular π-states to these d-bands, with an (almost) simultaneous back donation to the π^* states of the molecule. [4]
[3]The sulfur electrons play no important role in bonding. [4]
[4]A parallel geometry does not necessarily define _-stabilization. Both benzene and bithiophene on Al(111) adopt a flat-lying geometry, however, they are bonded via a purely electrostatic mechanism (no bonding of either the π-electrons or the S lone pair) [4]
[5]For example, 4T on Ag(111) has been reported to have a weak coupling but also a covalent (chemisorptive) bonding character. Also, on Ni(110) and Cu(110) strong π-bonding is observed, which can then be de-activated, in both cases, by a sulfur-modification (passivation) of the surface. However, a further S-modification (from a c(2x2)S and p(4x1)S surface) posses a still more reactive surface bonding. [4]

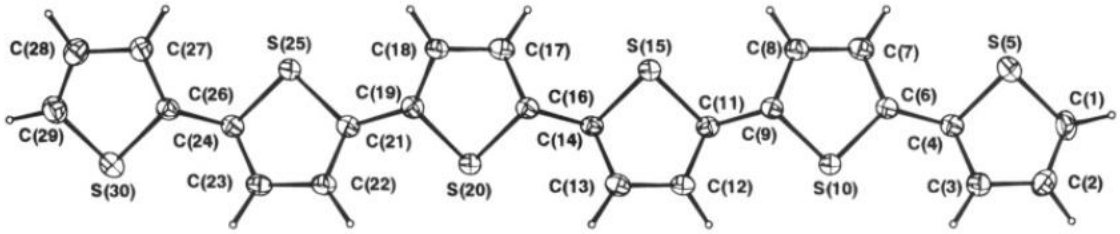

Figure 2.5: Molecular structure and numbering of sexithiophene (a-6T). [8]

In the solid state (and thin films), Nt molecules (n > 3) are almost planar (small tilt angle), with the point group symmetry C_{2h} for even numbered oligomers or C_{2v} for odd numbered oligomers. 6T molecules usually crystallize in a herringbone (HB) structure, common to planar molecules, in which the molecules face each other forming a quasi bi-dimensional H frame. The unit cell for crystalline 6T is presented in **Figure (2.6)**. Another helpful illustration of the 6T HB structure is presented in **Figure (2.7)** as shown through space-filling molecular orbitals. Orientational disorders of the molecules in the HB lattice were shown to strongly affect the crystals' optical and electronic properties (quenching optical signal and breaking the π-electron system). Hence, it is desirable to have control of the arrangement of molecules (not only at the interface), which would affect their mutual distance and thus their interactions, within a thin film (solid) sample. Again, this intimately depends on the experimental parameters.

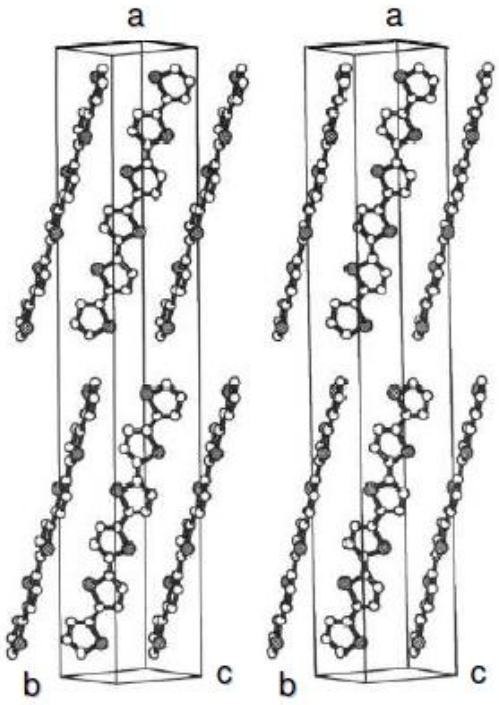

Figure 2.6: Stereographic view of the 6T unit cell, as inferred from x-ray diffraction measurements.

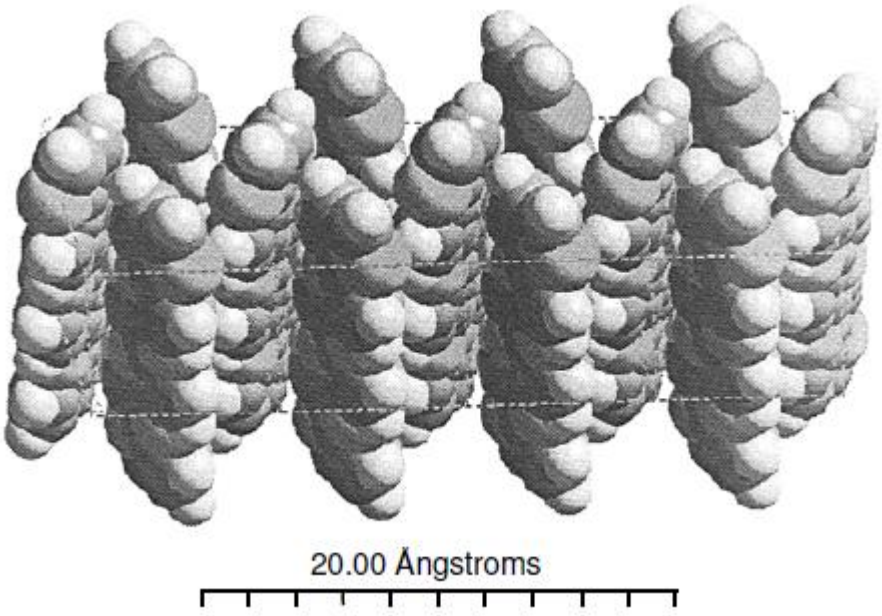

Figure 2.7: Space filling sketch of the herringbone pattern of the crystallized 6T lattice packing. [8]

Optical and electronic properties

Knowledge of the nature of the electronic structure of conjugated polymers is essential for an understanding of their electric and nonlinear optical properties. The electronic structure of 6T, particularly the π-orbitals (these are the orbitals important in surface chemical bonding), consists of a pair of localized and delocalized molecular orbitals per thiophene ring[6] (bonding and anti-bonding). Here, localized and delocalized refer to the probability of locating the electron wavefunction anchored on one atom (localized) or free to roam among several neighboring atoms (delocalized), specifically the carbon atoms. For the sp hybridized carbon atoms within 6T, there exists three σ-bonds and one remaining p-orbital, which overlaps with the adjoining unsaturated p-atomic orbital to form the continuous π-network (hence the term conjugated polymer). **Figure (2.8)** visually depicts the delocalized and localized orbitals, in 2-D and 3-D on the left and right sides respectively, according to the location of the carbon double and single bonds[7]. Notice that when the electronic structure consists of carbon double bonds connecting the C_α-C_β (top-left) the π-electron

[6] The valence orbitals develop gradually from molecular orbitals into broad bands in the large length limit.[4]
[7] The backbone of this structure (alternating double and single carbon bonds) resembles that of polyacetylene, a model organic molecule, however, with the sulfur atom breaking the symmetry. [4]

system likewise extends between the rings (top-right). This is known as aromatic character; clearly no contribution stems here from the sulfur atom. When the sulfur p_z orbital does participate in the molecular orbital (bottom-right), it remains separate from the delocalized carbon bonds, the C_β-C_β double bond (bottom-left) – i.e. localizing the electrons to one thiophene unit. This is denoted as quinoid character, always with significant electron density on the sulfur and (almost) no density on the C_α's [4].

Figure (2.9) shows the photo absorption coefficient of sexithiophene as was calculated from the optical density and film thickness [5]. Photo absorption coefficients of another two organic semiconductors; Zinc Phthalocyanine (ZnPc) and Fullerene (C_{60}), are depicted for comparison.

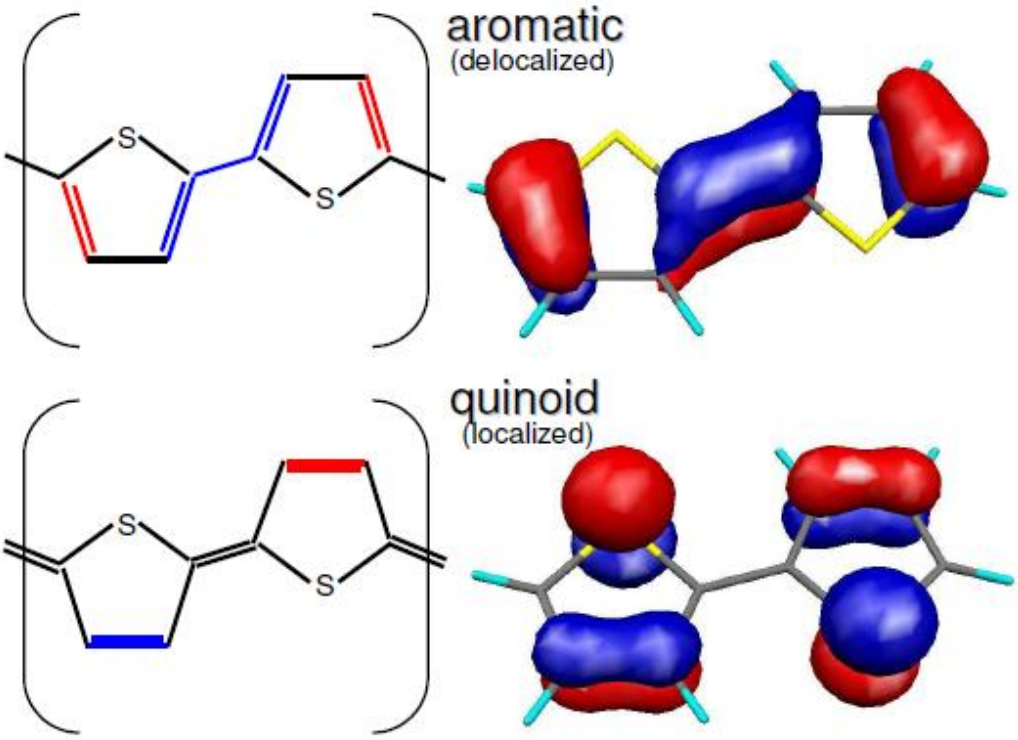

Figure 2.8: The two types of molecular orbital characters for thiophenes: aromatic vs quinoid. The particular pattern of the carbon double and single bonds dictate the localization of the orbitals' π-electrons. [4]

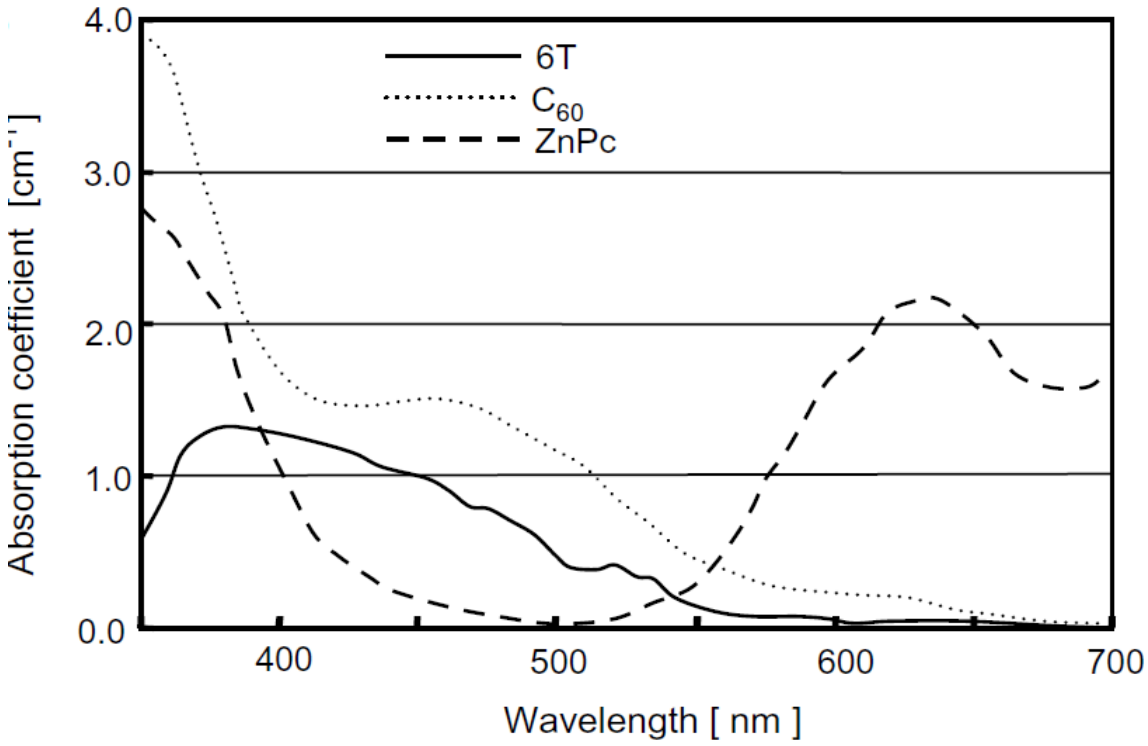

Figure 2.9: Absorption coefficient spectra of 6T, C_{60}, and ZnPc as calculated from UV–VIS optical density and film thickness. [5]

2.1.2 Fullerene C_{60}

Fullerene C_{60}, the most common representative of the fullerene family, is an organic material with semiconductor properties and was first produced on a preparative scale, in 1990, by resistive heating of graphite. Fullerene is an n-type semiconductor and so acts as an electron acceptor. Among the most spectacular findings, C_{60} was found to become a superconductor in M_3C_{60} species (M= alkali metal), an organic soft ferromagnet in TDAE $^{+}VC_{60}^{-}V$ (TDAE= tetrakisdiethylaminoethylene), a relatively stable hexaanion in cyclic voltammetry, and an interesting material with non-linear optical properties. [6] As was previously shown, **Figure (2.9)** presents the photo absorption coefficient of fullerene C_{60} calculated from the optical density and film thickness along with two other organic semiconductors.

Basic Principles of C_{60} Chemistry

The C_{60} surface contains 20 hexagons and 12 pentagons. All the rings are fused; all the double bonds are conjugated. Initially hypothesized as a 'super aromatic' molecule, C_{60} was rather found to possess a polyenic structure, with all the double bonds inside the six-membered rings. X-Ray crystal structure determinations on C_{60} and on some of its derivatives have proved the existence of two different types of bonds: 'short bonds' or 6,6 junctions, shared by two adjacent hexagons (ca. 1.38 Å long) and 'long bonds', or 5,6 junctions, fusing a pentagon and a hexagon (ca. 1.45 Å long). The geometric demand of the spherical cage is such that all the double bonds in C_{60} deviate from planarity. This pyramidalization of the sp^2-hybridized carbon atoms confers an excess of strain to C_{60} which is responsible for the enhanced reactivity of the fullerene. A release of strain is in fact associated with the change of hybridization from sp^2 to sp^3 that accompanies most chemical reactions. [6]. **Figure (2.10)** depicts the chemical structure of fullerene C_{60}.

Figure 2.10 Chemical structure of C_{60} [5]

2.2 Thin film growth

Knowledge of the rules governing thin film growth has become crucial, in order to achieve qualitative thin films, indispensable constituents for advanced microelectronic, optical and magnetic devices. Surface science methods find application for the purpose of understanding growth at the atomic level. As device miniaturization reaches submicrometer- and nanometer- length regimes, atomic-level control of the fabrication processes for novel materials becomes a necessity. Altering the morphology of a thin film during growth, by controlling deposition parameters, gives the advantage of selecting the desirable properties.

Growth of thin films from atoms deposited from the gas phase is intrinsically a non-equilibrium phenomenon governed by a competition between kinetics and thermodynamics. Precise control of the growth and thus of the properties of deposited films becomes possible only after an understanding of this competition is achieved. Here, the atomic nature of the most important kinetic mechanisms of film growth is explored. These mechanisms include adatom diffusion on terraces, along steps, and around island corners; nucleation and dynamics of the stable nucleus; atom attachment to and detachment from terraces and islands; and interlayer mass transport. [9]

Descriptions of atomistic mechanisms of growth have been largely based on the terrace-step-kink (TSK) model of a surface **Figure (2.11)**. In addition to defining steps, kinks, and terraces, **Figure (2.11)** shows several elemental entities in film growth: an adsorbed atom (adatom) and a vacancy on the upper terrace, an adsorbed dimer (addimer), and a larger island of four atoms in size. The scanning tunneling microscope (STM) has allowed direct visualization of the TSK model. The STM can be used to determine quantitatively kinetic and thermodynamic properties of morphological entities on a surface as small as a single atom, as large as a micrometer-sized terrace, or as high as many atomic layers. [9]

Information of this nature has allowed contact to be made with microscopic theories of film growth and has stimulated new theoretical developments. The synergism between experiment and theory has tremendously improved our understanding of the kinetic aspects of growth. For vapor phase epitaxy, the film growth kinetics are largely determined by only a few categories of atomistic rate processes, which form the basis also for all more complex growth situations. [9]

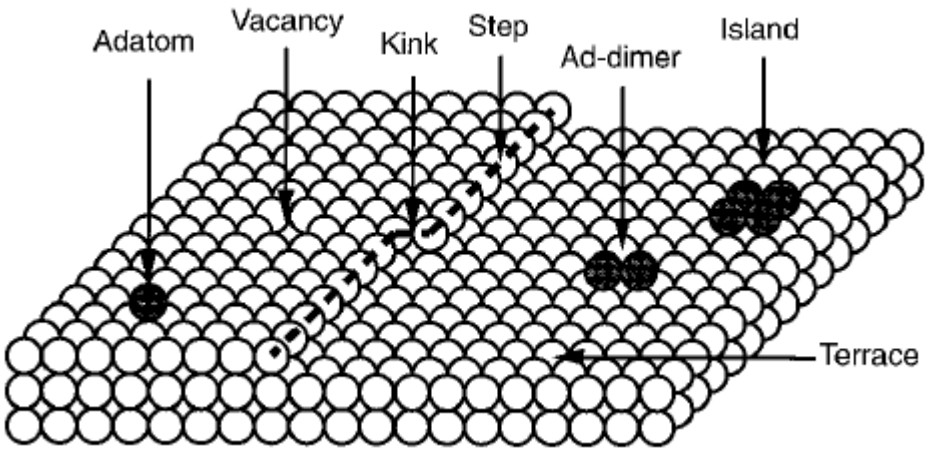

Figure 2.11 The TSK model of a surface defined for a simple cubic crystal. The white circles represent atoms of the substrate. The dashed line indicates the location of a step separating the upper and the lower terraces, with a kink along the step. The step-down direction is from left to right. The black circles are atoms adsorbed on the terraces. [9]

Numerous methods exist for the preparation of thin films, e.g. evaporation, sputtering, plasma decomposition, etc. For the experimental study of the basic phenomena of film growth, evaporation under thermal heating in UHV is the most suitable method, because, with this process, it is easy to have well defined experimental conditions. [10]

A typical set-up for the growth of films by vacuum evaporation is illustrated in Figure **2.12**. The vapour source is a Knudsen cell; this is a closed volume with the material to be evaporated inside and with a small hole in the lid. The cell, consisting of a refractory metal, can be heated by radiation or by electron bombardment. In the cell, an equilibrium vapour pressure of the material arises, which is a unique function of the temperature. The vapour beam flux is then only a function of the temperature of the cell and can be therefore controlled by that temperature. [10]

A shutter is mounted between the cell and the substrate to open or close the vapour beam and a substrate heater is mounted above the shutter. For the study of basic phenomena of thin film growth, single crystal substrates are most often used. These substrates are cleaved in vacuum immediately before the deposition of the film to avoid the adsorption of the residual gases on the substrate surface. Using a special substrate and deposit material, the main parameters of growth are the growth rate and the substrate temperature. [10]

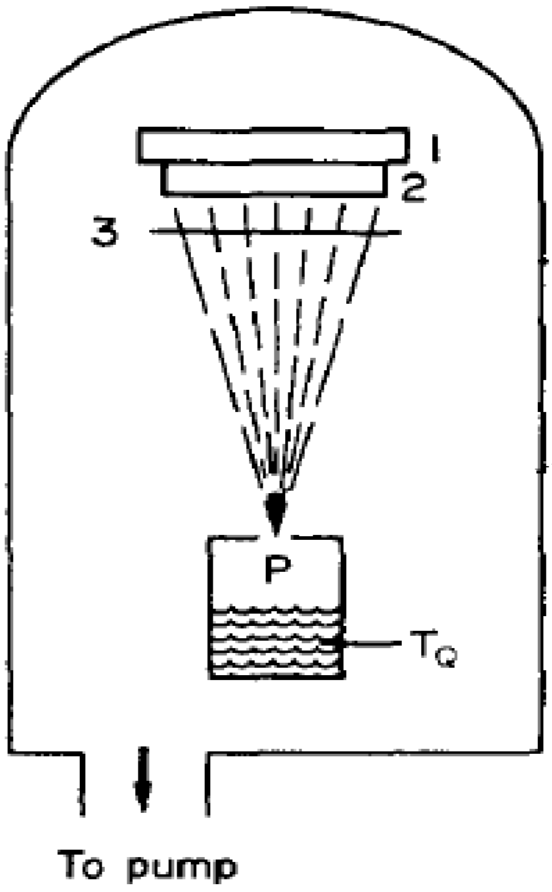

Figure 2.12 Vacuum Evaporation Chamber.

Adsorption and crystal growth modes

It is generally accepted that there are three possible modes of crystal growth on surfaces, which are illustrated schematically in **Figure (2.13)**. In layer by layer, or Frank van-der-Merwe mode, **Figure (2.13.a)**, atoms are more strongly bound to the substrate than to each other, the first atoms to condense form a complete monolayer on the surface, which becomes covered with a somewhat less tightly bound second layer. Providing the decrease in binding is monotonic toward the value for a bulk crystal of the deposit, the layer growth mode is obtained. In terms of ***energy difference*** $\Delta\gamma$, among ***substrate energy*** γ_s, film ***energy*** γ_f and ***interface energy*** γ_i, where $\Delta\gamma=\gamma_f + \gamma_i - \gamma_s$, [1], this mode occurs when $\Delta\gamma=0$. It is observed in the case of adsorbed gases, such as several rare gases on graphite and on several metals, in some metal-metal systems, and in semiconductor growth on semiconductors. [11]

The island, or Volmer-Weber mode, **Figure (2.13.c)**, displays the opposite characteristics, that is, small clusters are nucleated directly on the substrate surface and then grow into islands of the condensed phase. This happens when the atoms (or molecules) of the deposit are more strongly bound to each other than to the substrate **($\Delta\gamma>0$)**. This mode is displayed by many systems of metals growing on insulators, including many metals on alkali halides, graphite, and other layer compounds such as mica.[11]

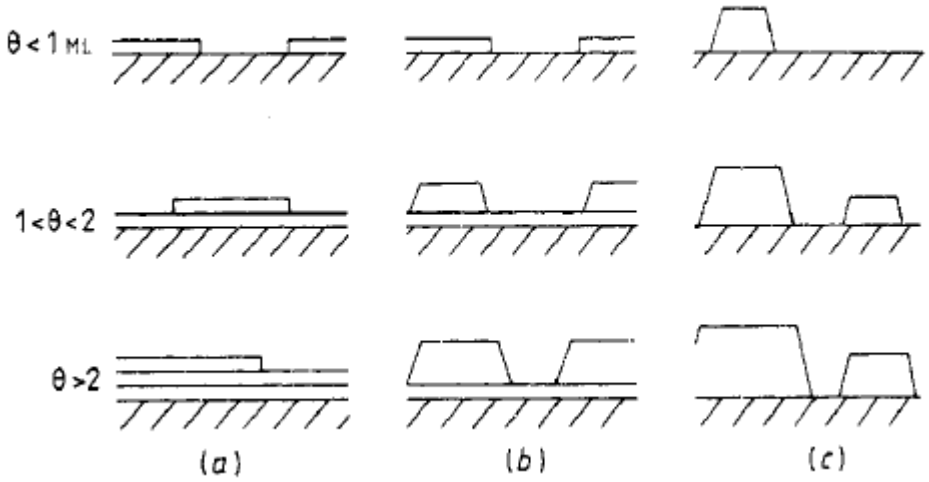

Figure 2.13 Schematic representation of the three crystal growth modes: *(a)* layer by layer or Frank van-der-Merwe mode, *(b)* layer plus island or Stranski-Krastanov mode, *(c)* island or Volmer-Weber mode. θ represents the coverage in monolayers (ML). [11][10]

The layer plus island, or Stranski-Krastanov, growth mode **(Figure 2.13.b)**, is an interesting intermediate case. After forming the first monolayer (ML) or a few ML, subsequent layer growth is unfavorable and islands are formed on top of this 'intermediate' layer. There are many possible reasons for this mode to occur; almost any factor (for example, *the lattice parameter of*, or *symmetry of*, or *molecular orientation in*), which disturbs the monotonic decrease in binding energy, characteristic of layer growth, may be the cause that the intermediate layer may not be able to be continued into the bulk crystal of the deposit. This results in a high free energy of the deposit intermediate-layer interface which favors subsequent island formation **($\Delta\gamma<0$)**. As it has been observed, this growth mode is much more common than was thought to be at first time. It is commonly observed

for lattice mismatched inorganic systems, such as metal-metal, metal-semiconductor, gas-metal and gas-layer compound. [11]

Nucleation and growth

In this section, a model is presented that describes the basic processes on a substrate surface, in the initial stage of growth. **Figure (2.14)** display these processes schematically. As was previously shown in **Figure (2.12)**, a source with active material is heated under ultra high vacuum, leading evaporated atoms to the substrate surface under a rate of arrival [10]-[11]:

$$R = \frac{C \cdot p}{(2\pi \cdot m \cdot k_b \cdot T_Q)^{\frac{1}{2}}} \left(cm^{-2} \cdot \sec^{-1}\right) \qquad (2.1)$$

where p is the vapour pressure, C is the geometrical factor, M is the molecular weight, k_b is Boltzmann's constant and T_Q is the source temperature. Single atoms adsorb on a substrate with a surface concentration $n_1(t)$ $\left(atoms \cdot cm^{-2}\right)$ on N_0 sites per unit area, so that the single-atom concentration is $\left(\frac{n_1(t)}{N_0}\right)$. These single atoms may then diffuse over the surface until they are lost by one of several processes, which may include re-evaporation or re-solution, nucleation of *2D* or *3D* clusters, capture by existing clusters, possibly dissolution into the substrate, and capture at special (defect) sites such as steps. On an ideally flat, 'inert' substrate, these last two processes would be excluded, though they may often be present in practice.

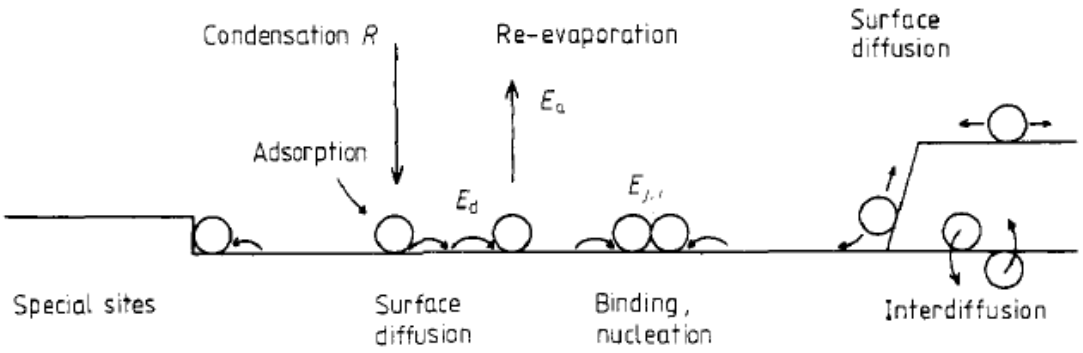

Figure 2.14 Schematic representation of processes and characteristic energies in nucleation and growth on surfaces. [11]

Each of these processes will be governed by characteristic times, which themselves will depend on the single-atom concentration and/or coverage. If such processes are thermally activated, then these times will in turn be controlled by activation energies and frequency factors. [11] For example, after an average stay time τ_A, ad-atoms are desorbed into the vacuum (re-evaporation) and this can be described by [10]:

$$\tau_A = \frac{1}{\nu_a} \exp\left(\frac{E_a}{k_b \cdot T_s} \right) \tag{2.2}$$

where ν_a is the vibration frequency, E_a is the activation energy for desorption and T_s is the temperature of the substrate. In addition to re-evaporation, there are diffusion energies ***(E$_d$)***, binding energies of small clusters of size ***j(E$_j$)***, up to the so-called 'critical' nucleus of size ***i(E$_i$)***. When large clusters can decay as well as grow, as is the case close to equilibrium adsorption conditions, then the corresponding free energies of evaporation (latent heats) in *2D* (onto the substrate) and *3D* (into the vapour) can also be important. In order to describe the behaviour of the early stages of nucleation and growth, the three types of independent material parameters ***E$_a$, E$_d$, E$_j$*** are essential, even on perfect substrate. [11]

Real surfaces, however, may be far from perfect, containing a distribution of ledges, kinks, dislocations and point defects, in addition to the perfect terraces. These imperfections can influence the binding of single atoms and small clusters to the substrate and via such binding changes can strongly influence adsorption, diffusion and nucleation behavior. This is especially so, as if there is a high nucleation barrier (i.e. a small concentration of critical nuclei) on a perfect terrace. Then the barrier will often be by-passed on a real surface by the agency of special sites, shown schematically in **Figure (2.14)** by a ledge. [11]

The ad-atoms diffuse on the substrate surface and the relation [10] is valid:

$$\left\langle x^2 \right\rangle = 2D \cdot t \tag{2.3}$$

where $\left\langle x^2 \right\rangle$ is the average value of the square of the diffusion distances in a special direction after the diffusion time *t.*

The diffusion constant is given by [10]:

$$D = D_0 \cdot \exp\left(\frac{-E_d}{k_B \cdot T_s} \right) \tag{2.4}$$

where $D_0 = a_0^{\,2} \cdot \nu_d$, ν_d is the vibration frequency of ad-atoms, E_d is the activation energy for diffusion, a_0 is the distance of a jump and T_s is the temperature of the substrate.

The surface concentration of ad-atoms can be calculated from the balance between adsorption and desorption. During the stay time τ_A, ad-atoms move by an average distance [10]:

$$\left\langle x^2 \right\rangle^{\frac{1}{2}} = \sqrt{2} \cdot a_0 \cdot \exp\left[\left(E_a - E_d \right) / 2k_B \cdot T_s \right] = \sqrt{D \cdot \tau_A} \qquad (2.5)$$

The desorption rate of adatoms can be described by [10]:

$$R_{des} = n_1 \cdot \nu_a \cdot \exp\left(\frac{-E_d}{k_B \cdot T_s} \right) = \frac{n_1}{\tau_A} \qquad (2.6)$$

The term 'sticking coefficient' which is used frequently in the description of thin film growth is the ratio (adsorbed rate) / (arrival rate).

β(t) is the differential sticking coefficient [10]:

$$\beta(t) = \frac{R - R_{des}(t)}{R} = 1 - \frac{n_1(t)}{R \cdot \tau_A} \qquad (2.7)$$

The integral sticking coefficient *α(t)*, is the average value *β(t)* in time [10]:

$$a(t) = \frac{1}{t} \int_0^t \beta(t') dt' \qquad (2.8)$$

Under special conditions (three dimensional growth at high substrate temperature $\boldsymbol{T_s}$) an adsorption-desorption equilibrium exists for a short period of time, if the arrival rate n_1 is constant [10]:

$$n_1 = const., \qquad \frac{dn_1}{dt} = R - \frac{n_1}{\tau_A} = 0 \rightarrow n_1 = R \cdot \tau_A \qquad (2.9)$$

and *β(t)* will be zero in this period of time.

The final sets of processes illustrated schematically in **Figure (2.14)** are re-arrangement processes. The clusters which initially form, at defect sites or on the perfect terrace, are not necessarily in their most stable form and can re-arrange in many different ways. Such processes can include mixing of species (alloying), shape changes caused by (surface) diffusion and/or coalescence, annealing of defects, etc. Diffusion processes thus occur at several stages of thin film formation: the motion of single atoms in forming small clusters, the mobility of these clusters themselves and the re-arrangement of larger clusters (islands) after coalescence. [11]

2.3 Orientation effects in organic semiconductors

Molecular structure of organic semiconductors and supramolecular arrangement in the solid state of grown films determine the physical properties of materials. Furthermore, these properties such as charge transport underlie **electronic device operation**, the optimization and improvement of which is the main target of research. Although it has been demonstrated that the molecular properties can be tuned by chemical tailoring, the solid–state supramolecular arrangement is generally more difficult to control, and appears to be one of the next challenges for materials science.

As was previously mentioned in paragraph 2.1.1 , alpha sexithiophene (a-6T) acts as a good hole-transport material with increased hole mobility over the past years, from $10^{-3}cm^2V^{-1}s^{-1}$ up to $4\times10^{-2}cm^2V^{-1}s^{-1}$. Upon several crystallographic and morphological studies, it is well known that transport properties of a-6T thin films correlate with morphology and molecular orientation, so this **enhancement of hole mobility is mainly related to growth of better oriented thin films.**

Observations made from multiple studies [12-16], indicate that molecular orientation exhibits different behavior depending on parameters such as film thickness (sub-monolayer, few monolayers, and thick films), substrate morphology, substrate temperature, evaporation rate, vacuum pressure, etc. According to Ref. [12], supramolecular organization in ultra-thin films (starting from sub-monolayer coverage) of a-6T on silicon dioxide (SiO_2), a common gate dielectric for TFTs, is characterized by the coexistence of two different phases: One with molecules lying with their long axis perpendicular to the substrate and one with orientation parallel to the substrate. Cross correlation of two different microscopy techniques was used as follows: One observing the photoluminescence (PL) intensity (Confocal Laser Scanning Microscopy (CLSM)) and another one, giving topographical information (Atomic Force Microscopy (AFM)). It was found, that AFM cannot reveal ultra-thin domains of a-6T molecules lying flat on the substrate and only the cross-correlation with PL microscopy and space resolved PL spectroscopy allows the supramolecular organization in sub-monolayer films to be understood.

Figure (2.15a–c) shows a series of AFM images of a-6T ultra-thin films grown on SiO_2 substrates kept at 120 °C. The films have a nominal thickness of 0.3, 0.8 and 2 nm (sub-monolayer coverage). The topography shown by the three films is island-like. The height profile of the islands is around 2.5 nm, comparable to the length of the a-6T molecule [8].

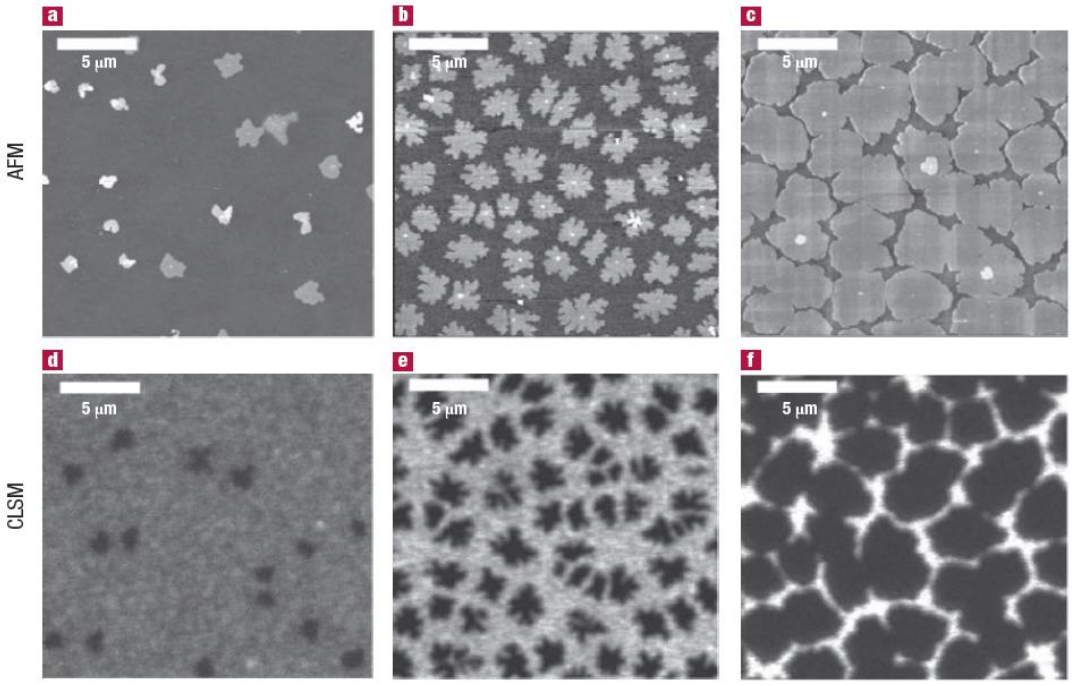

Figure 2.15 Topography and CLSM photoluminescence images of a-6T sub-monolayer films.
a–c: AFM and d–f: CLSM photoluminescence images of a-6T ultra-thin films on SiO_2.
The film growth conditions for a and d; b and e; and c and f, are: rate 0.02 Å s–1, substrate temperature 120 °C, nominal thickness 0.3, 0.8 and 2 nm, respectively. The step height of the islands in the AFM images is ~2.5 nm. [12]

An increase of the island lateral dimension is shown when going from thinner **Figure (2.15a)** to the thicker films **Figure (2.15c)**. AFM does not detect any presence of material in the inter-island region, even when operating in the most sensitive lateral force mode. **Figure (2.15d–f)** reports CLSM images of the same samples investigated by AFM. The three CLSM images show the same 'motif' of the topographical images, but with inverted contrast: dark islands (low PL emission) and bright inter-island regions (high PL emission). The topography of the islands in the PL images matches perfectly the islands shown by AFM. It is important to notice, that the SiO_2 substrates, before a-6T deposition, do not show any PL emission. Due to the fact that AFM does not detect any material to the inter-island regions where the high PL signal in the CLSM micrographs is limited, AFM cannot distinguish features of vertical dimension comparable with the r.m.s. roughness of the substrate (SiO_2 r.m.s. roughness 0.2–0.3 nm). Consequently, the upper limit for the thickness of the inter-island region can be estimated to be 0.2–0.3 nm.

With spatially resolved PL spectroscopy using a CLSM technique that allows fluorescence images and PL spectra to be correlated with an in-plane spatial resolution of ~200 nm, the authors in Ref. [12] managed to reveal that the a-6T molecules, in the inter-

island region, lie with their long axis parallel to the substrate. **Figure (2.16)** presents a schematic of the suggested film organization.

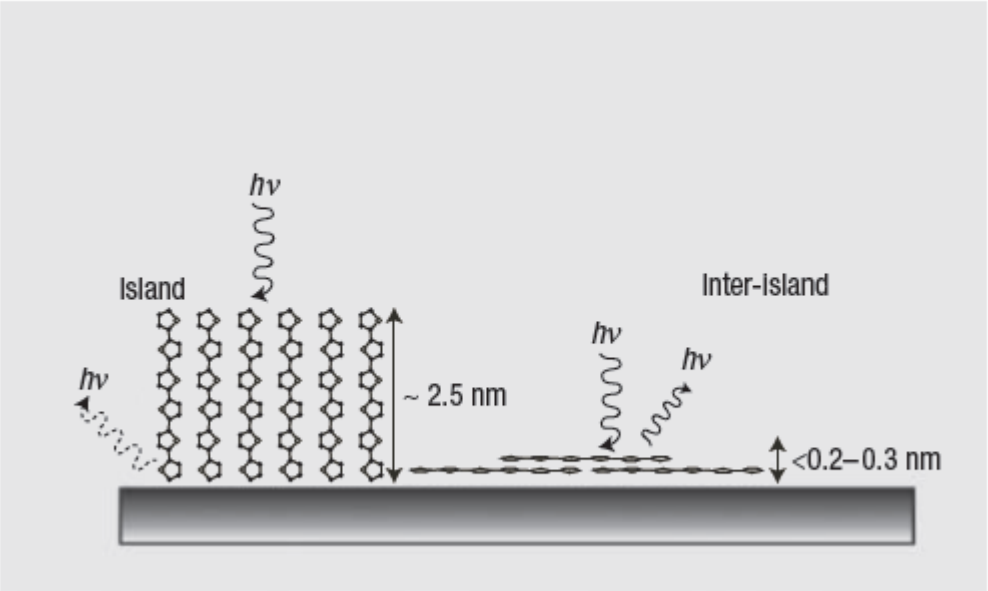

Figure 2.16 Schematic of the organization of the a-6T molecules in sub-monolayer films on SiO_2 substrates.

In films formed by at least a complete layer, the characteristic spectrum of the inter-island region is no longer detected, which means, that the orientation is completely different. The hypothesis, that flat lying molecules can still be located underneath the complete layer of perpendicular molecules, can be ruled out. In fact, due to the weak absorption of the complete layer of standing a-6T molecules, re-absorption of the lying molecules' PL by the complete layer can be excluded. Moreover, quenching phenomena induced by the molecular arrangement can also be excluded because of the low intermolecular electronic interaction between perpendicularly oriented rigid-rod molecules (that is, lying and standing a-6T molecules). ***This demonstrates that the molecules, which in the sub-monolayer films lie flat on the substrate, as the deposition continues, undergo rotation of their long molecular axis until, in thicker films, they stand almost perpendicular to the substrate.***

In addition to previous results, the authors in Ref. [5] evaluated the orientation of a-6T and C_{60} films deposited on a glass substrate, at room temperature, by X-ray diffraction (XRD). **Figures (2.17a)** and **(2.17b)** shows the XRD patterns of a-6T and C_{60} ***thick*** films, respectively.

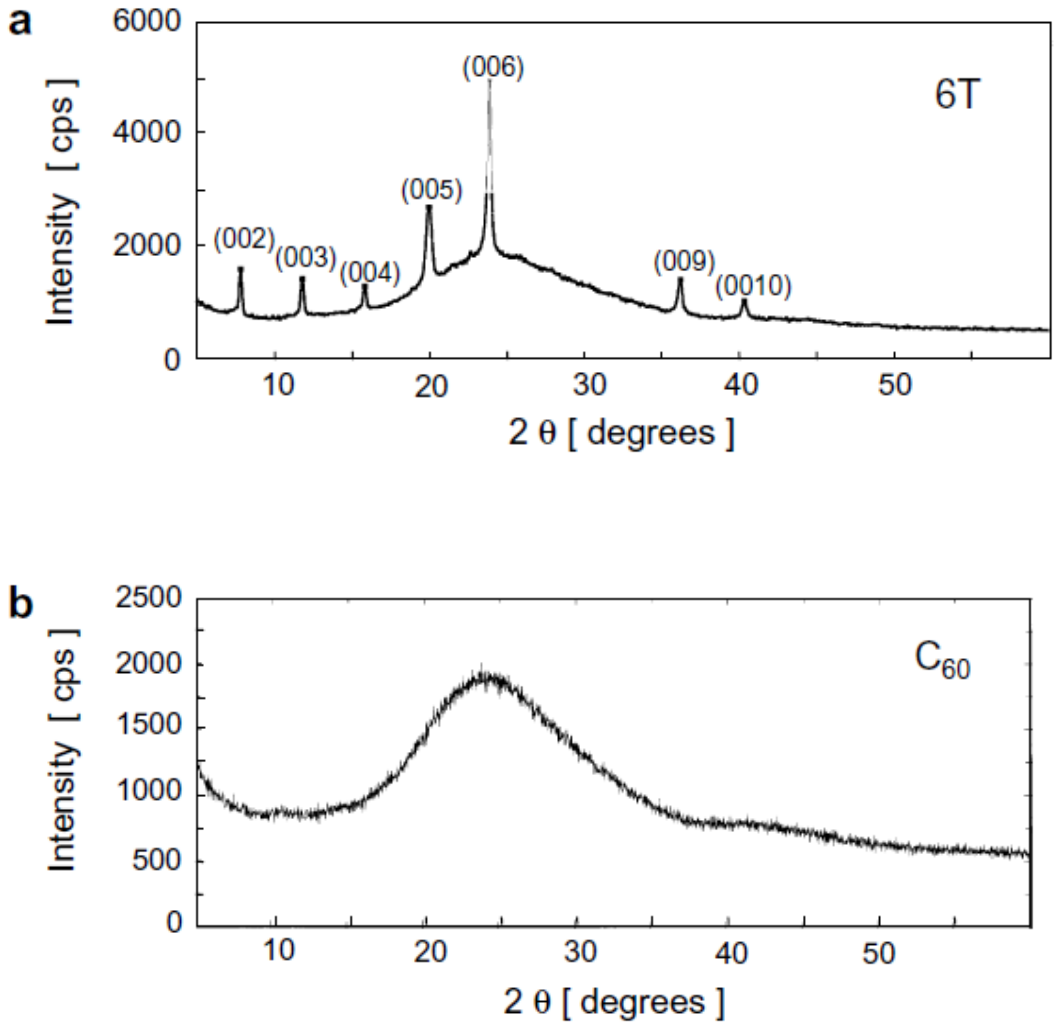

Figure 2.17 (a) X-ray diffraction pattern of sexithiophene film on a glass substrate, and (b) C_{60} film on a glass substrate. The broad peak at around 25 degrees corresponds to the glass substrate.

There are some sharp peaks in the a-6T film pattern indicating that the a-6T molecules are crystallized with a preferred vertical orientation. It is believed that hole mobility (intrinsic) in the horizontal direction is high, but lower in the vertical direction. This might prove unsuitable for photovoltaic devices. Conversely, no C_{60} peak was observed (as the broad peak at around 25 degrees corresponds to the glass substrate). This shows that the C_{60} film is almost amorphous.

Furthermore, research in Refs. [13]-[14] has revealed different XRD patterns of grown a-6T films depending on substrate selection and/or deposition rate. As a conclusion, it appears that controlling molecular orientation of films can lead to better charge transport and optical absorbance, and thus to organic electronic devices with improved operation.

Chapter 3 Devices

Organic Solar Cells (OSCs)

3.1 Introduction

Since the development of the first solar cell by Chapin, in 1954, composed of silicon based single p–n junction device with a solar power conversion efficiency of 6%, the main target of research has been the production of low cost, large area photovoltaics. Therefore, when the photovoltaic effect in laminated organic systems was first reported by Kearns and Calvin (1958), it was more than expected to think of organic semiconductors as ideal materials for solar cell applications. Among all the alternative technologies to silicon-based p-n junction solar cells, organic solar cells are the approach that could lead to the most significant cost reduction. In this direction, over the past two decades, rapid advances in science and engineering of organic semiconducting materials took place, leading to the demonstration and optimization of a range of organics-based solid-state devices, including organic light-emitting diodes (OLEDs), organic field-effect transistors (OFETs), and organic photovoltaic cells (OPV).

Nevertheless, the power yield of organic photovoltaic cells remained well below 1% for many years. A bilayer structure that delivered power efficiency slightly over 1% was reported by Tang (1986), but the fact that the device used very thin layers made inevitable to avoid short circuits when the area of the device was increased. This result represented the beginning of a new era of significant improvements in efficiency over the first report of a device with similar geometry by Kearns and Calvin in 1958. Production of high-purity conjugated polymers in the 1990s allowed the fabrication of organic photovoltaic cells with materials simply processed from solution.

The deposition of either organic small molecules from the vapor phase or polymers upon solution techniques gives the advantage of mild temperature processing. On the contrary, inorganic counterparts require high temperature procedures, a fact that minimizes the available range of substrates for deposition. Flexible plastic substrates, as shown in **Figure** 3.1, can lead to applications and consumer products with lower cost, highly flexible form factors, and light weight.

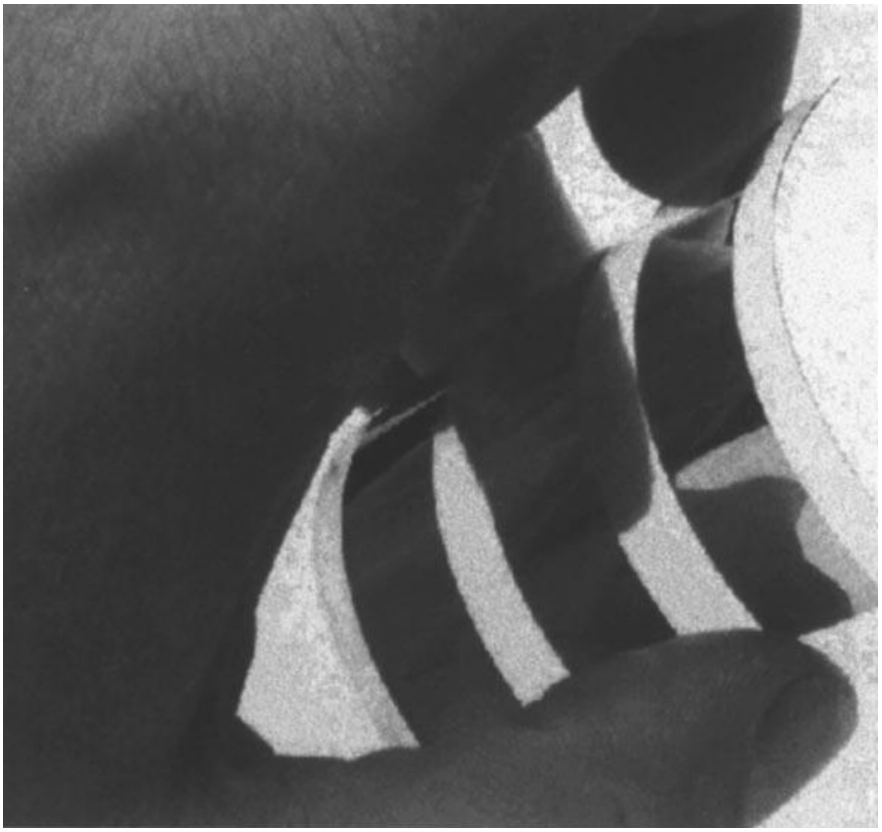

Figure 3.1 Flexible organic solar cell fabricated on a plastic sheet.

Furthermore, low-temperature processing cuts on energy use during manufacturing, further reducing **the energy payback time which is defined as the operating life of a power-generating device needed to produce the amount of energy invested during manufacturing, installation and maintenance.** These attributes, combined with the ability to tune the physical properties of organic molecules by fine tuning their chemical structure, constitute the main drivers boosting research and industrial interest in organic photovoltaics. [20]

The organics-based approaches and those that do not rely on conventional single p–n junctions are often referred to as third generation technologies. They include: (i) the dye-sensitized solar cells pioneered by Graetzel, which are electrochemical cells that require an electrolyte; (ii) multi-junction cells fabricated from group IV and III–V semiconductors; (iii) hybrid approaches in which inorganic quantum dots are doped into a semiconducting polymer matrix or by combining nanostructured inorganic semiconductors such as TiO_2 with organic materials; (iv) and all-organic solid-state approaches. [20]

While the physics of conventional p–n junctions is reasonably well understood and solar cell properties can be derived from materials parameters and the nature of the electrical contacts with electrodes, the understanding of the underlying science of organic solar cells is far less advanced and remains an intense subject of research. In the following, the basic principles of organic solar cells operation are described.

3.2 Device operation principles

Ghosh and Feng (1978) suggested a model, in order to describe device operation, which led the way toward efficient organic solar cells. According to that, the limiting step in organic solar cells, in contrast with inorganic semiconductors, is exciton diffusion rather than charge transport. In order to elaborate this difference, it is necessary to specify, that photon absorption, in inorganic semiconductors used in solar cells, contribute to generation of holes and electrons that are free to flow independently of each other and hence directly contribute to current flow. On the other hand, absorption of the impinging light, in a molecular organic semiconductor, promotes the formation of a bound hole-electron pair known also as exciton. ***This exciton is localized to a single molecule, which is generally on the nanometer length scale, and hole-electron extraction upon dissociation of the exciton is essential for current production***. It is easily contracted the conclusion, that the most significant objective, in the development of organic solar cells, is to overcome the localization and pairing in the form of excitons of optically generated holes and electrons.[3]

Excitons can be dissociated at interfaces of materials with different electron affinities called heterojunctions and by electric fields, or the dissociation can be trap- or impurity-assisted [18]. Quantum yield during charge separation of an exciton is very low unless the electric field is very high. Unfortunately, the latter is limited in a photovoltaic cell because the voltage drop through the device cannot exceed the work function difference between both electrodes, that is, 1.5V at most. One idea consists of using two materials between which photoinduced charge transfer is ultrafast, thus avoiding any other exciton relaxation mechanism. The initial separation of charges may then take place with quantum efficiency close to unity [17]

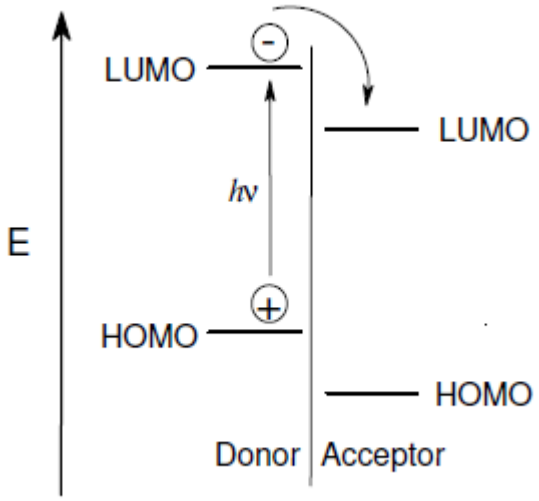

Figure 3.2 Schematic energy diagram of a donor-acceptor heterojunction. [19]

Figure 3.2 shows the initial step of an exciton formation subsequent to photon absorption, inside the material with the highest LUMO level called donor, and consequently followed by charge separation at the interface with the acceptor material, which is characterized by the highest electron affinity. The electron is transferred to the acceptor and, even it is not shown here, excitation of the acceptor can lead to the same charge separated state, when electron transfer from the HOMO level of the donor to the HOMO level of the excited acceptor takes place. In order to achieve an optimal device operation with high power conversion efficiency, the following five processes take place inside an organic solar cell and they will be extensively presented once first the different device structures, architectures, and performance characteristics are reported:

These five processes are:

I. Light absorption followed by exciton formation
II. Diffusion of excitons at the interface
III. Exciton disassociation into free charge carriers
IV. Charge transfer within the cell
V. Charge collection at the electrodes

3.3 Device architecture & operation characteristics

The simplest form of an organic solar cell, as shown in **Figure 3.3**, is comprised only of a single active layer of organic material deposited on a Transparent Conductive Oxide (TCO) coated glass substrate. In particular, Indium Tin Oxide (ITO) coated glass is commonly used. The device is completed upon deposition of two metal contacts (Al, Mg, Ag, Au etc.), one metal contact deposited on ITO acting as anode and the other one on top of the stack as cathode.

As previously mentioned, photons create molecular excitons in the organic semiconductor layer. In order for these charges to be collected, an electric field high enough must be applied. This field is generated between the anode and the cathode of the device due to their different workfunctions. The diffusion length of carriers is generally in the order of 10 nm, while the thickness of the semiconductor layer is much more than 10 nm to achieve a reasonable degree of photon absorption. The majority of the generated excitons are never dissociated and only a small fraction of generated carriers are collected by the electrodes. In fact, the electric field is only high right at the abrupt electrode-semiconductor interfaces, and this is where exciton dissociation can most readily occur. Efficient carrier collection, however, requires the participation of both carrier types, which is not favored by this approach. The energy level diagram for this structure is shown in **Figure 3.4**. [3]

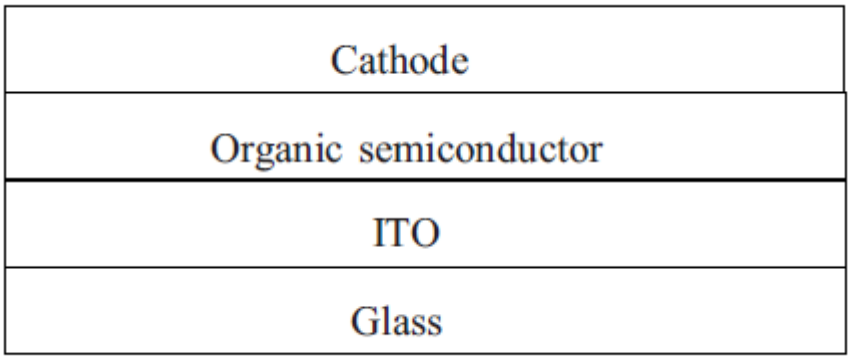

Figure 3.3 ***Single-layer organic solar cell consisting of a single organic semiconductor layer, a low workfunction cathode and a transparent anode. Device efficiency is well below 1% [3]***

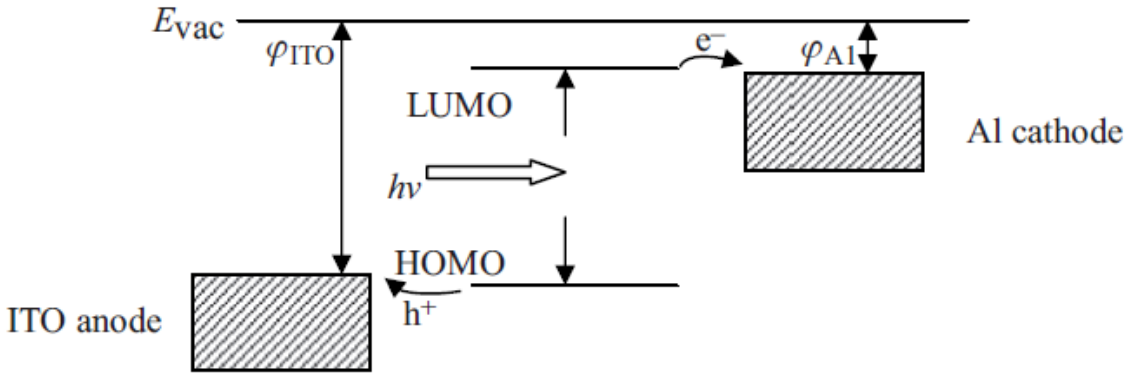

Figure 3.4 ***Energy level diagram for single-layer organic solar cell. The absorption of light creates excitons through the promotion of molecular electrons from the HOMO level to the LUMO level. Electrode workfunctions are set to match the HOMO and LUMO levels to facilitate the collection of the electrons and holes as shown***

As mentioned previously, an idea to achieve high electric field within the solar cell, in order to contribute to charge separation and at the same time efficient charge collection, is to introduce a second active layer, creating a heterojunction. The heterojunction consists of a hole transport donor layer (HTL) and an electron transport acceptor layer (ETL) on top of it. In **Figure 3.5** the aforementioned device architecture is presented.

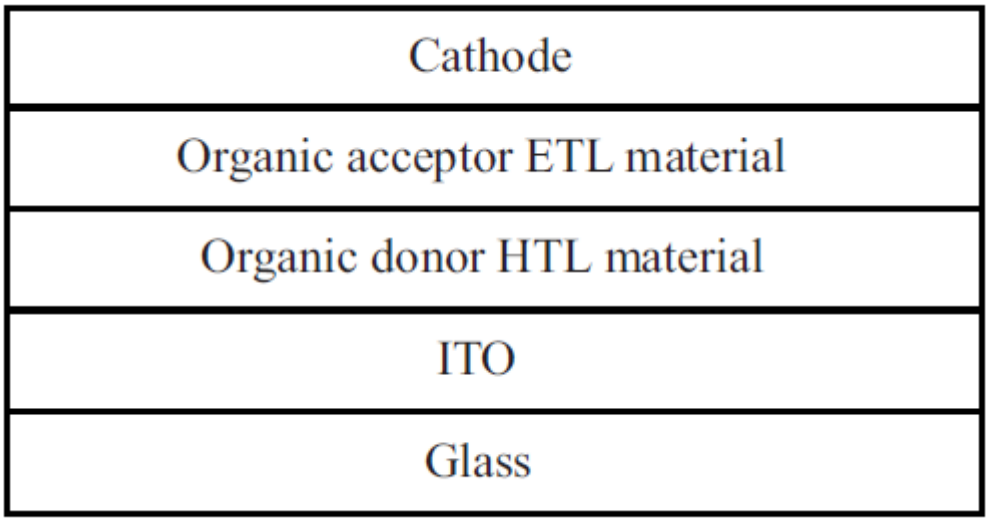

Figure 3.5 ***Organic planar heterojunction solar cell structure showing donor and acceptor organic layers***

In principle, both the donor and acceptor layers can absorb photons and become populated with excitons. These excitons can then diffuse towards the heterojunction interface and dissociate there, where generation of strong electric field becomes an advantage and enhances the procedure greatly. However, the way, that the solar cell is designed, favors the absorption of photons by the donor layer, resulting to high exciton population. Since the mobility of holes is relatively higher than that of electrons, the donor HTL allows the holes to diffuse towards the heterojunction interface. The electrons will remain bound to the holes since exciton dissociation will not readily take place until the excitons reach the interface. This interface now enables the collection of both electrons and holes, which drift across their respective layers: Holes reach the ITO electrode through the hole-conducting layer, and electrons reach the cathode through the electron-conducting layer.[3]

The sharp and narrow high field region at the heterojunction interface in organic solar cells may be contrasted with the inorganic p-n junction. The width of the depletion zone in inorganic junctions is determined by the spatial extent over which carriers recombine to establish an equilibrium condition. At the organic interface in organic junctions, charge carriers in the HOMO and LUMO levels transfer from molecule to molecule by hopping and only minimal charge transfer occurs, leaving the equivalent of a depletion zone of very small thickness. The potential difference between the HOMO and LUMO levels falls across a very small spatial range of dimension in the nanometer scale giving rise to a high electric field at the junction.[3]

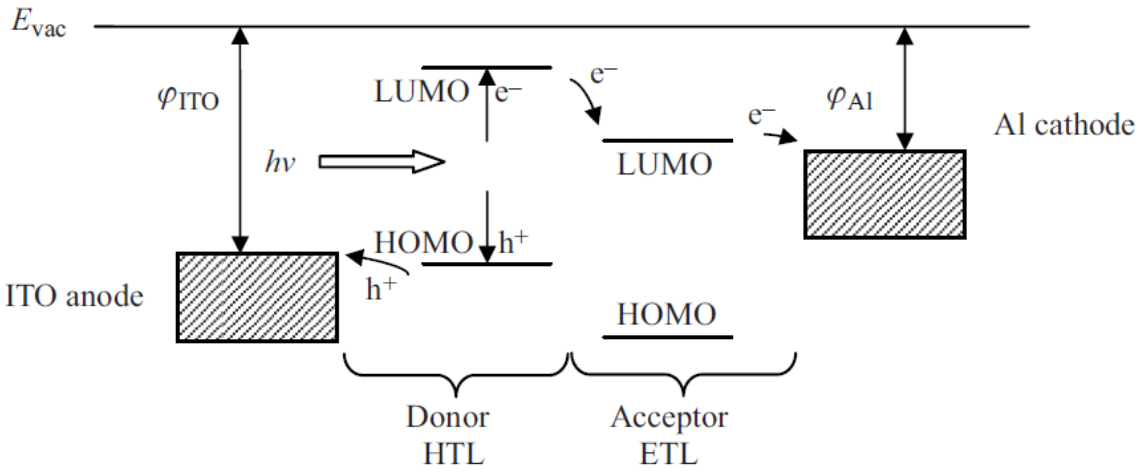

Figure 3.6 ***Heterojunction solar cell showing donor and acceptor LUMO and HOMO levels. Excitons are generated throughout the donor layer and these excitons are dissociated when they diffuse to the donor-acceptor interface. Finally, the separated holes and electrons can drift to their respective electrodes***

As shown in **Figure 3.6**, electrons that are dissociated from the excitons in the donor layer at the junction are transferred or 'donated' across the interface from donor molecules and accepted by acceptor molecules in the acceptor layer. The holes from the dissociated excitons remain in the donor layer and drift to the anode. This procedure described briefly, explains the terms 'donor' and 'acceptor'.

The terminology is a molecular analogue of the terms 'donor' and 'acceptor' applied to dopants used in inorganic semiconductors; however, the organic molecules donate and accept electrons to/from neighboring molecules rather than to/from energy bands. Since the acceptor layer becomes populated with electrons this layer needs to be an electron conductor and charge is carried in its LUMO level. Conversely the donor layer, being populated with holes, needs to be a hole conductor and these holes are carried in its HOMO level.[3]

Another effective approach in organic solar cell architecture is the formation of a bulk heterojunction of active organic layers. This technique increases solar cell performance and can be achieved either by in sequence arrangement of several layers of different organic semiconductors or by co-evaporation of the materials that creates a mixed organic layer. The main advantage of this method is the optical absorbance in different parts of the spectrum by each layer, since the absorption bandwidth of organic semiconductors is limited. This is due to the much narrower π and π^* bands than the conduction and valence bands in inorganic semiconductors.

In every case of device structure, thickness optimization of the active layers plays a very important role in device performance. This relies on the fact that excitons are characterized by a diffusion length inside the material, until they recombine. This length in organic materials is approximately 10nm as mentioned previously and is given by:

$$L_{EXC} = \sqrt{D_{EXC} \cdot \tau_{EXC}} \qquad (3.1)$$

where D_{EXC} is the diffusion coefficient of the excitons and τ_{EXC} is the exponential lifetime of an exciton. τ_{EXC} is determined by the reciprocal value of all radiative and non radiative decay rates together. For an efficient solar cell all excitons have to reach the photo-active interface within τ_{EXC}.

The problem that arises when thinner active layers are used is that they absorb a smaller portion of light. The thickness for virtually complete absorption of sunlight is close to 100 nm in organic materials; however, a donor layer of this thickness would result in poor efficiency and most generated excitons would recombine without reaching the interface (see [5] for exact curves of an OSC characteristics vs film thickness). The orientation and

structure of the organic materials contributes in this direction. Rod-like growth, for example, assists excitons to reach the interface before they recombine. **Figure 3.7** depicts this formation schematically.

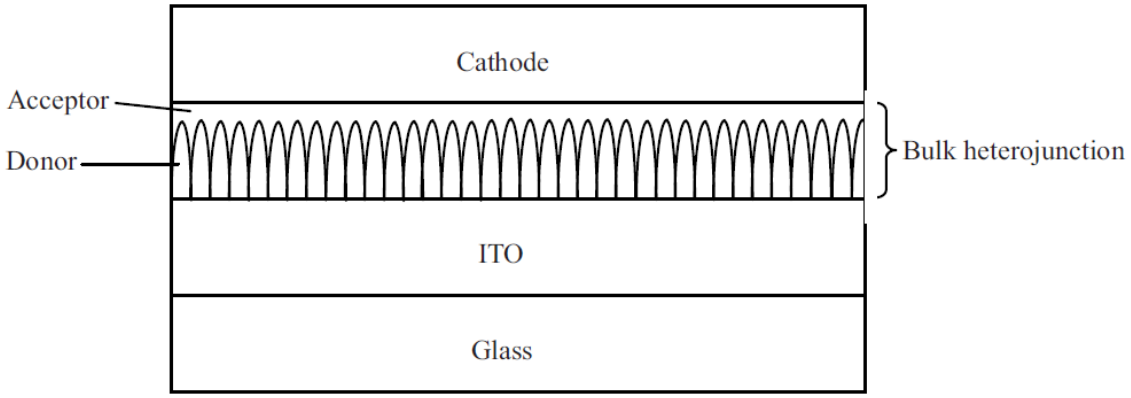

Figure 3.7 ***Bulkheterojunction of vertically oriented stripes of donor and acceptor materials that enables the donor material to be in contact with the ITO electrode and the acceptor layer to be in contact with the aluminum electrode. The acceptor layer could be made using vertically oriented carbon nanotubes [3]***

Once the exciton reaches the interface, the difference between donor and acceptor electron affinities creates the required amount of force needed for charge separation. In the photoinduced electron transfer process, an exciton at the D/A interface decays by creation of the charge-separated state consisting of the radical cation of the donor ($D^{\bullet+}$) and the radical anion of the acceptor ($A^{\bullet-}$)[7]:

$$D + A + h\nu \rightarrow D^{*} + A \left(or\ D + A^{*} \right) \rightarrow D^{\bullet+} + A^{\bullet-}$$

For an efficient charge generation, it is essential that the charge-separated state is the thermodynamically and kinetically most favorite pathway for the exciton. Therefore, it is important that the energy of the absorbed photon is used for generation of the charge separated state and is not lost via competitive processes like fluorescence or non-radiative decay. In addition, the charge-separated state should be stabilized, so that the photogenerated charges can migrate to one of the electrodes. Therefore, the back electron transfer or recombination should be slowed down as much as possible. [7]

After charge dissociation, a charge transfer mechanism comes into play, which drives charge carriers toward electrodes. Light absorption in inorganic photovoltaic (IPV)

cells leads directly to the production of electrons and holes in the same material. Since the two carrier types have the same spatial distribution, the concentration gradient, which is the driving force for the transport by diffusion, is identical (See **Figure 3.8**). Therefore, both charge carriers are driven in the same direction. Since this is a small driving force, in IPV cells, the electrical potential gradient present at the interface of a p-n junction (the band bending) is able to separate the photo-induced electrons from the holes effectively. In contrast to IPV cells, in organic solar cells, after the charge transfer, the electrons and holes are in close proximity. Therefore there is a large chemical potential gradient that drives the charge carriers away from the exciton dissociating interface.

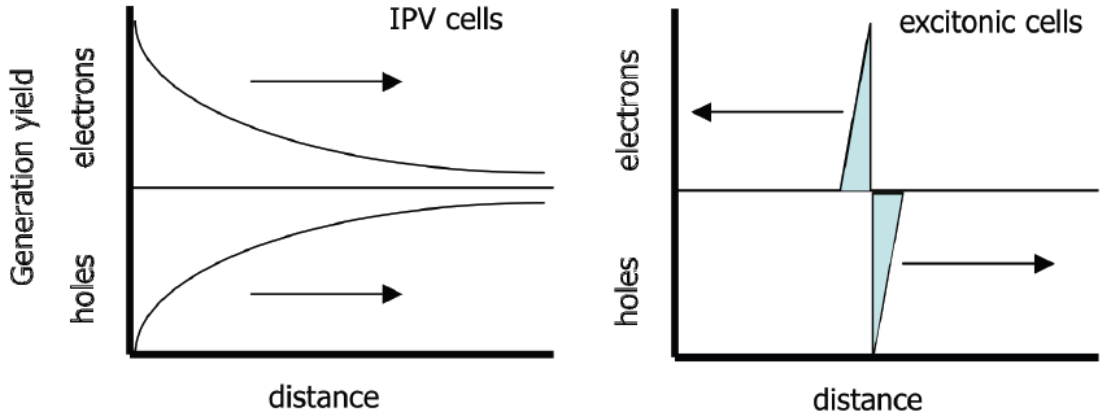

Figure 3.8 Schematic description showing the effect on the charge carrier distributions induced by the different charge carrier generation mechanisms in IPV cells (left) and organic solar cells (right). [7]

Though for IPV cells the electric field is the main driving force for charge transport, it is not yet clear to what extent the internal electrical field contributes to the charge transport in organic solar cells. This is due to the differences in mobilities in molecular materials and inorganic semiconductors. The velocity charge carriers acquire under the influence of an electric field (ξ) is given by the relation [7]:

$$V_{di} = \mu_i \cdot \xi \qquad (3.2)$$

in which μ_i is the mobility. The mobility in molecular materials is relatively small ($< 0.1 cm^2/Vs$) as compared to inorganic semiconductors ($100 – 10000\ cm^2/Vs$). In addition, it is not yet clear, if and how an electrostatic potential in an organic bilayer is formed. This is due to the fact that molecular materials contain only low densities of mobile charge

carriers. In view of the above, the rate kinetics for the various charge carrier recombination processes are important parameters in particular for organic solar cells. These processes should be sufficiently slow, in order to allow the charge carriers to reach the electrodes.[7]

The collection of charge carriers at the electrodes is regularly accomplished by a transparent conductive oxide (TCO) such as ITO or SnO2:F on one side and a metal contact on the other side. Care has to be taken that an Ohmic contact between the electrodes and the molecular layers is formed. In practice, special contact layers have been developed to obtain better performance of the solar cell. Examples of contact layers are a PEDOT:PSS layer, which is a charged conducting polymer layer at the TCO side, and LiF layers at the metal contact side.[7] The exact reason, how these layers improve the cells, is unclear. Apart from that, PEDOT:PSS layer posseses a number of negatives, such as absorption of light in the visible range, degradation problems due to its water absorption even after annealing and the fact that the PSS part of this copolymer is easy to diffuse into other parts of the device and possibly react with other components. [24-25]

Except from PEDOT:PSS, another polymer known as Bathocuproine or BCP is widely used in organic solar cells. BCP is deposited usually with a film thickness of 10nm between the acceptor and the Al electrode. As BCP is a wide-band-gap material, it acts as an exciton-blocking barrier (EBL) that prohibits excitons diffusing towards the Al electrode where they would otherwise be quenched. In some cases, an increase in power-conversion efficiency from 0.05 to 3.0% was observed. [27]

In IPV cells, the V_{OC} (open circuit voltage) is limited by the electrostatic potential at the junction. In organic solar cells, reasonable open circuit voltages have been measured on cells build up by using a single photoactive molecular material and identical electrodes. From this observation, it is evident that the V_{OC} is determined by other factors than for an IPV cell.

For an organic solar cell based on two molecular materials, optical excitation leads to the formation of an exciton in one of the layers. For the charge separation process part of the original energy of the photon is lost, yielding an electron in the n-type material and a positive charge carrier in the p-type material. In case that there is no potential loss at the electrodes, the maximum observed potential can be obtained as shown schematically in ***Figure 3.9***, that is:

V_{max}=ionisation potential of the p-type layer–electron affinity of the n-type layer

In simple HOMO-LUMO diagrams, V_{max} would be crudely approximated by the difference between the energies of the donor HOMO and acceptor LUMO. In practice, a potential loss at the electrodes in the order of 0.2 V is often observed. [7]

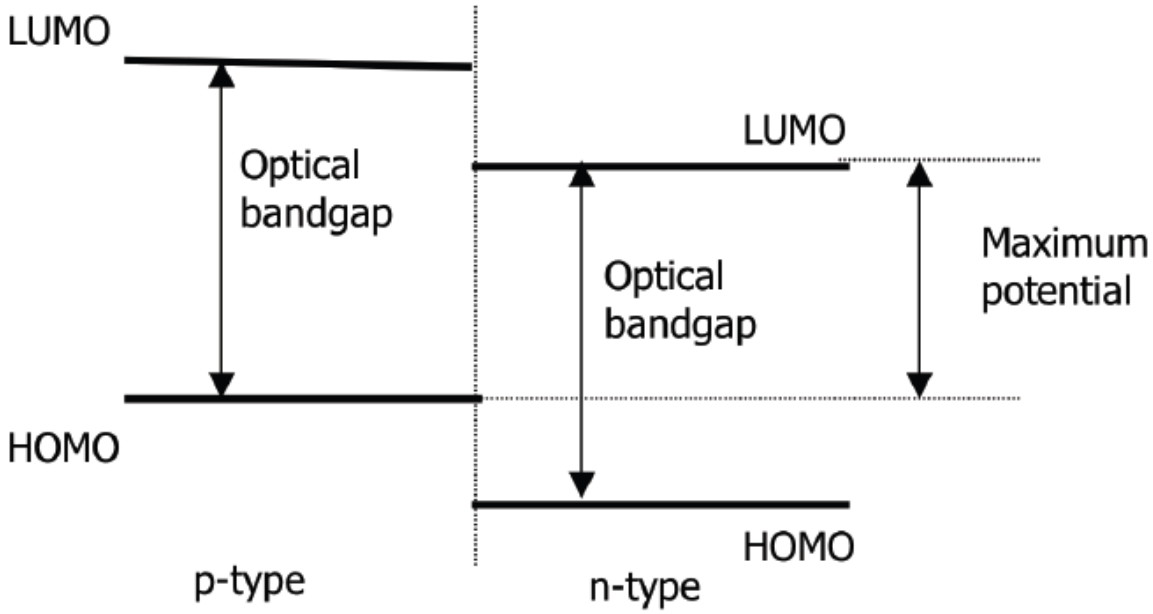

Figure 3.9: Energy levels involved in determining the maximum potential generated by an exciton solar cell. The offset in the energy levels corresponding to LUMO forms the driving force for the dissociation of the exciton [7]

The complete four-step photocurrent generation process starting from an absorbed photon and ending with charges collected at the electrodes is depicted in Figure 3.10, where:

a) the absorption of a photon results in an exciton,
b) the exciton diffuses towards the D–A interface,
c) the bound electron hole pair disassociates into free carriers, and
d) the free carriers transport towards the electrodes for collection

Each of these steps has its corresponding loss mechanism, namely, non-absorbed photons in step a, exciton decay in step b, geminate recombination of the bound pair in step c, and bimolecular recombination in step d. The four phases are interrelated. Improving a single could but not necessarily lead to the overall or expected improvement.

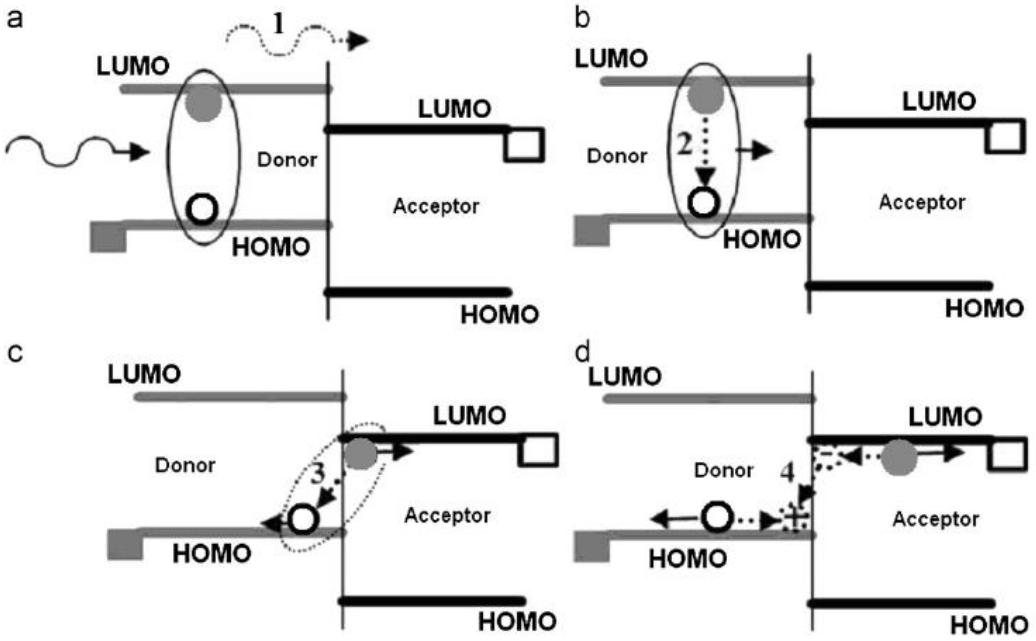

Figure 3.10: The scheme of the operative sequence of an OPVC. The photocurrent generation process is depicted: (a) generation of excitons by photon absorption, (b) diffusion of excitons to the heterojunction, (c) dissociation of the excitons into free charge carriers, and (d) transport of the carriers to the electrodes for collection. Loss mechanisms are also indicated: (1) non-absorbed photons, (2) exciton decays, (3) geminate recombinations of the bound pair, and (4) bimolecular recombinations. [28]

Power conversion efficiency (PCE) coefficient $\eta\%$ depends linearly on three factors: open circuit voltage V_{OC}, short-circuit current I_{SC}, and the filling factor FF:

$$\eta = \frac{J_{\max} \cdot V_{\max}}{P_{inc}} = FF \frac{J_{sc} V_{oc}}{P_{inc}} \qquad (3.3)$$

P_{inc} is the incident power density, while V_{max} and current density J_{max} denote the maximum values for these quantities and their product gives the largest power output:

$P_{max} = V_{max} \cdot J_{max}$. The maximum value for the fill factor is a function of the open circuit voltage V_{OC} and the ideality factor of the diode n (optimally equal to 1). [26]

Figure 3.11 shows the current-voltage (I-V) curves of an organic solar cell under dark and illumination respectively.

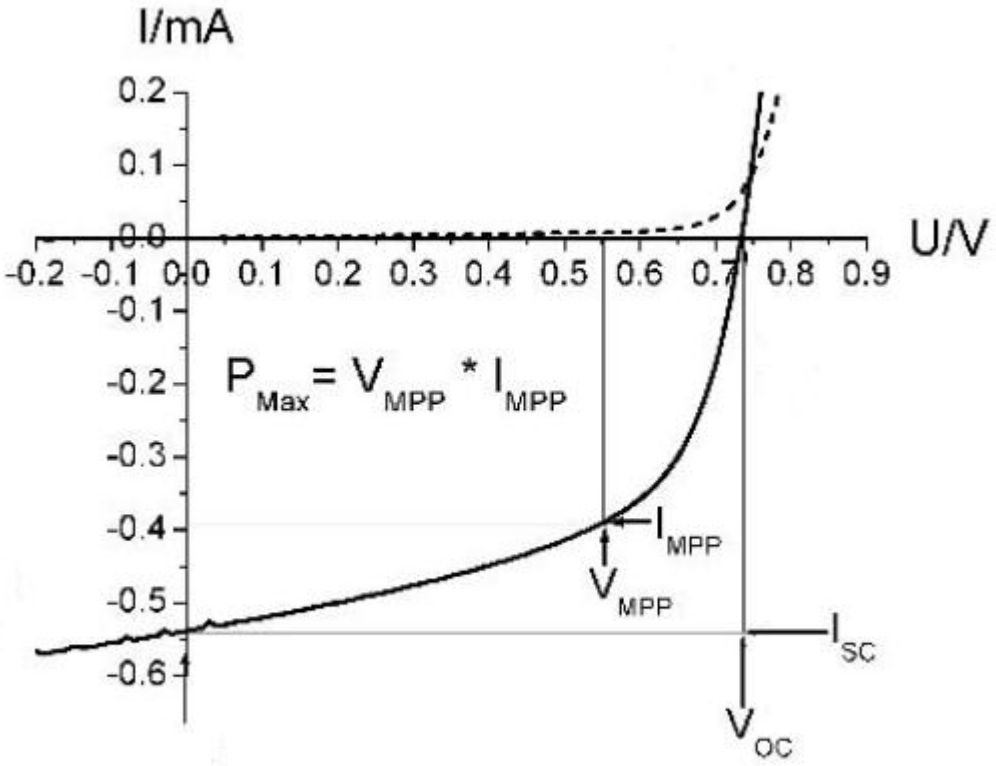

Figure 3.11: Current-voltage (IV) curves of an organic solar cell (dark, dashed; illuminated, full line). The characteristic intersections with the abscissa and the ordinate are the open circuit voltage (V_{oc}) and the short-circuit current (I_{sc}), respectively. The largest power output (P_{max}) is determined by the point where the product of voltage and current is maximized. Division of P_{max} by the product of I_{sc} and V_{oc} yields the filling factor FF. [26]

Closing this chapter, it would be interesting to cite Table 1, which includes current power conversion efficiency records from laboratory results for all the available solar cell technologies. The actual conversion efficiencies in the final mass production should be with caution compared to the lab performance. Nevertheless, the recent increases in efficiency along with the growing research community in OPVCs indicate that commercially viable efficiency of greater than 10% is feasible. According to Heliatek company [21], a new

record of 12% (not included in Table 1) has been achieved. This record was possible using oligomers evaporated under ultra high vacuum. The OSC combines two patented absorber materials, which convert light of different wavelengths. Using two different absorber materials creates a stronger absorption of photons and improves energetic utilization through a higher photovoltage. Thanks to OPV's unique behavior at high temperatures and low light conditions, this 12% efficiency is comparable to about 14% to 15% efficiency for traditional solar technologies like crystalline silicon and thin film PV. Whereas those technologies significantly lose cell efficiency with rising temperatures and decreasing solar radiation, organic cells increase their efficiency under these conditions leading to a much higher energy harvesting in real life environments. [21]

Category	Type	Efficiency (%)	Research organization
Multi-junction concentrators (2-terminal, monolithic)	Three-junction (concentrator)	43.50	Solar Junction
	Three-junction (non-concentrator)	35.80	Sharp
	Two-junction (2-terminal, monolithic)	32.60	FhG-ISE
Single-Junction GaAs	Concentrator	29.10	FhG-ISE
	Thin film crystal	28.80	Alta Devices
	Single crystal	26.40	FhG-ISE
Crystalline Si cells	Single crystal	27.60	Alta Devices
	Silicon Heterostructures (HIT)	23.00	Sanyo
	Multicrystalline	20.40	FhG-ISE
	Thick Si film	16.00	Sharp
Thin-film technologies	Cu(In,Ga)Se2	20.30	ZSW
	CdTe	17.30	First Solar
	Nano-, micro-, poly-Si	17.20	Univ. Stuttgart
	Multi-junction polycrystalline	15.00	NREL
	Amorphous Si:H (stabilized)	12.50	United Solar
Emerging photovoltaic	Dye-sensitized cells	11.80	NTU/Singapore
	Organic cells (various technologies)	10.16	Sumitomo Chemical
	Inorganic cells	10.00	IBM
	Organic tandem cells	8.60	UCLA
	Quantum dot cells	5.10	Univ. of Toronto

Table 1 Best research-cell efficiencies compiled from National Renewable Energy Laboratory's chart 2012/5. [28]

Chapter 4 Characterization methods

In this chapter, the methods used for characterization of samples and devices are presented. These methods are divided into two main categories: The first one, is Scanning Probe Microscopy, a term that is used to describe a technique where scanning of a surface with a sharp probe leads to a schematic representation of the structure along with the properties of the surface. Atomic Force Microscopy and Scanning Tunneling Microscopy are the most common representatives. The second category consists of techniques used to characterize the optical properties of a sample such as light absorption spectra and reflectivity. UV-Visible Spectroscopy, Photoreflectance-Photoluminescence spectroscopy (PR-PL) and Electroreflectance (ER) methods are being introduced.

4.1 Scanning Probe Microscopes

4.1.1 Atomic Force Microscopy (AFM)

Atomic Force Microscopy was developed in 1986 by Binning, Quate, and Gerber as collaboration between IBM and Stanford University. AFM relies on the ability to sense small forces. A cantilever with a sharp tip provides the means for sensing forces exerted on the tip by the atoms in the sample. To register small inter-atomic forces, the cantilever probe must be insensitive to extraneous disturbances from the surrounding environment. These disturbances are caused by sources such as building vibrations, whose power spectral density is significant in the frequency range 0–2 kHz. Therefore, to avoid the effects of these disturbances, the resonance frequency of the cantilever must be greater than 2 kHz. At the same time, the cantilevers need to be sufficiently compliant to sense the inter-atomic forces. The forces between the tip of the cantilever and the sample are in the range 10^{-7} – 10^{-12} N. To produce a deflection greater than 1 Å for a force of 10^{-12} N, the spring constant k of the cantilever must be less than 0.01 N/m. A stiffness of 0.01 N/m and a resonance frequency of 2 kHz imply a mass less than 10^{-10} kg. These requirements are met by microcantilevers, which are typically made of silicon nitride and silicon oxide, and are batch fabricated using microfabrication techniques. Typical length, width, and thickness of microcantilevers used in AFM are 100, 10, and 2 μm, respectively. The stiffness of the microcantilevers can vary from 0.06 to 100 N/m. [29]

A typical AFM setup is shown in **Figure 4.1**. The prevalent method for measuring the cantilever deflection uses a laser beam, which is focused on the cantilever and is reflected from the cantilever surface into a split photodiode. The cantilever deflection changes the angle that the incident laser beam makes with the cantilever surface, which, in turn, changes the incidence position on the photodiode, which is registered as a change in the photodiode voltage. The length of the reflected laser path amplifies the cantilever deflection. [29]

The fixed end of the cantilever is supported by the *base*, which is typically attached to a *dither piezo* (Figure 4.1). The dither piezo provides a means for oscillating the base of the cantilever. A scanner, which is actuated by piezoelectric material, positions the sample laterally and vertically during imaging. [29]

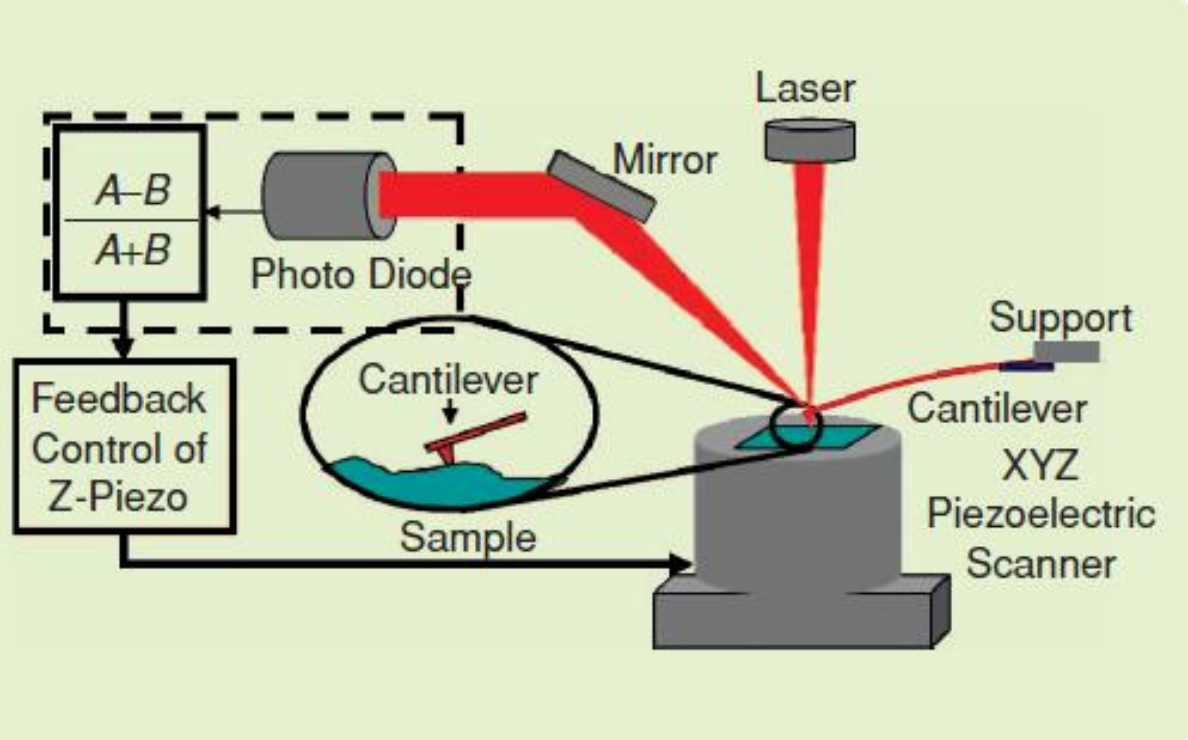

Figure 4.1 Atomic force microscope. The atomic force microscope yields atomic-resolution imaging capability for both conductors and insulators. The main probe of an atomic force microscope is a microcantilever, which deflects due to forces between the atoms on the sample and the atoms on the tip. The deflection of the cantilever is registered by a laser incident on the cantilever, which reflects onto a split photodiode. The cantilever support can be forced using the dither piezo. The control signal, which regulates a reference set-point by moving the sample vertically relative to the cantilever probe, gives a measure [29] of the sample topography. A piezo scanner positions the sample relative to the cantilever in the lateral and the vertical directions.

The cantilever is a flexure member whose first mode is described by the spring-mass-damper dynamics:

$$\ddot{p} + \frac{\omega_0}{Q}\dot{p} + \omega_0^{\,2} \cdot p = f(t) \qquad (4.1)$$

$$y = p + \upsilon$$

where p, f, y, and υ denote the deflection of the tip, force on the cantilever, measured deflection, and measurement noise, respectively, whereas the parameters ω_0 and Q are the first modal frequency (resonance frequency) and quality factor of the cantilever. The quality factor characterizes the energy loss of the cantilever to the surrounding environment. The first modal frequency of typical cantilevers used in AFM is in the range 10–400 kHz, while Q can range from 2 in a liquid environment to 10,000 or higher under vacuum. The measurement noise υ is dominated by 1/f noise at low frequencies and is nearly white at frequencies beyond a few kilohertz. The cantilever model (Eq.(4.1)) can be identified

precisely. Viewing the cantilever as a filter (Eq.(4.1)) proves crucial for employing systems and control perspectives to AFM. [29]

The interaction force between the tip and the sample can be characterized by the Lennard-Jones force:

$$F(r) = \frac{-6A}{r^7} + \frac{12B}{r^{13}} \tag{4.2}$$

where r is the separation between the tip and the sample. The term $-A/r^7$ models the Van der Waals interaction that characterizes the attractive force between the atoms of the tip and the sample. The effect of these long-range forces is perceptible when two atoms are separated by distances smaller than 10 nm. At separations smaller than 1 Å, the overlap of electron clouds and ionic interactions causes strong repulsive forces between atoms on the cantilever and atoms on the sample surface. The effect of the repulsive forces is captured by the term B/r^{13} in the Lennard-Jones model. This model provides a good qualitative characterization of the tip-sample interaction, notwithstanding the diverse factors that cause experiments in AFM to deviate from this model. [29]

There are 3 different operation modes of Atomic Force Microscopy depending on the interaction regime. Contact mode, intermittent-contact or tapping mode, and non-contact mode shown in **Figure 4.2** as a function of force vs tip-sample distance.

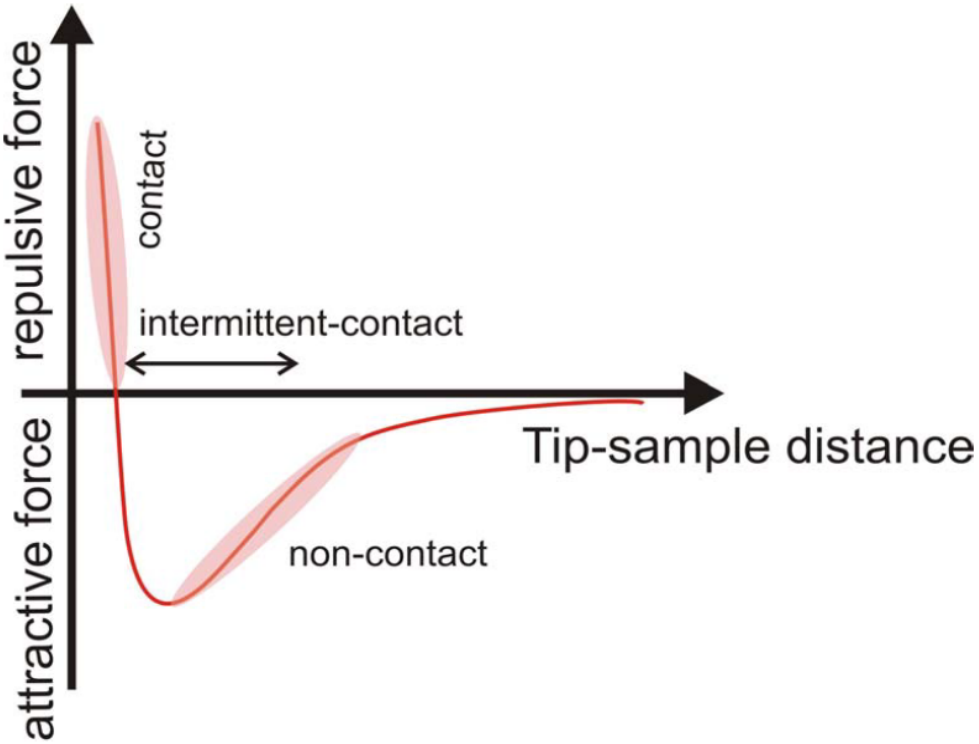

Figure 4.2 A schematic describes the Lennard-Jones force vs tip-sample distance.[1]

In the following, the advantages and disadvantages of each method will be analyzed. [30]

Contact mode

Advantages:

- High scan speeds (throughput).
- Contact mode AFM is the only AFM technique which can obtain "atomic resolution" images.
- Rough samples with extreme changes in vertical topography can sometimes be scanned more easily in contact mode.

Disadvantages:

- Lateral (shear) forces can distort features in the image.
- The forces normal to the tip-sample interaction can be high in air due to capillary forces from the adsorbed fluid layer on the sample surface.
- The combination of lateral forces and high normal forces can result in reduced spatial resolution and may damage soft samples (i.e., biological samples, polymers, silicon) due to scraping between the tip and sample.

Tapping mode

Advantages:

- Higher lateral resolution on most samples (1nm to 5nm).
- Lower forces and less damage to soft samples imaged in air.
- Lateral forces are virtually eliminated, so there is no scraping.

Disadvantages:

- Slightly slower scan speed than contact mode AFM.

Non-contact Mode

Advantages:

- No force exerted on the sample surface.

Disadvantages:

- Lower lateral resolution, limited by the tip-sample separation.
- Slower scan speed than Tapping Non-contact usually only works on extremely hydrophobic samples, where the adsorbed fluid layer is at a minimum. If the fluid layer is too thick, the tip becomes trapped in the adsorbed fluid layer causing unstable feedback and scraping of the sample.

Due to the nature of disadvantages that non-contact mode exhibits, applications for this mode have been limited. On the other hand contact mode can damage organic samples, which are very sensitive. It is easily understood that tapping mode is the preferable one for structure imaging. It operates by scanning a tip attached to the end of an oscillating cantilever across the sample surface. The cantilever is oscillated at or slightly below its resonance frequency with amplitude ranging typically from 20nm to 100nm. The tip lightly "taps" on the sample surface during scanning, contacting the surface at the bottom of its swing. The feedback loop maintains constant oscillation amplitude by maintaining a constant RMS of the oscillation signal acquired by the split photodiode detector. The vertical position of the scanner at each (x,y) data point in order to maintain a constant "setpoint" amplitude is stored by the computer to form the topographic image of the sample surface. By maintaining a constant oscillation amplitude, a constant tip-sample interaction is maintained during imaging. Operation can take place in ambient and liquid environments. In liquid, the oscillation need not be at the cantilever resonance. When imaging in air, the typical amplitude of the oscillation allows the tip to contact the surface through the adsorbed fluid layer without getting stuck. [30]

4.1.2 Scanning tunneling microscopy (STM)

Scanning tunneling microscopy (STM) was first developed in 1982 by Binning, Rohrer, Gerber, and Weibel at IBM in Zurich, Switzerland. Binning and Rohrer won the Nobel Prize in Physics for this invention in 1986. The invention of the scanning tunneling microscope (STM) is a significant step in realizing the vision of atomic-scale interrogation of materials. The STM uses the quantum-mechanical phenomenon of *tunneling current*. Tunneling current is caused by the flow of electrons from the surface of one material to the surface of another even when the surfaces are not in contact with each other. The magnitude of the tunneling current is appreciable when the separation between the surfaces is on the order of a few nanometers. In scanning tunneling microscopy, the tunneling current flows between the *sample*, which is the material being imaged, and the *probe*, which is positioned above the sample. The STM determines the topography of the material by using the dependence of the tunneling current on the separation between the two surfaces. Earlier attempts to use tunneling current to image material with atomic-scale resolution were not successful due to

extraneous vibrations that made it difficult to maintain a small separation between the probe and the sample. The use of STM is limited to conductors and semiconductors, in contrast with the ability of AFM to image insulators also. [29]

The tunneling current I_T in terms of the separation z between two surfaces is given by:

$$I_T(z) = I_0(V)e^{-2\kappa z} \tag{4.3}$$

where the parameters κ and $I_0(V)$ are material-dependent constants and V is the voltage difference across the two surfaces. For a typical conducting material, κ is on the order of 10^{10} m^{-1}. The large exponent κ implies that the contribution to the tunneling current decreases by a factor of ten for an atom that is two atomic dimensions farther from the tip. Since most of the contribution to the tunneling current is due to the atom on the sample surface that is closest to the tip, STM can determine the sample topography with atomic resolution. [29]

Since a sample is typically tilted, it is difficult to move the sample laterally without either losing proximity between the tip and the sample or impacting the tip into the sample. Another practical difficulty in using the tunneling current to image the topography of the sample is the nonlinear dependence of the tunneling current on the sample height. Only the qualitative behavior of the relation (1) is known, which limits the ability to determine the topography of the sample from the tunneling current. [29]

Scanning tunneling microscopy uses feedback to overcome the practical difficulties that limit the use of tunneling current. In STMs, a feedback scheme is used to vertically position the sample with respect to the tip with the objective of maintaining a constant current (**Figure 4.3**). During a scan, when the sample is moved laterally under the tip, the controller attempts to maintain a constant current by moving the sample vertically in a manner that compensates for variations in the topography of the sample. Thus, during scanning, when the separation between the sample and the tip decreases or increases due to variations in the sample topography, the control signal regulates the current by actuating the positioning device away from or toward the tip. For typical speeds of operation, the compensating control signal is proportional to variations in the topography and therefore provides a measure of the sample topography. This feedback scheme restricts the movement of the tip to a small region around an operating point of the current-separation curve described by (1), and, therefore, linear behavior of the current with respect to separation z can be assumed. The linearizing effect is a significant advantage of the control loop. [29]

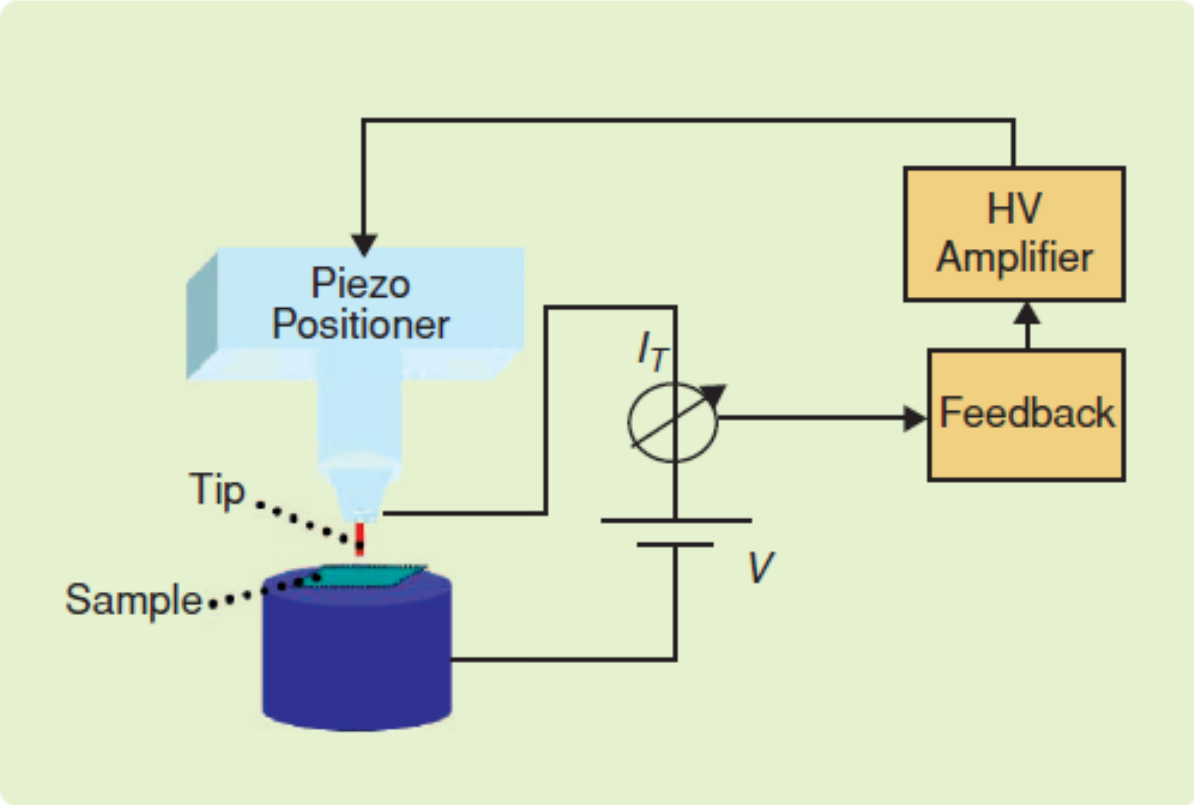

Figure 4.3 Scanning tunneling microscope.

The STM feedback mechanism requires a positioning device that provides sub-angstrom resolution at an acceptable bandwidth. Piezoelectric elements provide such a high positioning resolution. A contribution of early STM experiments is confirmation that piezoelectric material can be deformed with the required resolution. [29]

In practise, the operation of a scanning tunnelling microscope can be simulated throughout energy level diagrams between sample and tip, as shown in **Figure 4.4.**

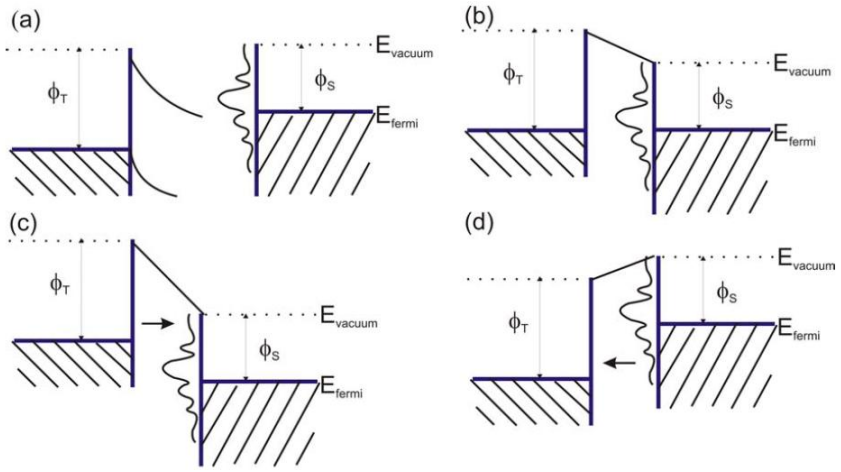

Figure 4.4 Energy level diagram for sample and tip. [1]
(a) Independent sample and tip.
(b) Sample and tip at equilibrium, separated by small vacuum gap.
(c) Positively biased sample: electrons tunnel from tip to sample.
(d) Negatively biased sample: electrons tunnel from sample to tip.

4.2 Optical characterization

4.2.1 Modulation spectroscopy

Photoreflectance (PR) – Electroreflectance(ER)

In order to understand the properties of microstructures, it is important to have as much information as possible about their band structure. This usually involves inter-band measurements, such as photoluminescence excitation spectroscopy (PLE), modulation spectroscopy, absorption and reflection spectroscopy. In the case of bulk semiconductors, modulation spectroscopy was highly successful in obtaining maps of the band structure of various semiconductors (Cardona, 1969; Seraphin, 1972). [32]

Photoreflectance (PR) is a simple, practical, flexible, contactless modulation spectroscopy technique, which at the same provides a lot of useful information. It was first introduced in the 1960s, and first used in investigations of semiconductors band structure parameters during 1970s. In 1985, Glembocki reported the first application of this technique in semiconductors microstructures studies. [31]

In general, with modulation spectroscopy, the derivative of the absorptivity or reflectivity with respect to some parameter is evaluated. This spectroscopy has been shown to be sensitive to critical point transitions in the Brillouin zone, with the resulting spectrum having sharp derivative-like features and little, if any, featureless background. Also, weak features that may have been difficult to observe in the absolute absorption or reflection spectrum can be enhanced. Because of this derivative-like nature, a large number of sharp spectral features can be observed even at room temperature. In addition, there is also information on the other experimental variables such as the modulation frequency, amplitude, and phase. [32]

The modulation can easily be accomplished by varying some parameter of the sample or experimental system in a periodic fashion and measuring the corresponding normalized change in the optical properties. While it is possible to modulate a variety of parameters, including the wavelength of the incident beam, the sample temperature, an applied stress, or applied magnetic field, we are basically interested in a modulation of either an externally applied electric field or a photoinduced variation in the built-in electric field. [32]

Figure 4.5 shows a comparison of reflectivity and electroreflectance (ER) spectra for GaAs over the same photon energy range (Phillip, 1963). While the reflectivity is characterized by broad features, the ER spectrum is dominated by a series of very sharp lines with zero signal as a baseline. Notice, that much of the broad featureless background of the reflectivity measurement is not present in the ER spectrum. Herein lies the power of modulation spectroscopy: uninteresting background structure is eliminated in favor of sharp lines corresponding to specific transitions in the Brillouin zone. While it is difficult to calculate a full reflectance spectrum, this is not the case for modulation spectra. For well-known critical points in the Brillouin zone, it may be possible to account for the line shapes in a modulation spectrum (Cardona, 1969). [32]

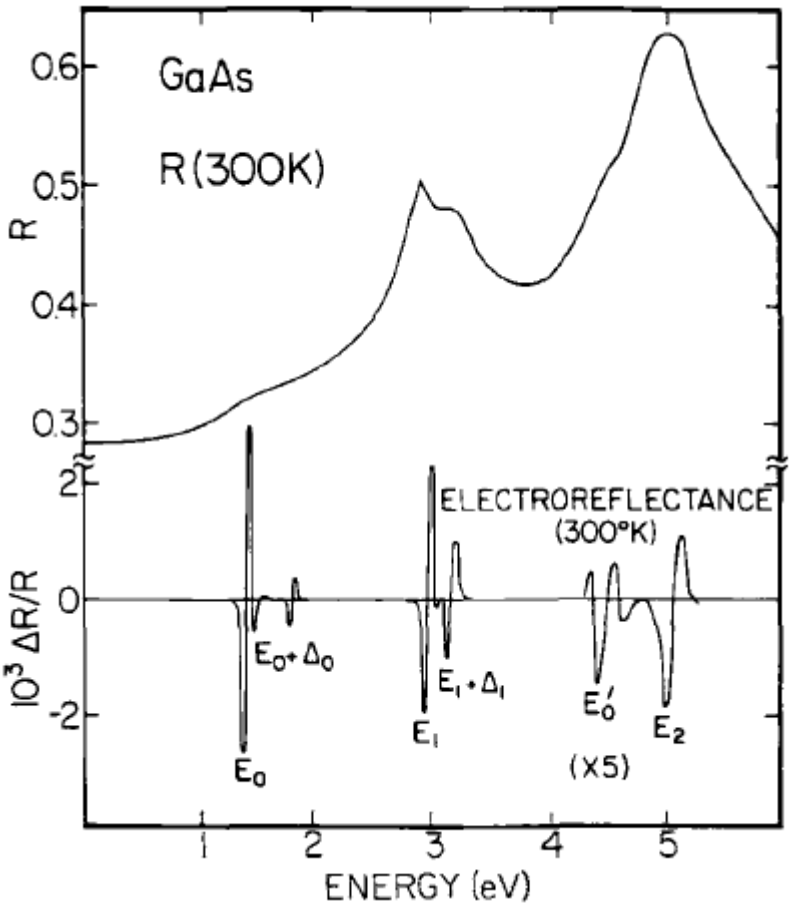

Figure 4.5 Room temperature reflectivity (top) and electroreflectance (bottom) spectra of GaAs. (Phillip and Ehrenreich, 1963.) [32]

Differential changes in the reflectivity can be related to the perturbation of the complex dielectric function in a simple manner, as expressed by Seraphin and Bottka (1966):

$$\frac{\Delta R}{R} = a \cdot \Delta\varepsilon_1 + \beta \cdot \Delta\varepsilon_2 \qquad (4.4)$$

where R is the reflectivity, $\Delta\varepsilon_1$ and $\Delta\varepsilon_2$ are changes in the complex dielectric function $\varepsilon = \varepsilon_1 + i\varepsilon_2$, and α and β are the Seraphin coefficients, which are related to the unperturbed dielectric function. Near the fundamental gap of bulk materials, $\beta \approx 0$, so that $\Delta R/R \approx a \cdot \Delta\varepsilon_1$ is the only important term. However, in multilayer structures interference effects are prevailing, so that the Seraphin coefficients are modified and both $a \cdot \Delta\varepsilon_1$ and $\beta \cdot \Delta\varepsilon_2$ may have to be considered. The exact functional form of $a \cdot \Delta\varepsilon_1$ and $\beta \cdot \Delta\varepsilon_2$ can be calculated provided that the dielectric function and type of the critical point are known. In the next sections, we will derive expressions for $\Delta\varepsilon_1$ and $\Delta\varepsilon_2$. [32]

In modulation spectroscopy, one often encounters discussions that revolve around the "phase of the line shape". As one can see, from Eq. (4), the modulated reflectivity can be a mixture of $\Delta\varepsilon_1$ and $\Delta\varepsilon_2$. The modulation spectroscopy phase, therefore, represents the fraction of $\Delta\varepsilon_1$ and $\Delta\varepsilon_2$ that constitutes to the observed line shape. A further complication can arise in systems, in which the modulating parameter (e.g., electric and magnetic fields, stress, or temperature) can produce changes in several properties of the system. For example, in quantum wells, the electric field not only shifts the band gap, but it also changes the oscillator strength. This type of effect will also mix different line shapes into the modulated reflectivity. Therefore, the modulated reflectivity phase contains information not only about the Seraphin coefficients, but also about optical interference, as well as modulation mechanisms. [32]

As mentioned already, modulation techniques take advantage of the application of a small periodic perturbation to a physical property of the sample. The change in the optical function (reflectivity or absorptivity) is only a small fraction of its unperturbed value, typically 1 part in 10^4. The perturbation is usually extracted through the use of a lock-in amplifier tuned to the modulating frequency. This aspect of modulation spectroscopy is common to all techniques, including electroreflectance, photoreflectance, wavelength modulation, piezoreflectance, and thermoreflectance. In electroreflectance, an applied

electric field is modulated to produce a periodic variation in the dielectric function, while in photoreflectance this modulation is accomplished through the production of photoexcited carriers. The experimental apparatus for photoreflectance spectroscopy is shown in **Fig. 4.6.**

The probe light is a monochromatic beam obtained from either a tungsten lamp or a quartz halogen source dispersed through a monochromator. For most routine applications, a monochromator having a focal length of 1/4 m is adequate. At low temperatures, excitons can exhibit narrow line widths and a 0.85m or 1m monochromator is better. The light impinging on the sample has intensity I_0. The modulation (electric field, temperature stress, etc.) is applied to the sample at a frequency Ω_m. [32]

The reflected light is detected by a photomultiplier or a suitable photodiode. In most cases a Si PIN diode is often used. The light striking the detector contains two signals: a dc or average value, I_0R, and a modulated value, $I_0\Delta R$, which varies with the frequency Ω_m.

Since the quantity $\Delta R/R$ is of interest, it is necessary to eliminate the common factor I_0. This normalization can be accomplished in two different ways: The simplest, although the most time-consuming, manner is to measure ΔR and R independently and to divide the two quantities. The drawback of this technique becomes evident, because it requires two measurements and it is always more difficult to rely on ratioing, especially in the case of a light source such as a Xe arc lamp, which has many sharp lines. A more elegant method of obtaining $\Delta R/R$ is to simultaneously measure both quantities: ΔR and R. Since the magnitude of R is varied during an energy scan and may diminish at certain energies, it is important to keep *R* constant electronically. This can be accomplished in one of three ways: In the first technique, the dc output of the photomultiplier tube (PMT) is kept constant through a servomechanism that compares the dc background output to a reference voltage and uses the difference between the two to change the gain of the PMT. This idea holds also in the second technique and can be applied to a photo-diode through the use of a programmable gain amplifier. A third technique involves keeping the dc intensity of the reflected light constant through the use of a continuously variable neutral density filter placed after the monochromator (Shen et al., 1987a,b). This circular filter is rotated by a servomotor driven by the voltage difference between the dc signal and a fixed reference signal as illustrated in **Fig. 4.6**. Both of the electronic servo techniques result in the output of the lock-in amplifier being proportional to $\Delta R/R$. [32]

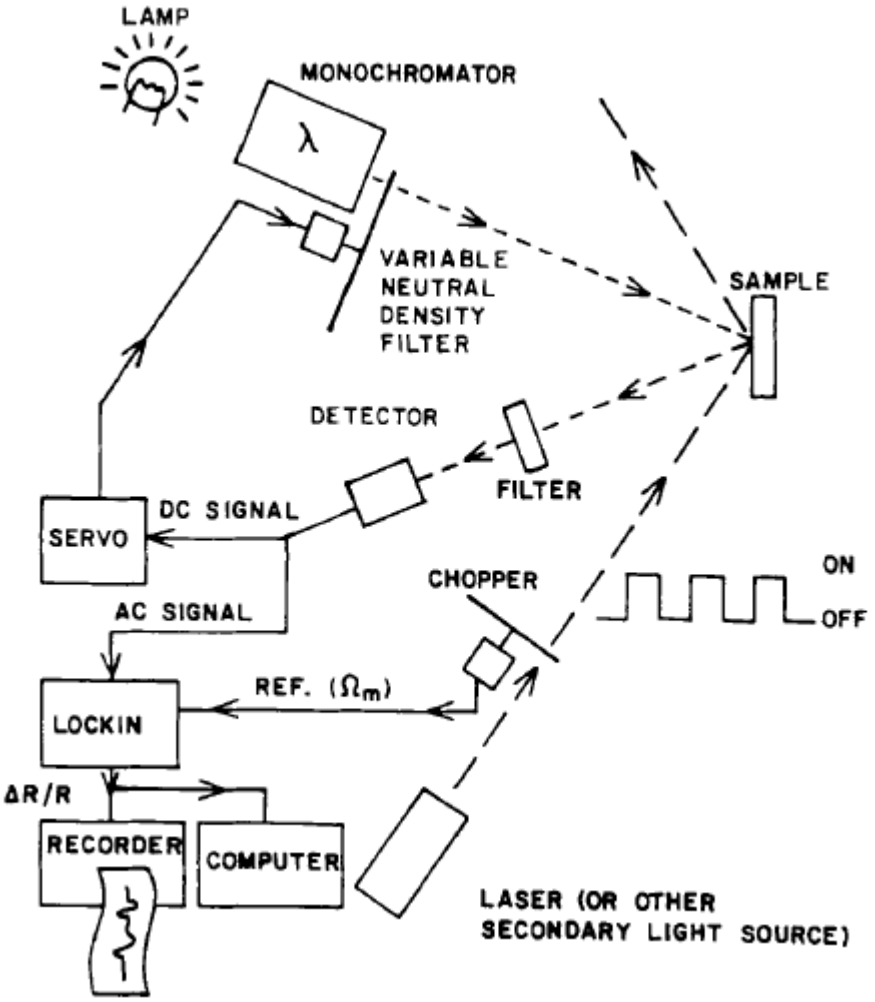

Figure 4.6 Schematic diagram of the photoreflectance apparatus. Monochromatic light is used as a probe. Its intensity is kept constant by a variable neutral density filter, which is controlled by a servomechanism. The pump is provided by a chopped laser having a frequency Ω_m. The lock-in is tuned to Ω_m and detects the reflected light at this frequency. (Shen *et al.*, 1987a,b.) [32]

In the case of photoreflectance, it is important for the apparatus to have good filtering of the stray laser light, because it has the same frequency (chopped) as the signal of interest and can easily be detected. Furthermore, laser illumination can produce band-gap photoluminescence, which under certain conditions is greater in intensity than the signal of interest. This problem can be eliminated by using long-focal-length optics or by using a second monochromator running in unison with the probe monochromator (Theis et al., 1988). For a double monochromator, two scans are taken, one with the probe light on and one without it. Subtracting, the two traces effectively eliminates the PL. An alternative technique involves using a dye laser as the probe beam and a detector placed sufficient far away from the sample so as to reduce the PL, which is usually emitted isotropically (Shanabrook *et* al.,1987a; Glembocki and Shanabrook, 1987b). [32]

4.2.2 Ultraviolet-Visible (UV-VIS) Spectroscopy

With UV-VIS spectroscopy it is possible to investigate electron transfers between orbitals or bands of atoms, ions, and molecules in the gas phase as well as in liquids and solids. The spectral region of 250 to 800 nm is of special interest for in situ UV-VIS spectroscopy. Investigations of solutions and crystals usually take place in transmission, whereas powder samples are often measured in diffuse reflections (DRS: diffuse reflectance spectroscopy). A significant advantage of UV-VIS spectroscopy lies in the individual detection of electron transfers without superimposition by neighboring vibrational bands. Unlike IR spectroscopy, where the use of Fourier transform techniques predominates, dispersive spectrometers are almost exclusively applied for UV-VIS spectroscopy because of the large band widths. [33-35]

The energy of the radiation can be calculated by the equation $E = h \nu$. This energy irradiated on the molecules can result in changes in the electronic nature of the molecule i.e. changes between ground state and excited states of electrons within the system. As a result, UV-VIS spectroscopy is also known as electronic spectroscopy. [33-35]

Every time a molecule has a bond, the atoms in a bond have their atomic orbitals merged to form molecular orbitals which can be occupied by electrons of different energy levels. Ground state molecular orbitals can be excited to anti-bonding molecular orbitals. [33-35]

The electron bonds in a molecule can be of one of three types: namely σ (single bond), π (multiple-bond), or non-bonding (n- caused by lone pairs). These electrons when imparted with energy in the form of light radiation get excited from the highest occupied molecular orbital (HOMO) to the lowest unoccupied molecular orbital (LUMO) and the resulting species is known as the excited state or anti-bonding state. [33-35]

1. σ-bond electrons have the lowest energy level and are the most stable electrons. These would require a lot of energy to be displaced to higher energy levels. As a result these electrons generally absorb light in the lower wavelengths of the ultraviolet light and these transitions are rare.
2. π-bond electrons have much higher energy levels for the ground state. These electrons are therefore relatively unstable and can be excited more easily and would require lesser energy for excitation. These electrons would therefore absorb energy in the ultraviolet and visible light radiations.

3. n-electrons or non-bonding electrons are generally electrons belonging to lone pairs of atoms. These are of higher energy levels than π-electrons and can be excited by ultraviolet and visible light as well.

Most of the absorption in the ultraviolet-visible spectroscopy occurs due to π-electron transitions or n-electron transitions. Each electronic state is well defined for a particular system. **Figure 4.7** below shows the different transitions between the bonding and anti-bonding electronic states. [33-35]

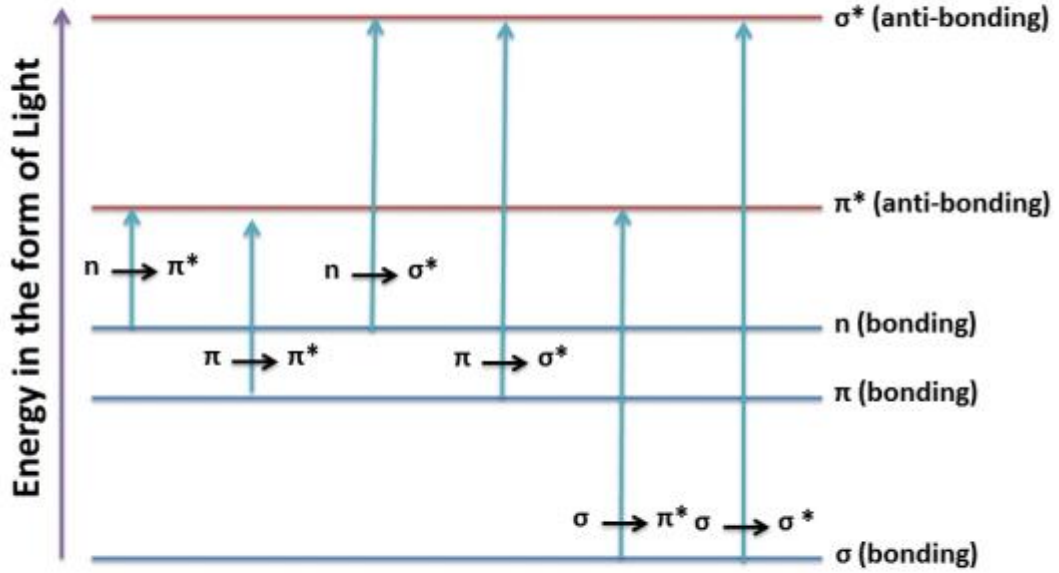

Figure 4.7 Different transitions between the bonding and anti-bonding electronic states when light energy is absorbed in UV-Visible Spectroscopy.

When a sample is exposed to light energy that matches the energy difference between a possible electronic transition within the molecule, a fraction of the light energy would be absorbed by the molecule and the electrons would be promoted to the higher energy state orbital. A spectrometer records the degree of absorption by a sample at different wavelengths and the resulting plot of absorbance (A) versus wavelength (λ) is known as a spectrum. The wavelength at which the sample absorbs the maximum amount of light is known as $\lambda_{max.}$ For example, shown in **Fig. 4.8** below, is the spectrum of isoprene. Isoprene is colourless, as it does not absorb light in the visible spectrum, and has a λ_{max} of 222nm. [33-35]

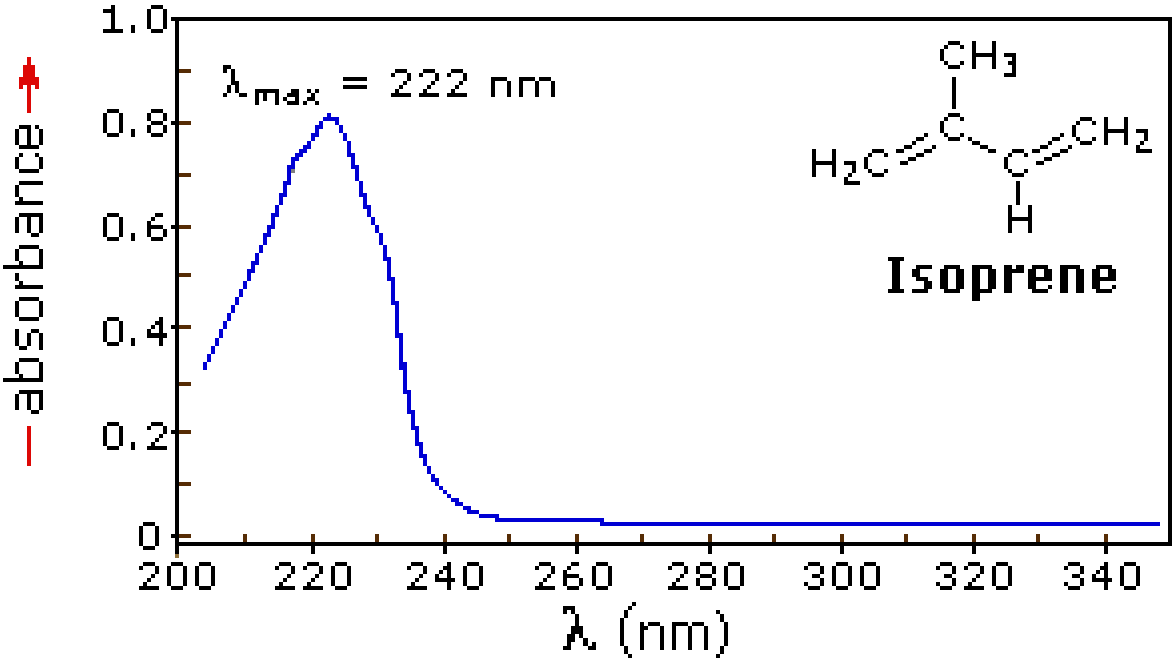

Figure 4.8 UV-VIS spectrum of isoprene showing maximum absorption at 222 nm.

Chapter 5 Experimental details

This chapter introduces the laboratories and the experimental systems that were used for the experiments to be carried out through the present diploma thesis. They will be presented in the following order: organic thin film growth upon thermal evaporation in Ultra High Vacuum systems (UHV), structural and morphological characterization with AFM, optical characterization and investigation of properties with modulation spectroscopy techniques (PR-ER), search for single organic molecular orientation with the STM under UHV and finally with Organic Solar Cell (OSC) fabrication and performance characterization.

5.1 Ultra High Vacuum systems (HZB)

Thin films of organic semiconductors were grown by thermal evaporation in high vacuum chambers.

Organic semiconductor film growth experiments were carried out at the Laboratories of the **Institute of Heterogeneous Materials Systems in the Solar Energy Research Section of Helmholtz-Zentrum Berlin für Materialien und Energie (HZB), under the Direction of Prof. Dr. M.-Ch. Lux-Steiner and the Assistance of Dr. K. Fostiropoulos.**

Figure 5.1 shows the experimental small chamber where layers of a-sexithiophene were grown. The pump on this chamber was able to reach high vacuum in the order of 10^{-5}-10^{-6} mbar. Inside the chamber, a sample holder is installed, with integrated heating elements for deposition at increased substrate temperature, if desired. The holder can carry only one sample each time. In order for a sample to be loaded, the vacuum must be broken unavoidably. This has as consequence loss of time for the next evaporation until vacuum reaches maximum values. On the other hand, such a simple system is easily manipulated, controlled, and opened for maintenance. Furthermore, the chamber is equipped with a quartz crystal microbalance (QCM) for monitoring the film thickness and two Knudsen cells (crucibles) for evaporating organic materials and metal. The quartz crystal microbalance must be calibrated for each material. This is mainly done with X-Ray Reflectivity (XRR) measurements of layer thickness and using the density of the material. **Figure 5.2** presents the sample holder and **Figure 5.3** the Knudsen cells.

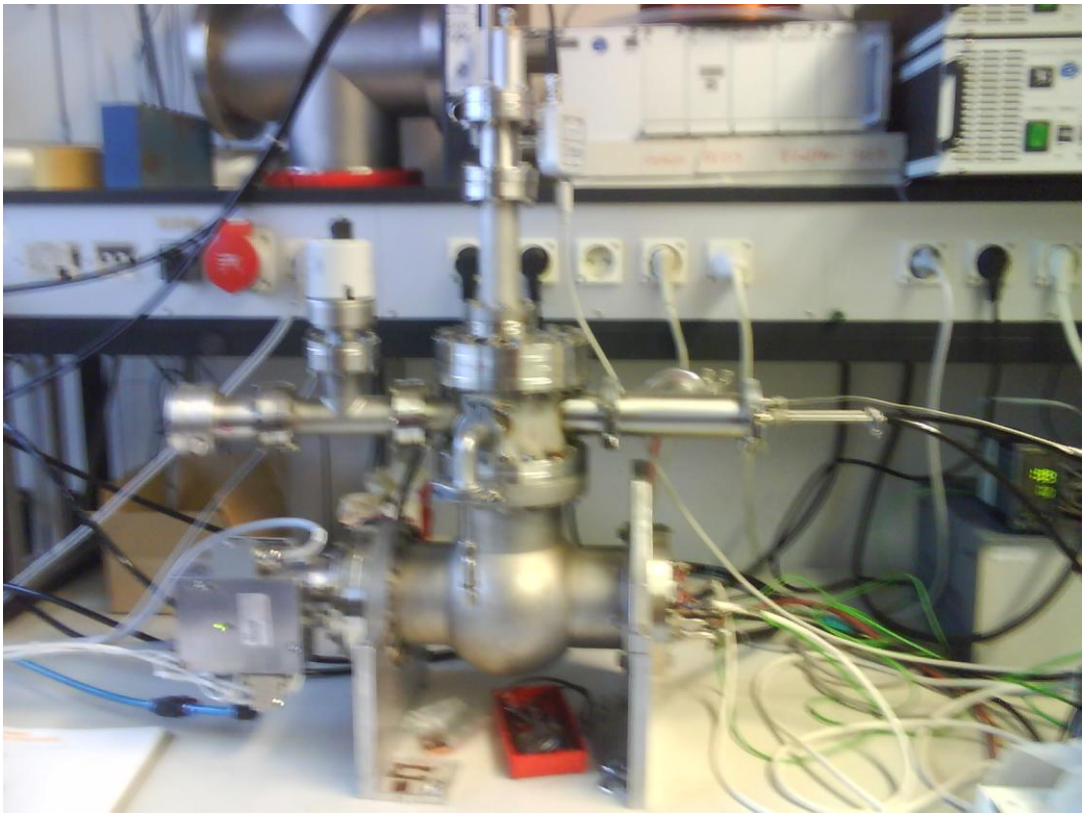

Figure 5.1 Small, high vacuum chamber at HZB.

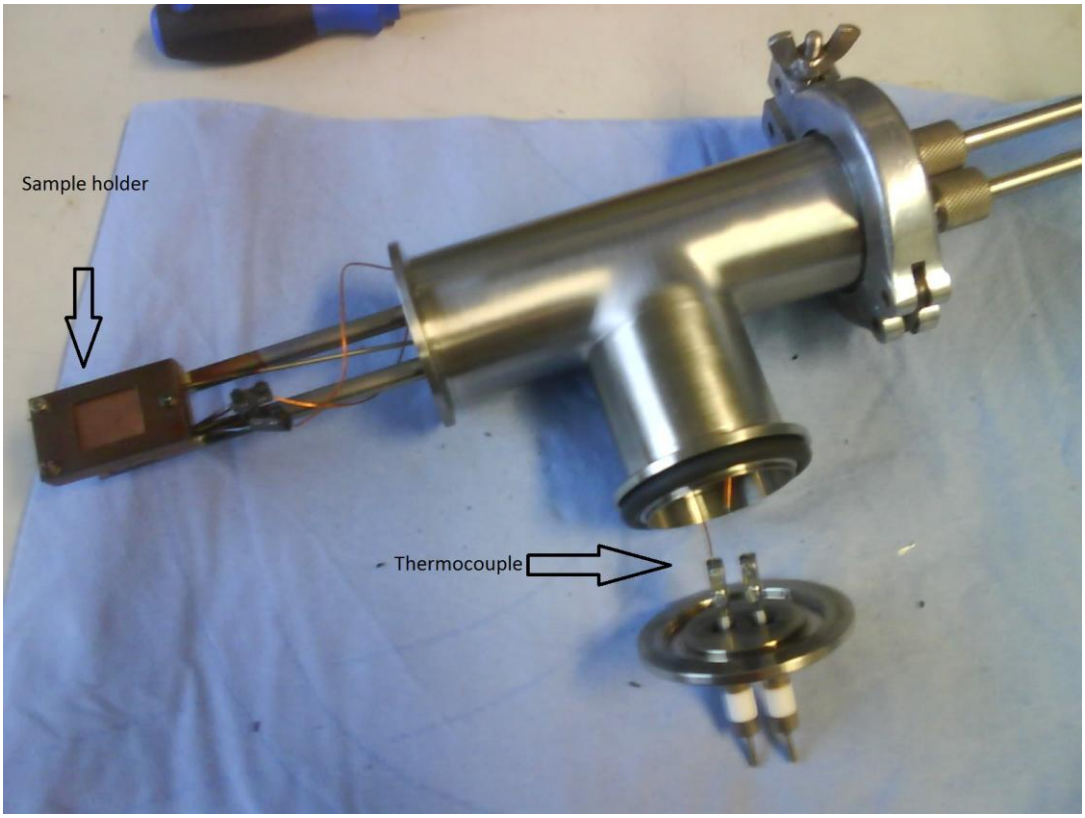

Figure 5.2 Sample holder and thermocouple.

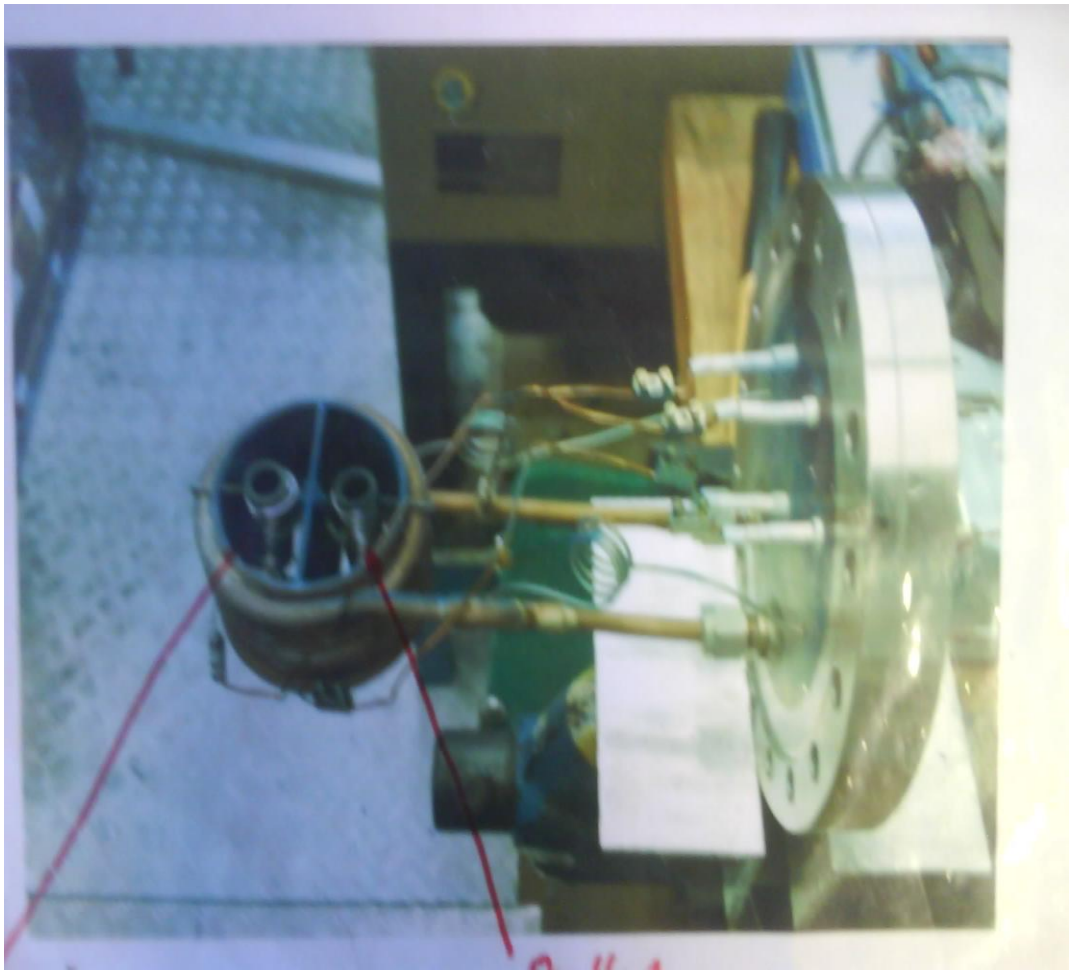

Figure 5.3 Knudsen cells for the evaporation of organic materials or metals.

Another high vacuum chamber of capacity up to 10^{-8}mbar was used for the evaporation of Fullerene (C_{60}) and Buthocuproine (BCP) layers and the deposition of Aluminum contacts in order to finalize organic solar cell fabrication. In contrast with the previous system, this one has the advantage of being equipped with multiple Knudsen cells and the ability to process four (4) samples at one time. Increased substrate temperature is also in this case an option. Besides, as shown in **Figure** 5.4 and **Figure** 5.5, this chamber is connected with a sealed "Glove Box", so that the vacuum never falls under 10^{-6}, even when the samples are transported. Two different pumps are operating in this system: one stays always in use pumping constantly up to 10^{-3} mbar, while the other, more powerful one (turbo pump), is operated when high vacuum must be reached for the evaporation of materials under "clean" conditions. The existence of a glove box is really crucial, when it comes up to film and device storage and protection from contamination of the atmosphere. Apart from this, inside the glove box appropriate "packaging" of an organic solar cell is possible, that is, an organic solar cell can be attached to a small sealed box and can be safely

removed and transported into the atmosphere in order to be measured for electrical performance. A so called “manipulator” enables transfer of samples between the vacuum chamber and the glove box as shown in **Figure 5.6**. Through, the challenging usage of manipulator, inside the vacuum chamber, it is possible and desirable to rotate the samples during evaporation in order to achieve homogeneous layers.

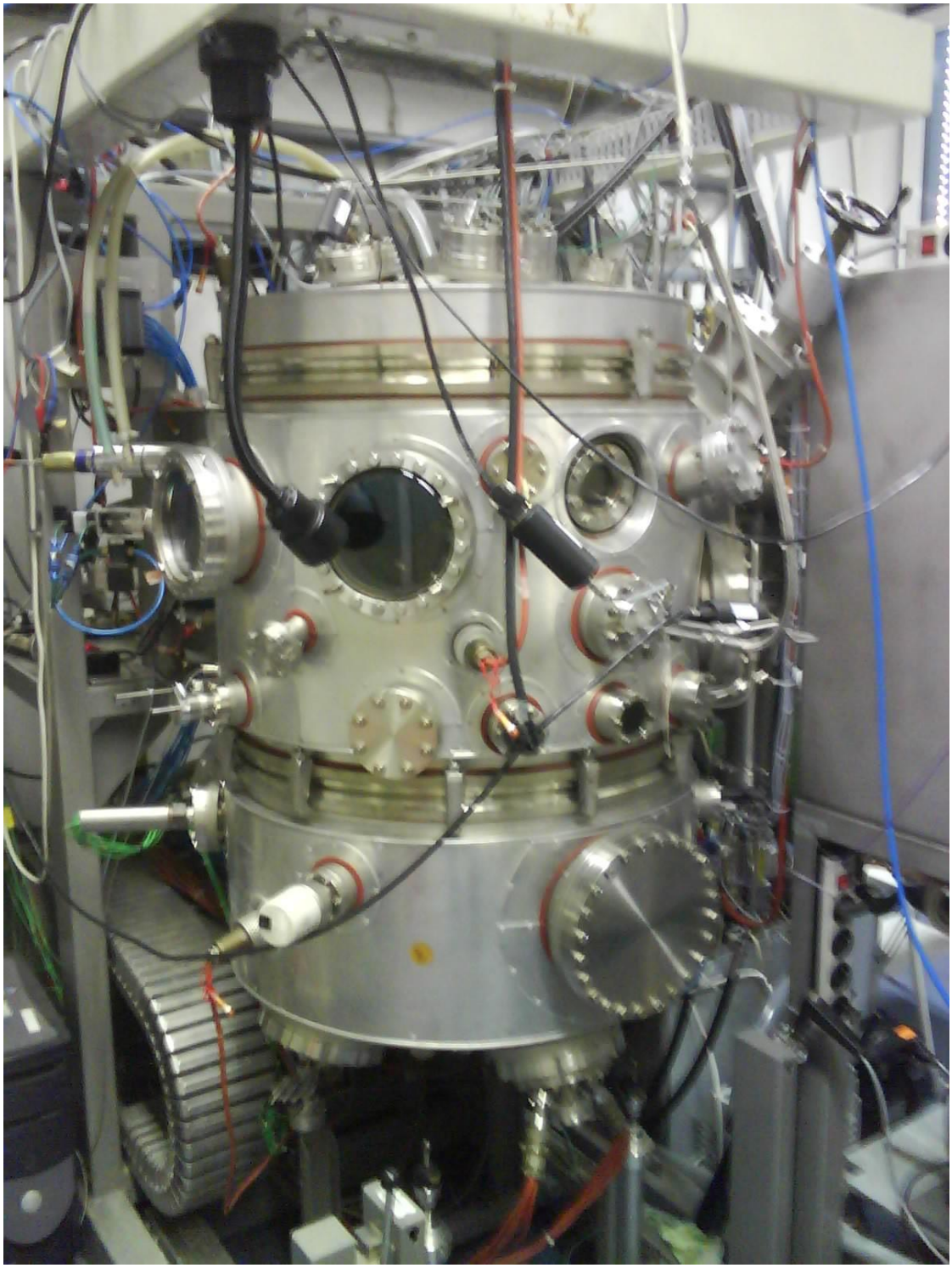

Figure 5.4 UHV chamber

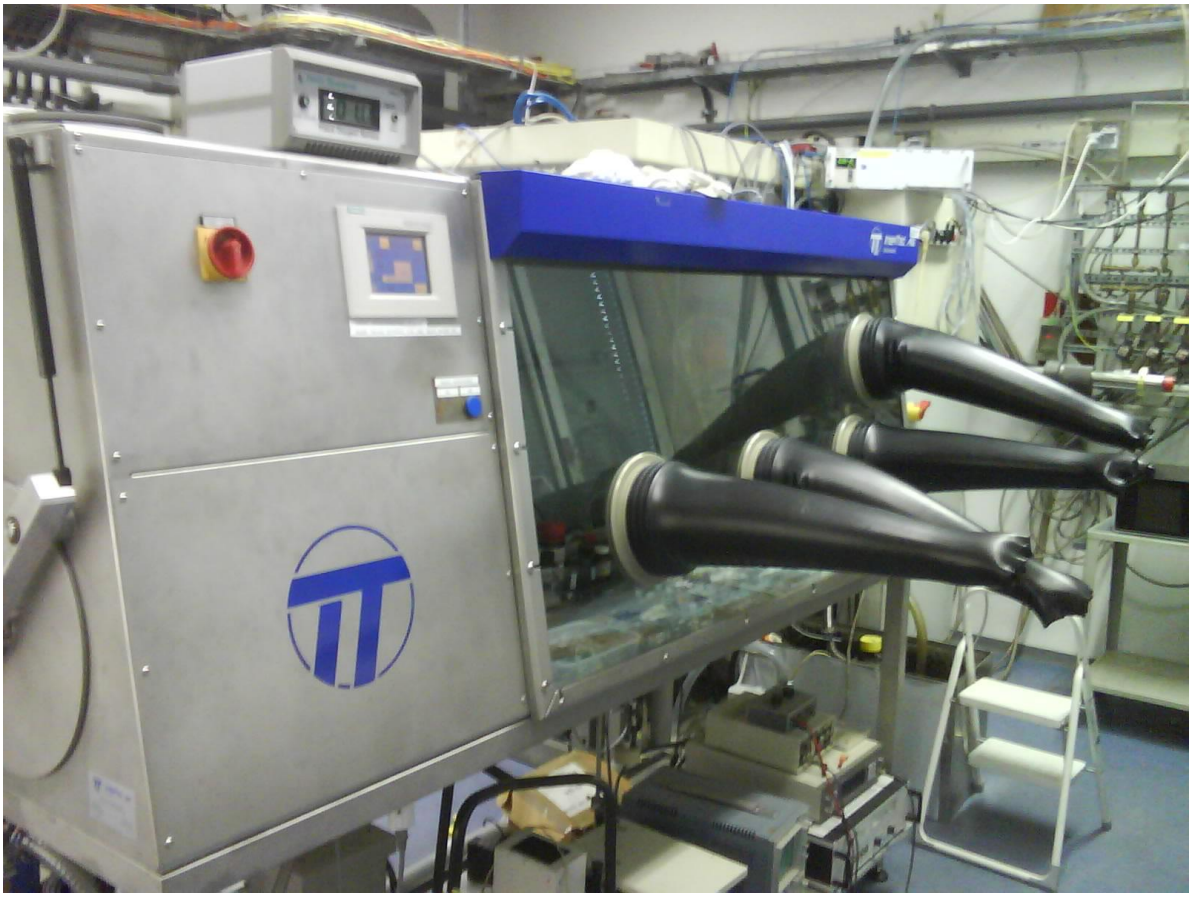

Figure 5.5 Atmosphere secured "Glove Box"

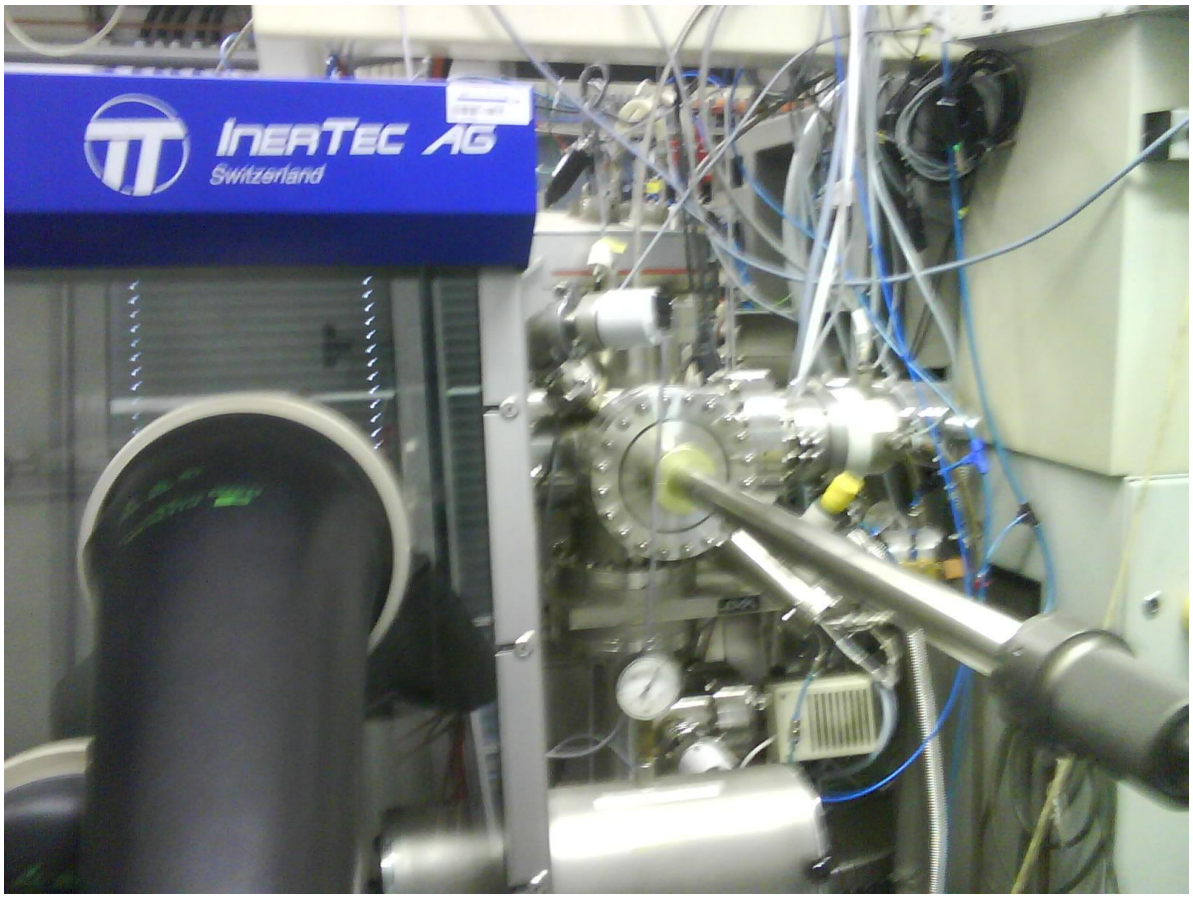

Figure 5.6 Chamber and Glove Box (the manipulator that enables sample transfer is visible).

5.2 UHV- Scanning Tunneling Microscope (TUB)

In this section, the Scanning Tunneling Microscope experimental setup will be presented. It is operated under UHV conditions at the **Institute of Solid State Physics of Technische Universität Berlin (TUB).**

Experiments were carried out at the Laboratory Facilities of the **Experimental Nanophysics and Photonics Group under the Direction of Prof. Dr. M. Kneissl and the Assistance of Dr. P. Vogt.**

The main component of the experimental set-up is an ultra-high vacuum (UHV) chamber operated at 10^{-10}-10^{-11} mbar for organic material evaporation, surface, and interface studies. Principally, the UHV chamber is equipped with accessories common to most in-vacuum growth facilities (three stage pump system, substrate holder with heater, manipulator, crucibles, characterization diagnostics, transporter, etc.). A unique characteristic of the substrate heater is the very high temperature level it can reach making possible inorganic substrate surface-reconstruction and epitaxial film growth in accordance with the atomic arrangement of the reconstructed surface. Low-energy electron diffraction (LEED) is applied as standard characterization diagnostic of surface-reconstructions. The aforementioned parts are shown in **Figures 5.7 and 5.8** respectively. As it is clearly seen in **Figure 5.7**, the system is equipped with several manipulators that can also move the sample holder (with the sample attached to it) to neighboring, from one another separated chambers. Ulterior motive is the placement of sample into the Scanning Tunneling Microscope, which is depicted in **Figure 5.9,** and there, images in atomic and molecular scale can be obtained.

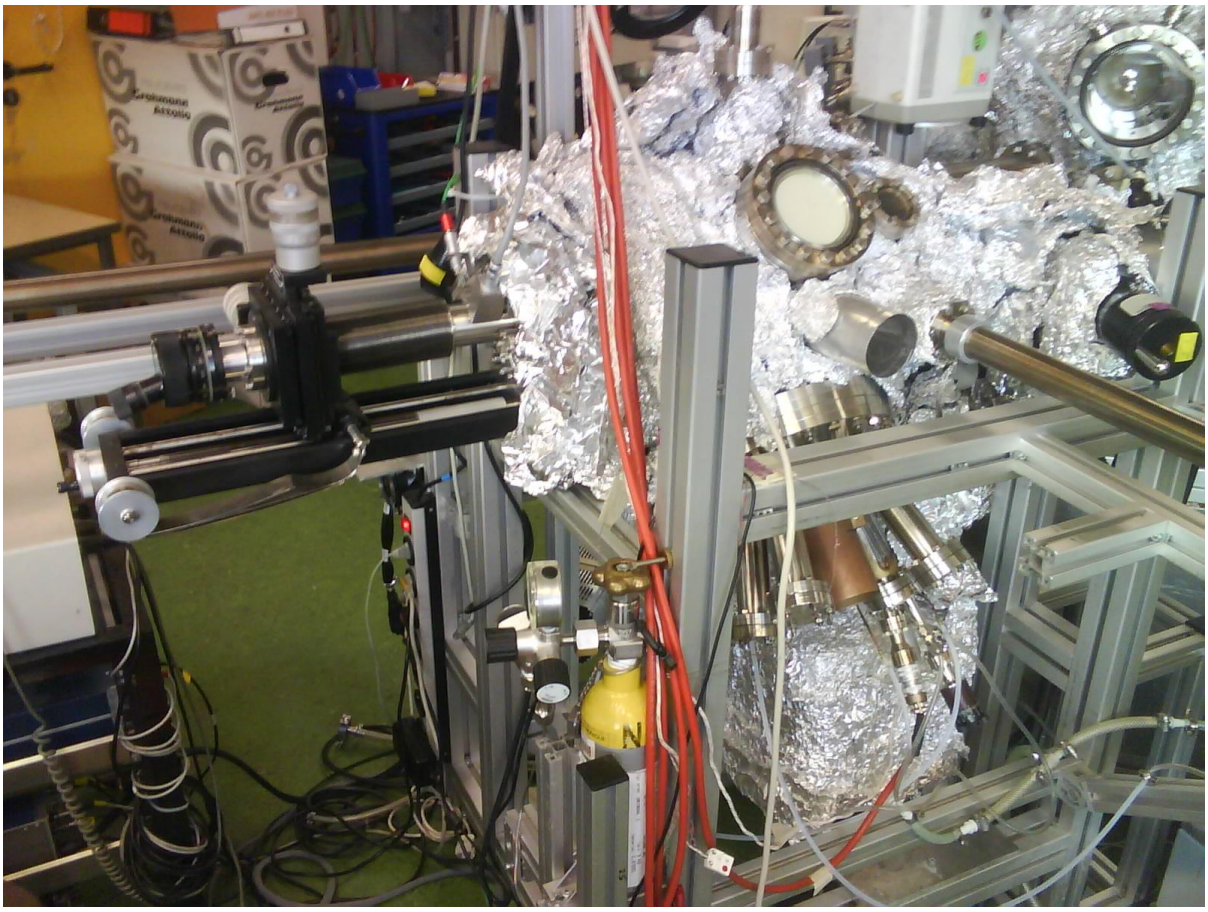

Figure 5.7 Deposition and surface reconstruction chamber.

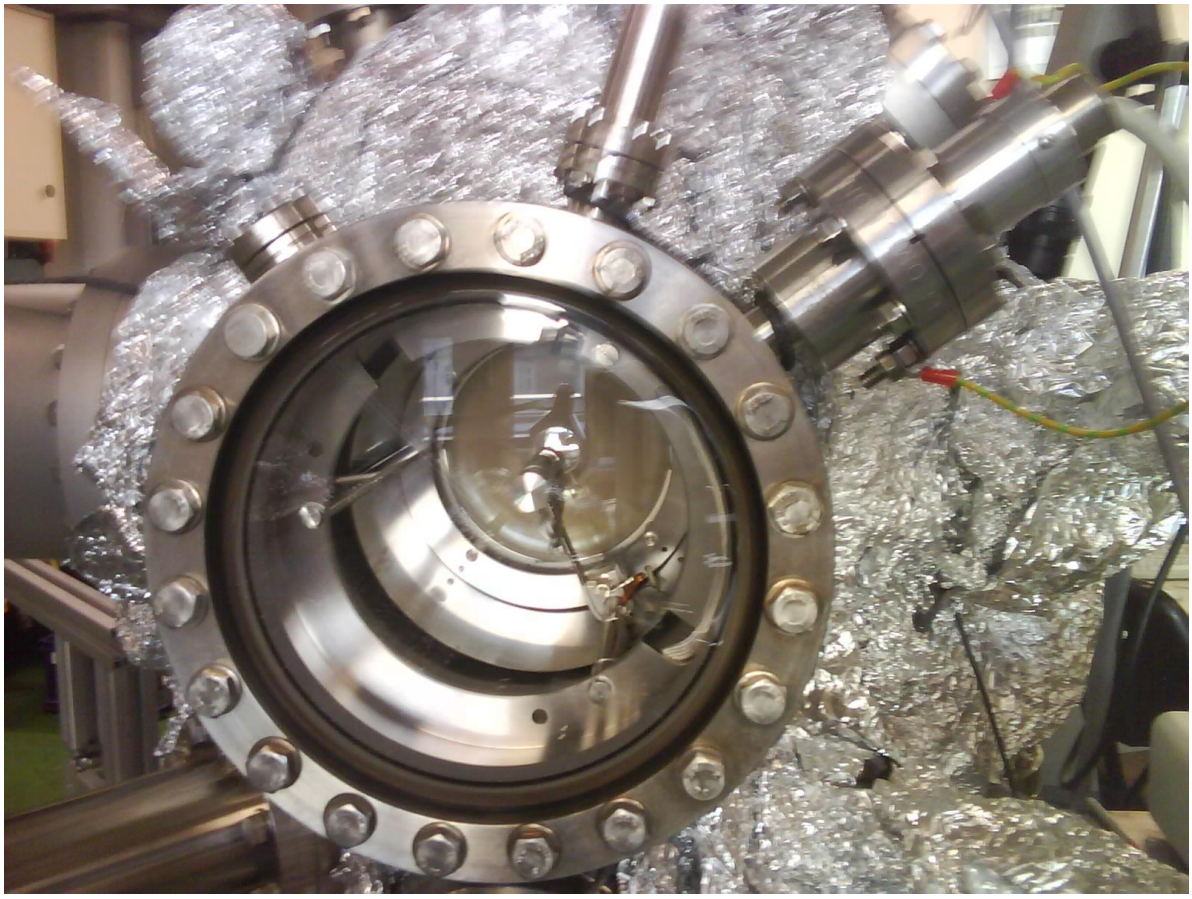

Figure 5.8 Part of the setup where LEED technique is applied.

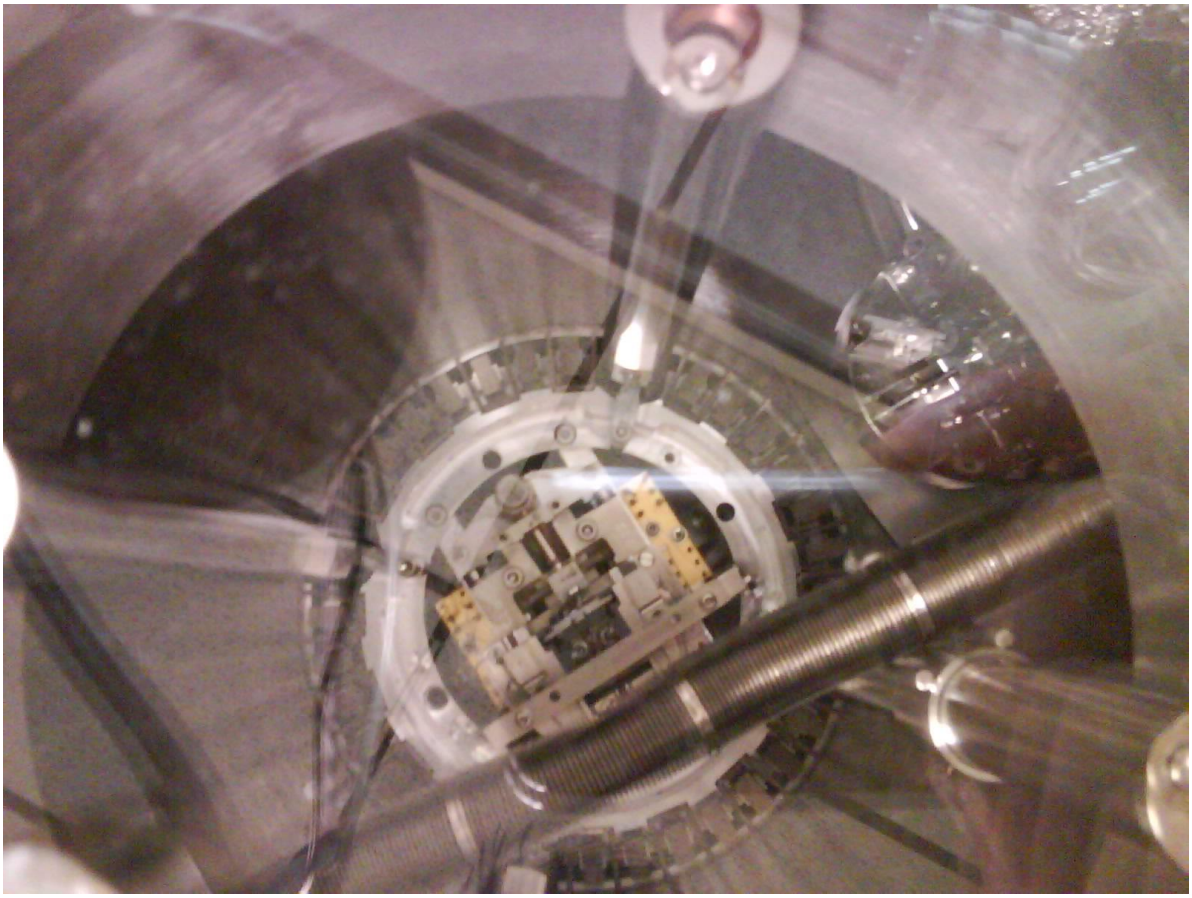

Figure 5.9 The Scanning tunnelling microscope. (STM)

5.3 Atomic Force Microscope (MPIG)

AFM measurements were performed **at the Department of Interfaces of the Max Planck Institute in Golm (MPIG)**, under the Direction of **Dr. H. Riegler** and with the valuable help of **Phd candidate F. Ghani**

A Veeco atomic force microscope was used as shown in **Figure 5.10.** In principle, AFM technique is much easier than STM, is performed in the atmosphere and thus is much faster. Once the sample is placed into the sample holder everything is controlled through a computer and structure and morphology of thin films can be revealed.

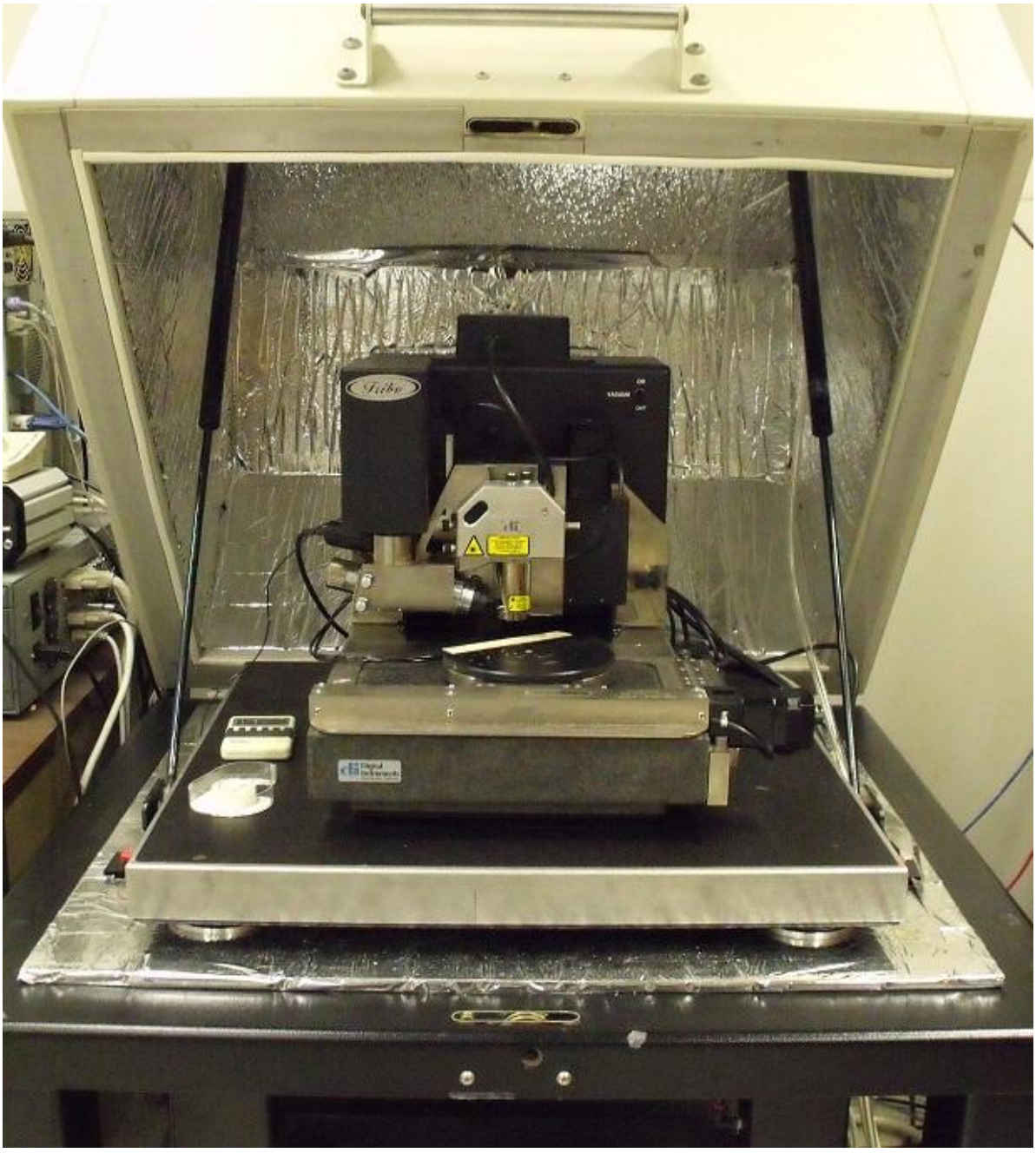

Figure 5.10 Atomic Force Microscope (AFM)

5.4 Optical systems (NTUA)

In this section, the experimental setup for **Optical Characterization via Modulation Spectroscopy (PR/ER)**, located at the **National Technical University of Athens (NTUA)**, is presented. **Assistant Professor Dr. D. Papadimitriou, Supervisor of the present Diploma-thesis, is Head of the Laboratory for Growth and Characterization of Advanced Materials and Devices, in particular, Materials and Devices for Photovoltaic Technology Applications, and Responsible for the Laboratory-Facilities of Modulation Spectroscopy and Spectroscopic Ellipsometry.**

As described in chapter 4.2.1 extensively, the modulation spectrometer consists of a self-built, modular experimental set-up, for modulated reflectance (PR/ER) and luminescence (PL/EL) measurements, equipped with Xe- and tungsten-halogen spectral-lamps, Ar^+- and Kr^+-lasers, two single-grating monochromators, Si- and InGaAs-diode detectors. The source light is analyzed by the first monochromator, directed onto the sample by several mirrors and focusing lenses, collected from the sample, filtered by a second monochromator, and detected by highly sensitive semiconductor diode detector using lock-in amplification techniques. In **Figure 5.10** the aforementioned parts (spectral-lamps, first monochromator, lasers, and beam-chopper) set in the path of the incident light are depicted.

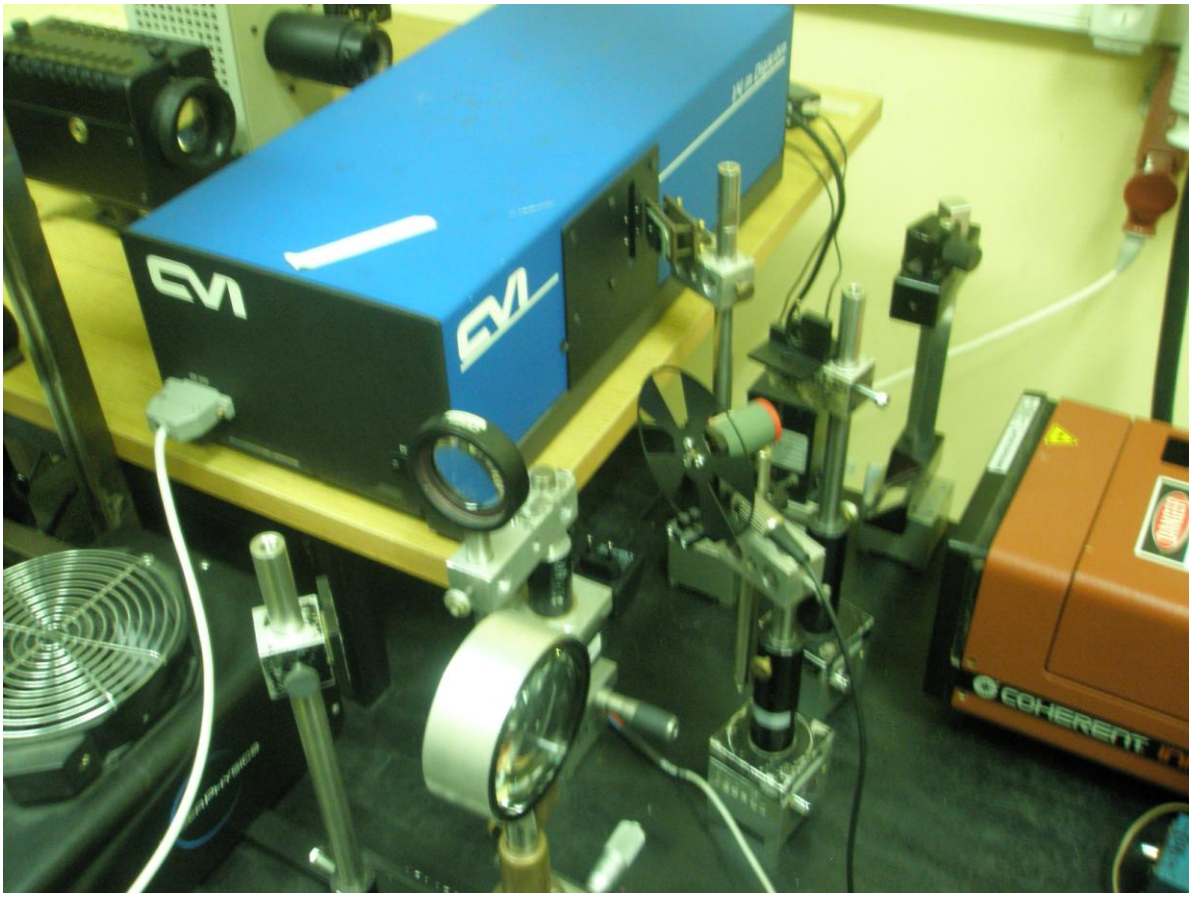

Figure 5.10 Halogen lamp, monochromator, focuses lenses and sample holder.

Figure 5.11 includes parts (spectral-lamps, lasers, first and second monochromator, detector at the exit-slit of the 2nd monochromator) set in the paths of both, the incident and reflected light, and also a close-cycle He-cryostat for the performance of low temperature measurements. The spectrometer is controlled by a computer as shown in **Figure 5.12**. The Lock-In unit along with the pulsed generator used for electrical modulation of the sample are also visible.

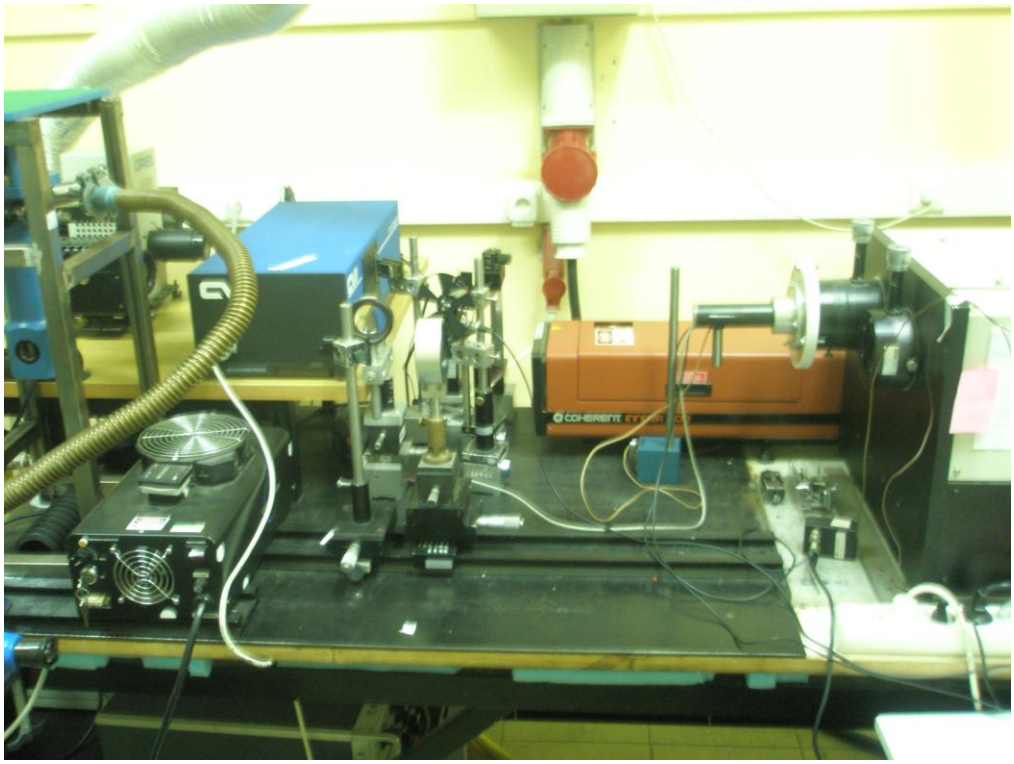

Figure 5.11 Detector and spectrometer on the right.

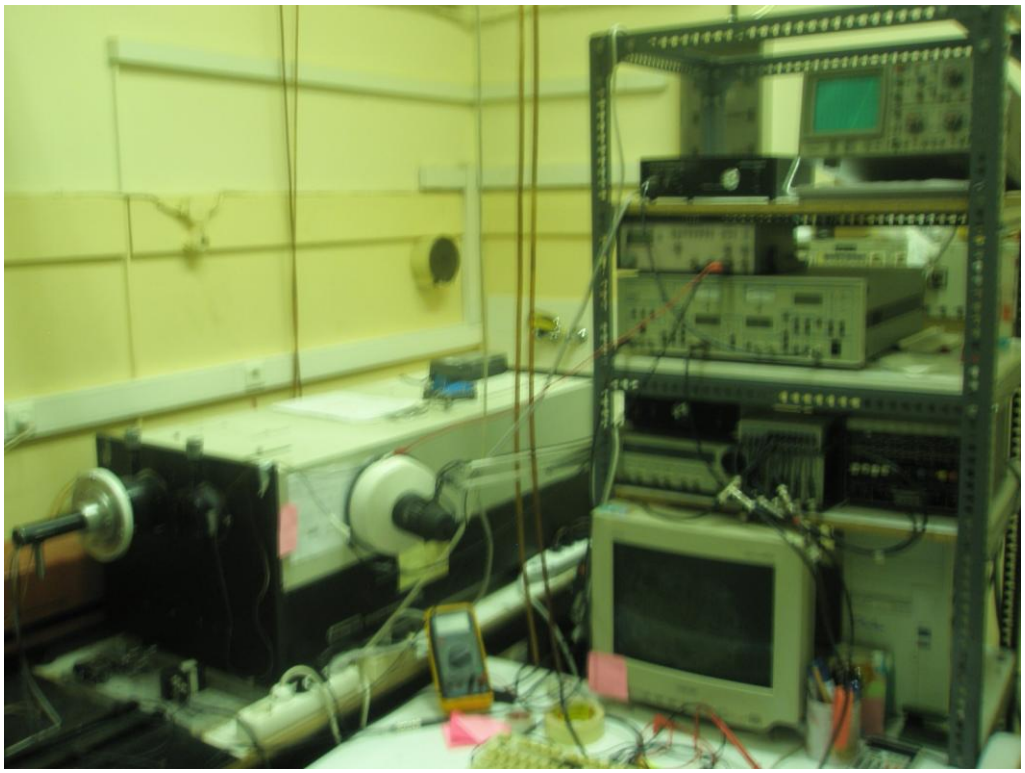

Figure 5.12 Spectrometer, computer and Lock-in unit.

Chapter 6 a-6T/C_{60} Organic Solar Cells (OSCs)

6.1 Substrate preparation

Deposition of organic layers requires a specific procedure of substrate preparation. Substrates should be completely clean of contamination, so that impurities affecting thin film structure and thus device performance can be avoided. Four different types of substrates have been used: Silicon dioxide wafers (SiO_2), float glass, Indium Tin Oxide (ITO) sputtered glass substrates for thin film growth (with the aim to optically and structurally characterize the grown samples), and Indium Tin Oxide (ITO) sputtered on glass for organic solar cell fabrication. With this last extra option, it becomes feasible to divide an organic solar cell into two electrically separated sub-cells suitable for comparative studies of material homogeneity, contact, and efficiency as will be explained later on, in section 6.3. The ITO film, coated on glass, had a thickness of 310 nm, and sheet resistance of about 7Ohm.

Substrates were consecutively cleaned with acetone, ethanol, and de-ionized water, in ultrasonic bath, for 20min each. Afterwards, the substrates were immediately dried in a nitrogen stream. Cleaned substrates were then placed inside the HV chamber for deposition or otherwise were kept inside an atmosphere-free glove-box to avoid contamination.

6.2 Organic thin film deposition

Once the cleaned substrates were placed inside the HV chamber, shown in **Figure 5.1**, and the vacuum has reached maximum affordable values, the deposition of an organic thin film could start. Primarily, ***thick a-sexithiophene layers*** were created by thermal evaporation under $5x10^{-6}$ mbar vacuum on SiO_2 wafers and float glass, so that the structure and morphology is investigated by atomic force microscopy (AFM) measurements. The temperature of the Knudsen cell containing the solid organic material has reached 250 ^{o}C before the deposition started. Consequently, a deposition rate of 0.3-0.4 Å/sec was achieved and the layers were formed after a few minutes.

Next, thin a-sexithiophene layers were deposited on ITO coated glass substrates in order to be optically characterized with UV-VIS spectroscopy. Deposition parameters were similar, only the film thickness was limited to **30nm**. For comparison, a layer of **30nm** a-sexithiophene was deposited on a heated ITO coated glass substrate at 90 ^{o}C substrate temperature. Two of the **30nm a-sexithiophene** samples were placed inside the HV

chamber, shown in **Figure 5.4,** for further deposition of organic layers. In particular, on both samples, a **30nm Fullerene C_{60}** film was thermally evaporated, under $3x10^{-7}$ mbar vacuum, at a rate of 0.3 Å/sec, from a source heated at temperature of 468 ^{o}C. Following that, only one of the samples was exposed to further processing by leaving the sample holder shutter open. In this way, **10nm** of **Bathocuproine (BCP) exciton blocking layer** could be deposited with a rate R=0.3 Å/sec at T=200 ^{o}C source temperature under the same vacuum $3x10^{-7}$ mbar. Tables 6.1 and 6.2 include an overview of all samples produced at this stage along with the deposition parameters and the investigation purposes.

Table 6.1

Sample	Substrate	Substrate Temperature	Organic layers	Purpose
1	SiO_2	RT	a-6T	Surface analysis
2	Float Glass	RT	a-6T	Surface analysis
3	ITO Coated Glass	RT	a-6T	Optical characterization
4	ITO Coated Glass	$90^{o}C$	a-6T	Optical characterization
5	ITO Coated Glass	RT	a-6T C_{60}	Optical characterization
6	ITO Coated Glass	RT	a-6T C_{60} BCP	Optical characterization

Table 6.2

Organic layer	Thickness nm	Deposition Rate Å /sec	D.Temperature ^oC	Vacuum mbar
a-6T	30	0.3-0.4	250	$5x10^{-6}$
C_{60}	30	0.3	468	$3x10^{-7}$
BCP	10	0.3	200	$3x10^{-7}$

6.2.1 a-6T film surface analysis

As mentioned previously, thick a-6T films deposited on SiO_2 and float glass substrates, respectively, were used for surface analysis by atomic force microscopy (AFM). In **Figure 6.1** and **6.2,** a 3-D AFM image of thick films on both substrates is demonstrated. As it can be seen, regardless of the substrate that has been used, the surface morphology is similar. It exhibits a **rod-like growth of the a-6T layer**. This characteristic is, in principle, desirable for organic electronic applications, because it assists charge carrier transport between different layers. Nevertheless, the growth of thinner and longer rods would be ideal. This could be probably achieved by varying the deposition parameters, such as deposition temperature and rate along with substrate temperature. Films may be also subjected to subsequent annealing (post deposition annealing). **Figures 6.3** and **6.4** show the topography of the particular films as obtained with the atomic force microscope. Light spots on top of the films can be attributed to contamination of the film surface during transport and measurement procedure.

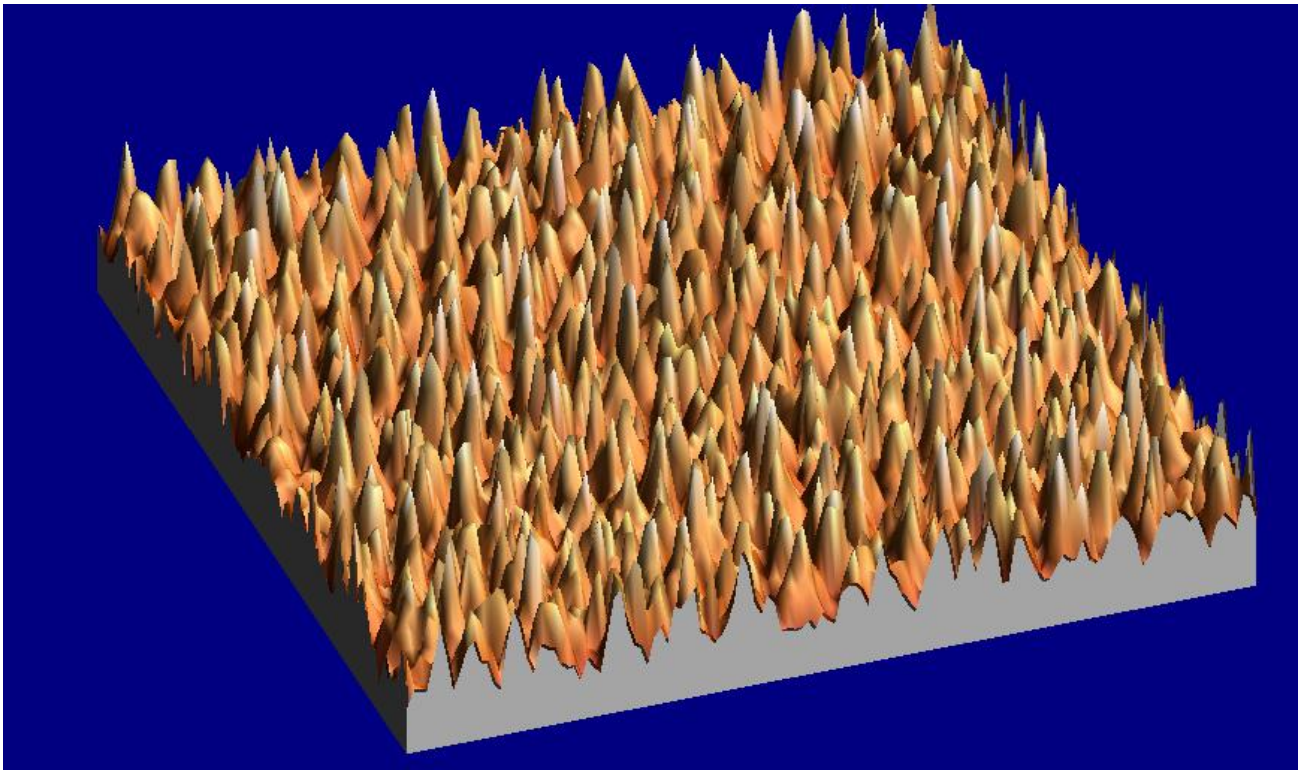

Figure 6.1 3-D AFM image of a thick a-6T layer on SiO_2

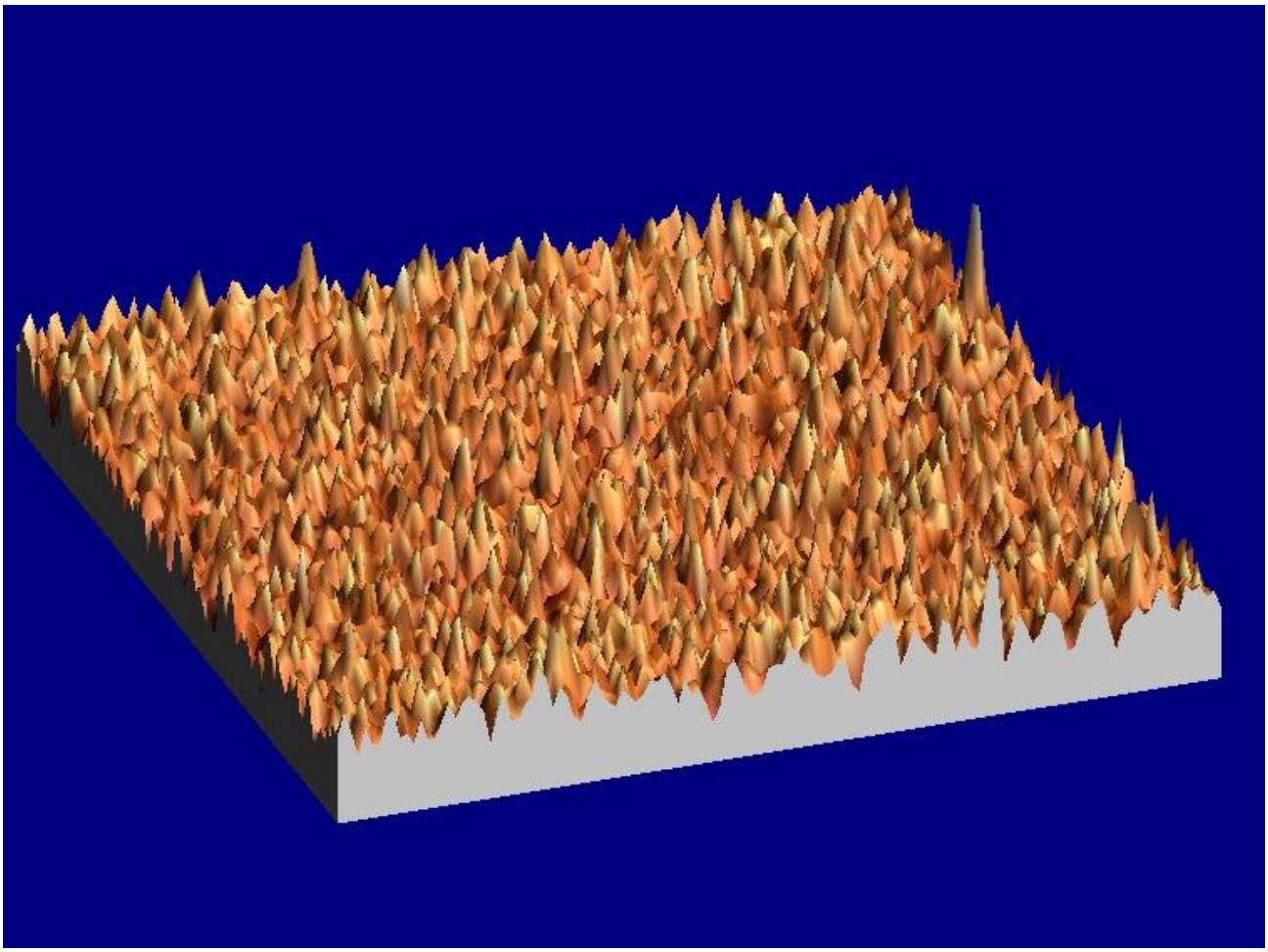

Figure 6.2 3-D AFM image of a thick a-6T layer on float glass.

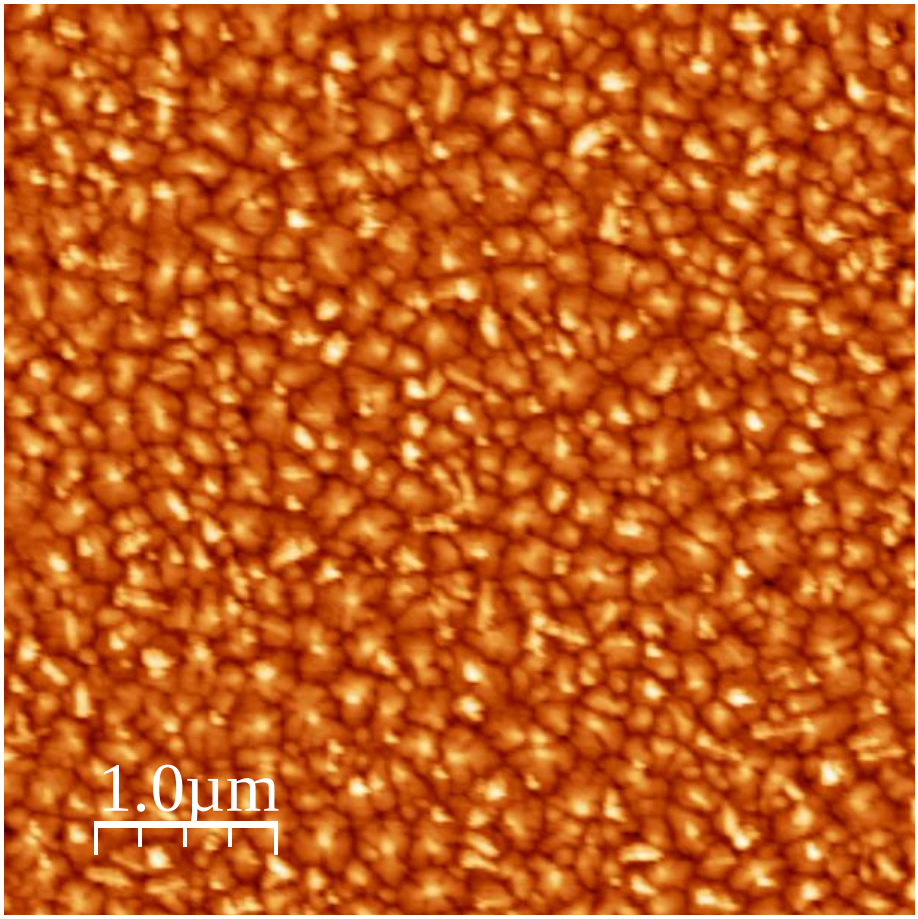

Figure 6.3 Topography image of a a-6T thick layer on SiO_2.

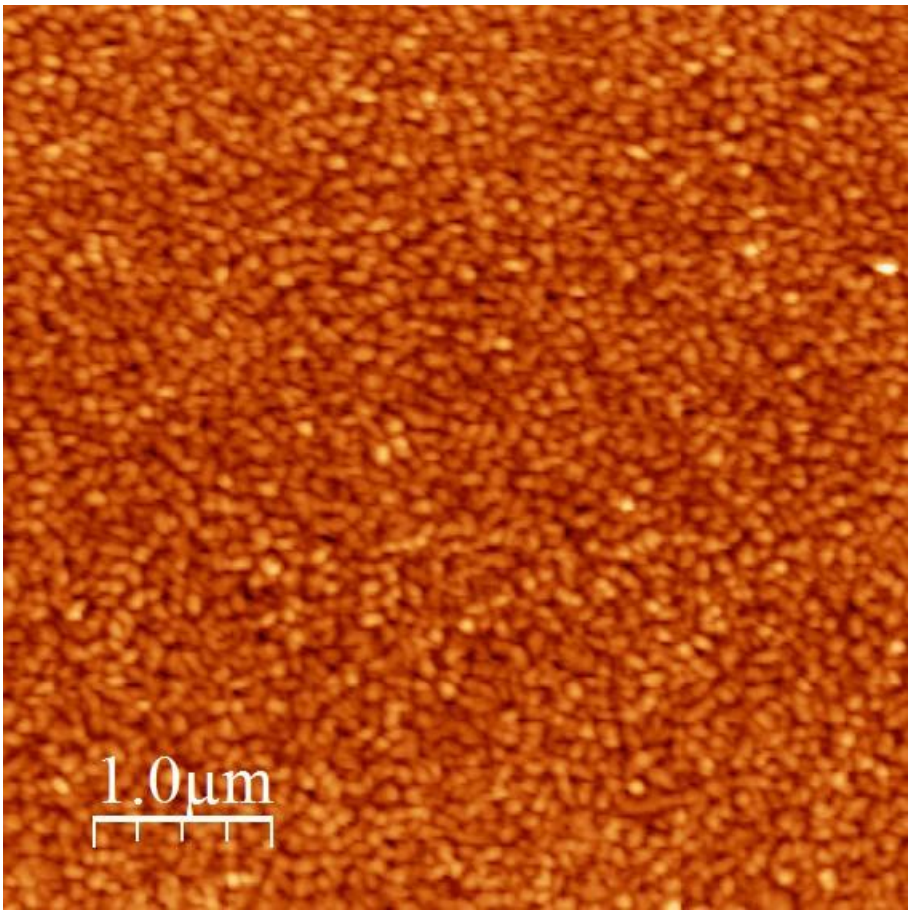

Figure 6.4 Topography image of a thick a-6T layer on float glass.

AFM software provides a surface roughness analysis tool. This tool is not capable of calculating film thickness. Nevertheless, it gives a clue of the roughness of the very last layers of the film, as shown in **Figures** 6.5 and 6.6**,** for each sample, respectively. Supplementary **Figures** 6.7 and 6.8 present the histograms and give an estimation of the average film height.

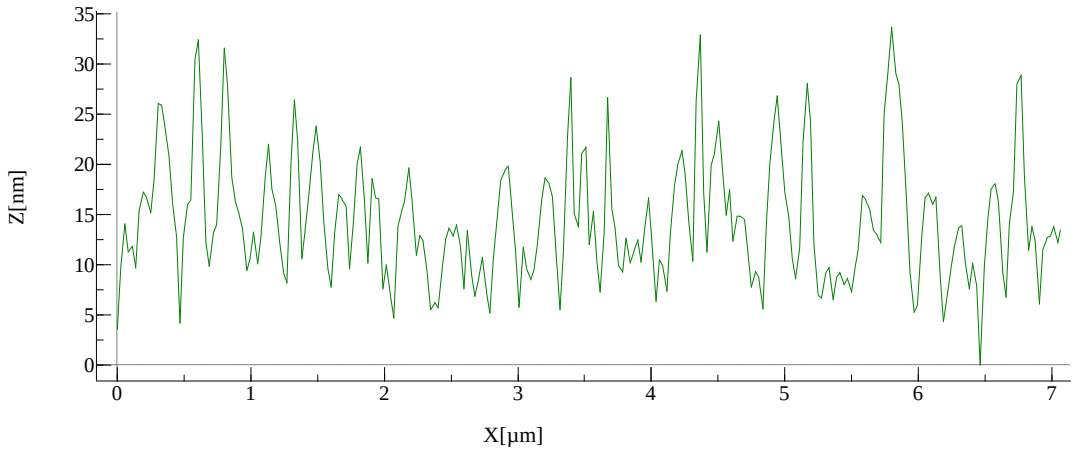

Figure 6.5 Surface roughness analysis of a-6T film on SiO_2.

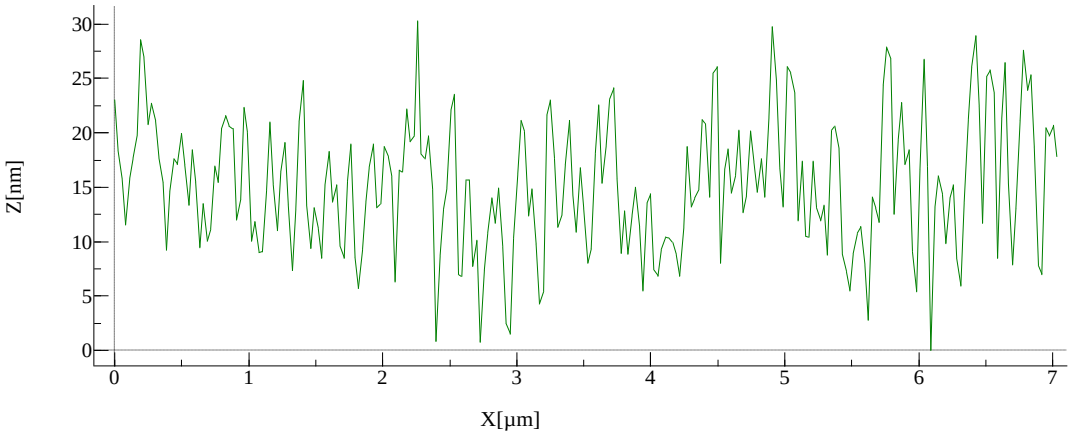

Figure 6.6 Surface roughness analysis of a-6T film on float glass.

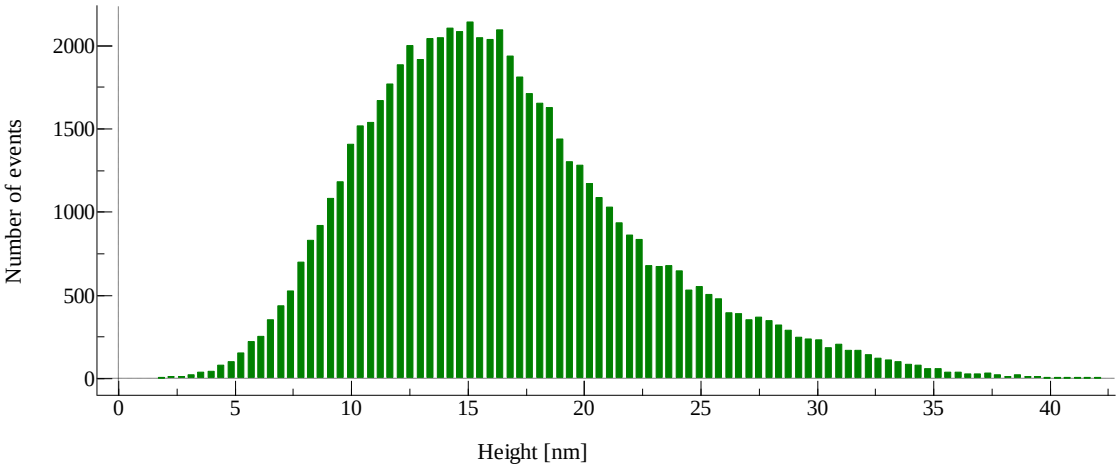

Figure 6.7 Histogram representing average film height on SiO_2.

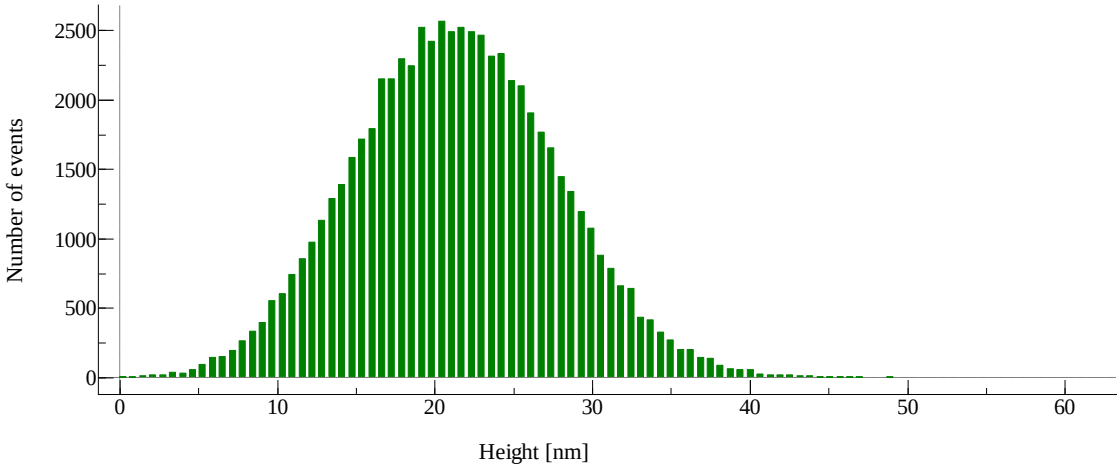

Figure 6.8 Histogram representing average film height on float glass.

6.2.2 a-6T thin film optical properties

As mentioned previously, an individual series of samples have been produced for optical measurements aiming to the determination of the optical absorption of thin films by UV-VIS Spectroscopy. Different samples were used in order to specify the absorbance of the layer stack at individual stages during organic solar cells fabrication, as has been explained in Chapter 3 extensively and will be explained furthermore later on. **Figure 6.9** presents the absorption spectra of the aforementioned samples along with the spectrum of an a-6T film deposited on ITO substrate heated at 90°C. The latter exhibits absorbance lower than the equivalent one deposited at room temperature (RT). Thus, heating may interrupt the oriented rod-like growth that is assumed to favor, in particular, the optical properties of the deposited films. Concerning the other samples, an increase in absorption can be easily identified as more layers are deposited. One negative feature that strongly affects the total absorbance of the stack is that a-6T film as well as C_{60} film absorb mainly within the same spectral range from 350 to 600 nm (see also **Figure 2.9**)

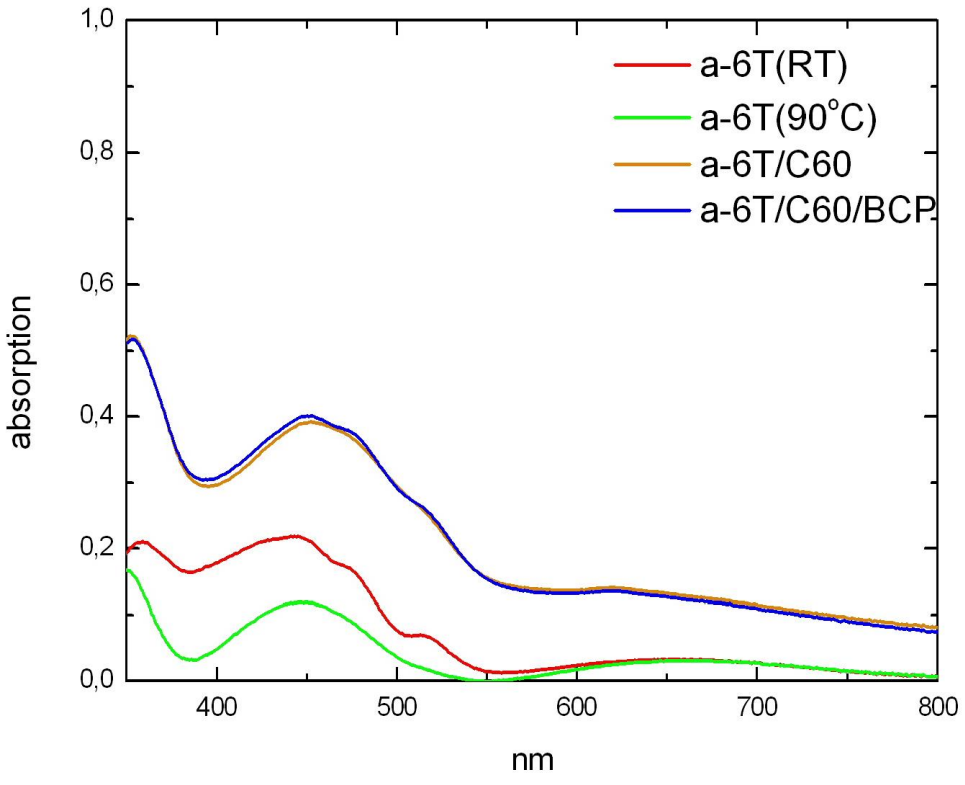

Figure 6.9 Absorption spectra of a-6T at RT (solid red) and at 90°C (solid green), a-6T/C_{60} bi-layer (solid pink) and a-6T/C_{60}/BCP layer stack (solid blue)

6.3. a-6T/C_{60} bi-layer heterojunction based OSCs

In this section, the organic solar cells fabricated within the frame of this Diploma-thesis are presented as completed devices. First, the device architecture is presented followed by electrical and optical measurements that determine the performance of a device.

6.3.1 Solar cell architecture

Similar solar cell architecture has been used for all solar cells that were fabricated. In some cases a different film thickness and/or chemical treatment of the substrate was the distinct parameter. In **Figures** 6.10 and 6.11**,** a schematic drawing and an actual photo of an organic solar cell is shown. With similar deposition conditions used in thin film growth described previously, 30-35nm thin films of a-6T acting as donor material were thermally evaporated on ITO sputtered glass substrates which were also structured in a way that two separated front electrodes can be adapted. This leads to two distinct OSCs enabling, in each case, two different electrical measurements from the same active layer. Following 30nm C_{60} as an acceptor material and 10nm BCP as buffer layer and exciton blocker completed the organic layer stack. At the end of the procedure, 100nm aluminum contacts completed the device.

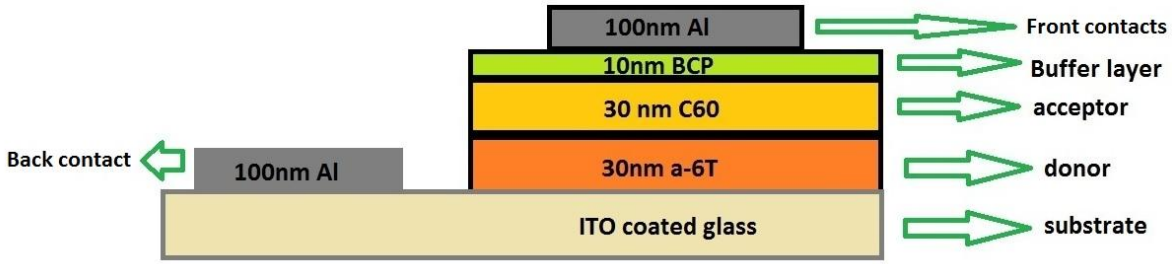

Figure 6.10 Schematic drawing of the organic solar cell fabricated.

Figure 6.11 Photo of the developed organic solar cells (OSCs).

6.3.2 Electrical characterization (I-V curves)

Properly functioning organic solar cells were developed with I-V characteristic curves similar to the theoretically expected and shown in **Figure 3.11 (chapter 3.3)**. The cells were featured by one or more unique characteristics: In the first cell structure (***OSC1***), **30nm of a-6T** were used as a donor material. The layer stack consisted of **30nm a-6T, 30nm C_{60}, 10nm BCP, and 100nm Al contacts**. Efficiencies of η_{1a}***=0.7%*** and η_{1b}***=0.67%*** were measured on the two equivalent electron collectors on top of the cell**.** It is reminded, that, as we mentioned earlier, from one organic solar cell two different electrical measurements can be obtained by using the same organic active layer, the same back contact, but two distinct front contacts. In this way, efficiency fluctuations generated possibly by material inhomogeneities can be identified and handled. **Figures 6.12a** and **6.12b** show I-V curves and give the performance characteristics for ***OSC1***. I-Vs are characteristic of a relatively high shunt resistance indicating the existence of defects in form of carrier "traps" in the ITO substrate. The presence of defects is strongly related to the lack of a substrate passivation process which could reduce carrier trapping effects.

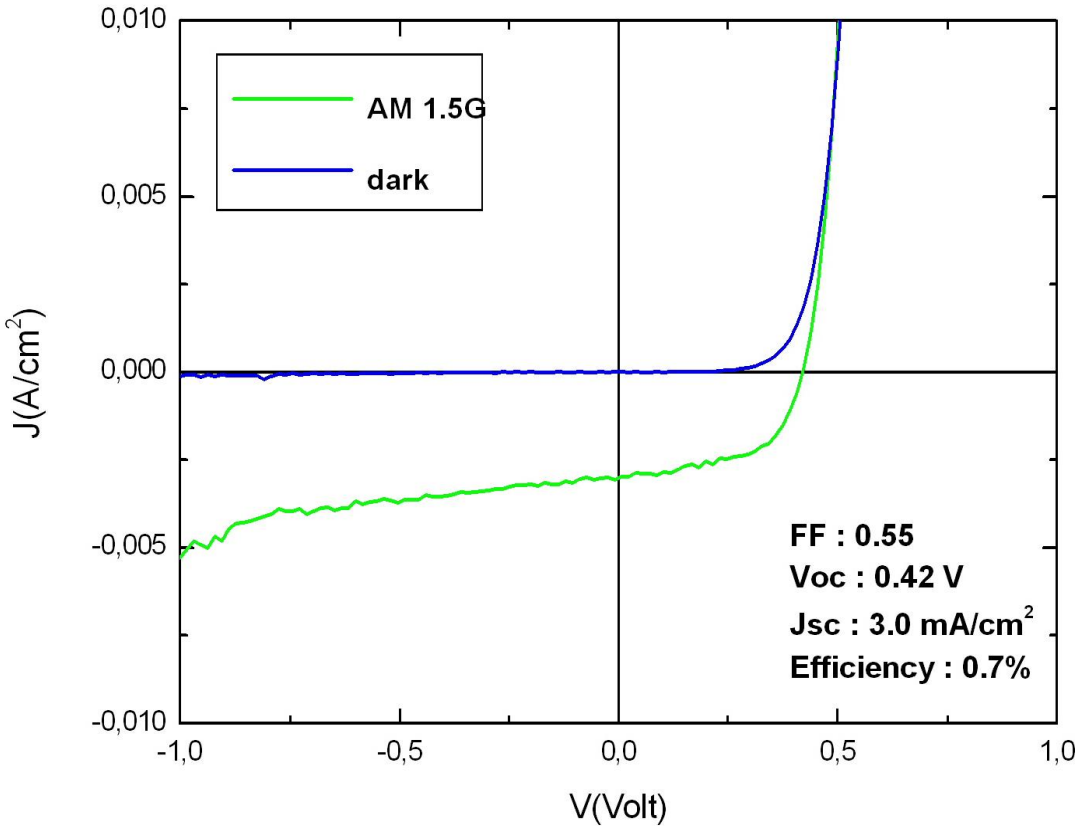

6.12 a)

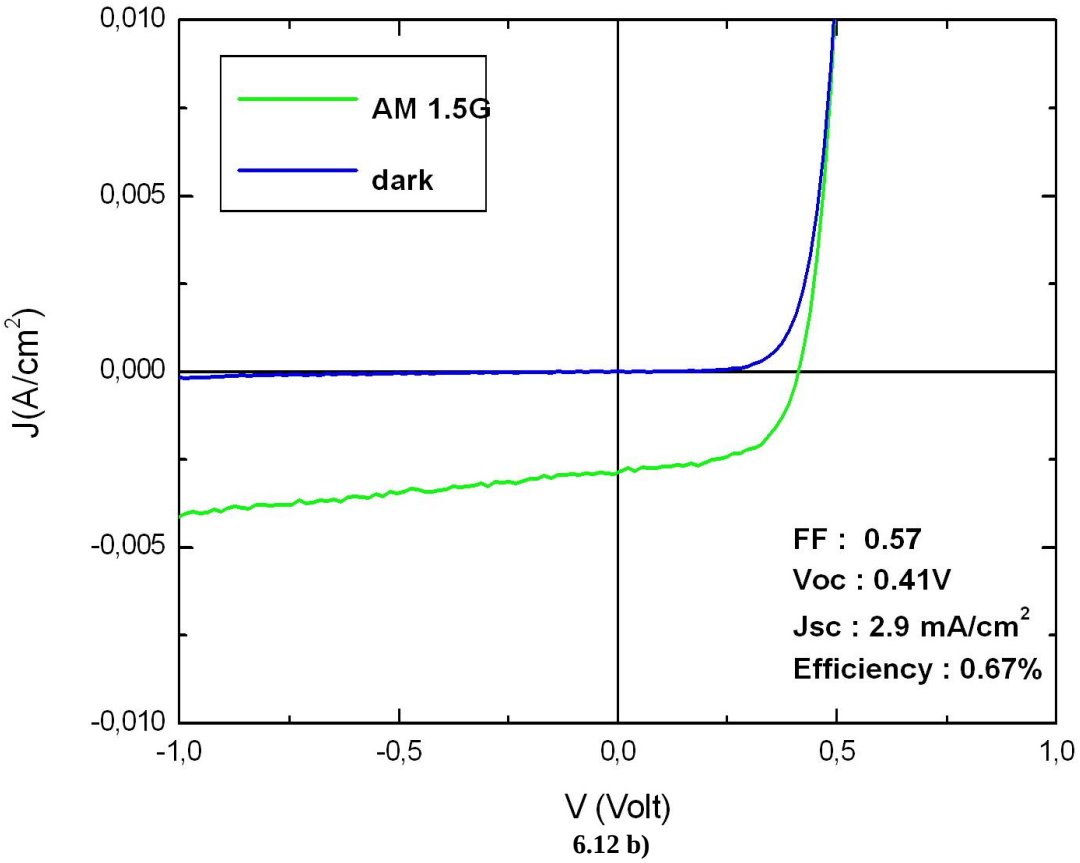

6.12 b)

Figure 6.12 a) and b) I-Vs of OSC1 measured at the two different Al-front contacts of the cell.

In the second cell structure (***OSC2***), passivation of the ITO substrate with ***phosphoric acid*** (***H_3PO_4***) has been applied before the deposition of organic layers. In particular, the ITO substrate was bathed into phosphoric acid for 20 minutes followed by de-ionized water cleaning and nitrogen stream drying and 10 minute annealing process at 120 ^{o}C in order to fully remove excess water left on the surface. Again, a **30nm a-6T** layer was used as donor material followed by **30nm C_{60}, 10nm BCP, and 100nm Al contacts**. ***Power conversion efficiency* (*PCE*) η_{2a}=0.7%** acquired on one of the two front contacts was comparable to that of ***OSC1***. Measurement from the second front contact has not been possible as a consequence of a short circuit at the specific front contact. In **Figure 6.13**, the I-V curve of the ***OSC2*** looks smoother that the previous one, although the high shunt resistance can still be acknowledged.

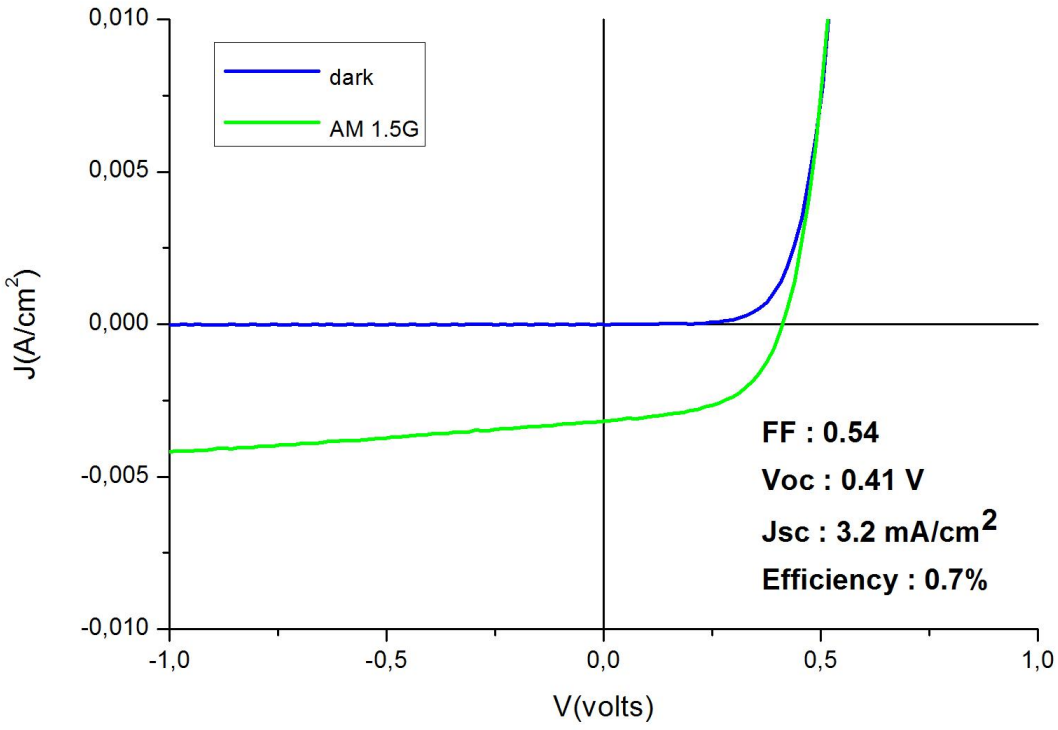

Figure 6.13 I-V curve of OSC2 processed on a chemically treated ITO substrate.

During fabrication of the third organic solar cell (***OSC3***), the ITO substrate was again chemically treated with phosphoric acid. Thus, the use of a slightly thicker (35nm) a-6T was the main difference to the previous case (***OSC2***). Measurement on one of the two front contacts showed an increase of ***PCE*** up to ***η_{3a}=0.76% (Figure 6.14a)***. Nevertheless,

measurement from the other front contact led to lower efficiency of η_{3b}=*0.66%* and an I-V curve that denotes dysfunction of the cell ***(Figure 6.14b).***

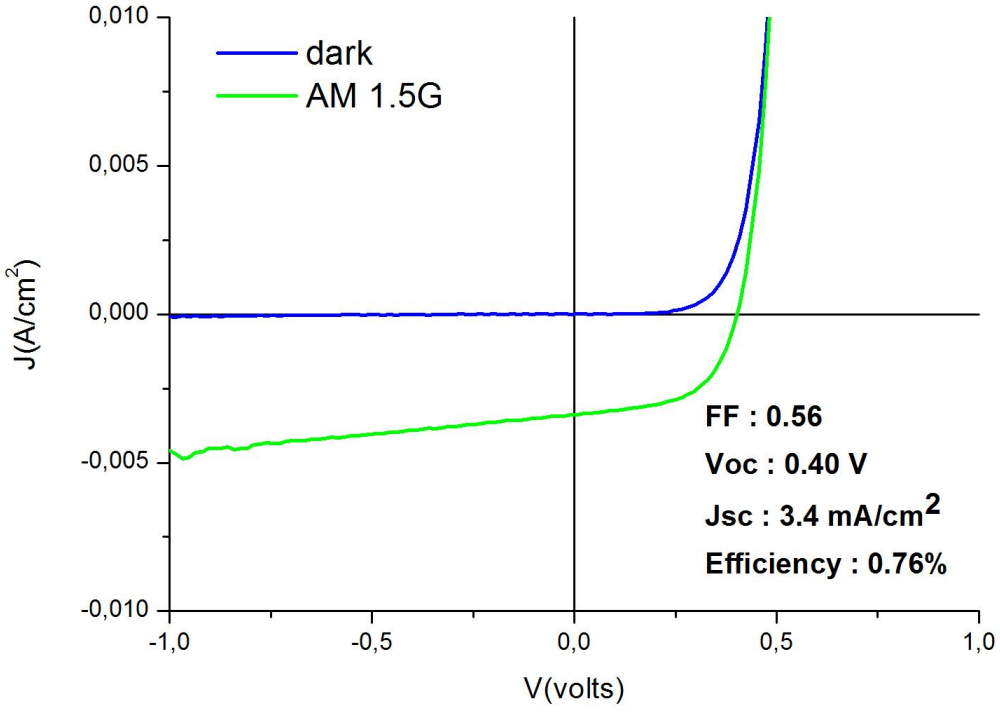

6.14 a)

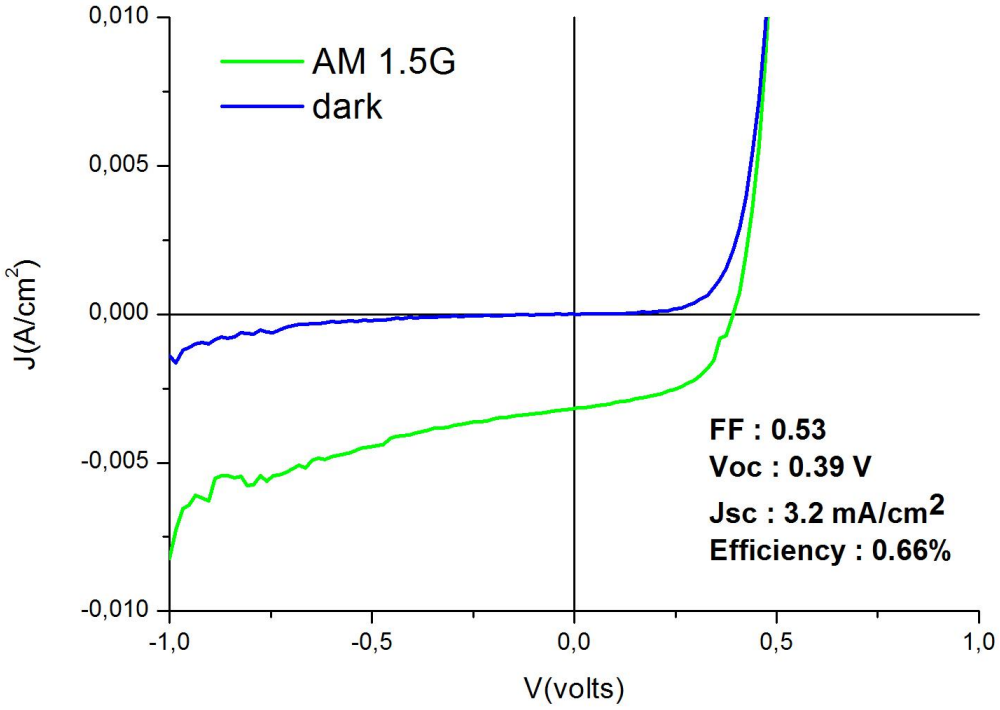

(6.14b)

Figure 6.14 a) and b) I-V curves of OSC3 measured at the two different front Al-contacts.

6.3 Optical characterization

At this point, a comparison between optical absorption of a complete organic solar cell and absorption at each separate stage of fabrication can be made. **Figure 6.15** is the same as **Figure 6.9** with the addition of the optical absorption curve of the third, most efficient organic solar cell (***OSC3)***. As can be seen, optical absorption of ***OSC3*** is lower than that of the last two stages of fabrication process. This is attributed to the reflection of incident light at the two front Al-contacts of the completed solar cell.

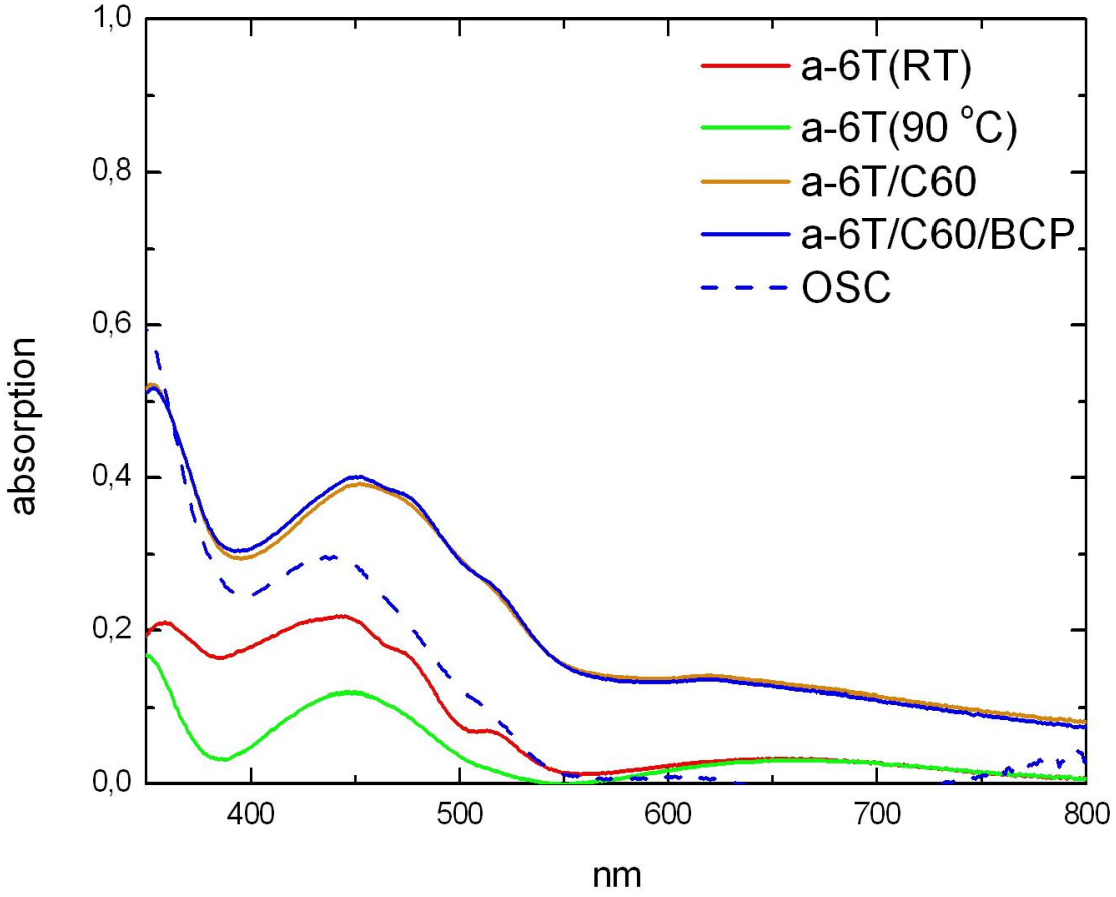

Figure 6.15 Absorption spectra of a-6T layer at RT (solid, red) and 90 °C (solid, green), a-6T/C60 bi-layer (solid, pink), a-6T/C60/BCP layer stack (solid, blue), and a-6T:C60 Organic Solar Cell (dashed, blue).

It is crucial to apply the basic operation principles of an organic solar cell, presented in **paragraphs 3.2** and **3.3**, at the a-6T/C_{60} heterojunction based cell developed and calculate the charge carrier transitions. **Figure 6.16** depicts the energy level diagram (HOMO-LUMO) of the organic materials constituting the a-6T/C_{60} OSC along with the work functions of ITO substrate and Al-contacts, as they were extracted from [5] and [40].

According to this energy level diagram absorption of the incident light leads to creation of an exciton (electron-hole pair). This exciton travels to the interface where it dissociates. The hole travels to the ITO substrate through the HOMO level of a-6T and the electron initially is transitioned to the LUMO level of C_{60} and afterwards connects to the Al electrode throughout the BCP layer. The BCP layer plays the role of buffer layer in this device facilitating charge transport. **HOMO-LUMO** transition inside a-6T layer is calculated to **2.2eV (563.5nm)** and **LUMO-LUMO** transition between a-6T and C_{60} is estimated to **1.4eV (885.5nm)**.

Optical characterization of the organic solar cells by Electroreflectance (ER) spectroscopy was attempted long time after their fabrication. The results resemble the optical transitions (HOMO-LUMO/2.2eV, LUMO-LUMO/1.4eV) expected for the organic constituents of the cell structures investigated in this Diploma-thesis, as demonstrated in **Figures** 6.16 and 6.17. However, electrical measurements revealed that the cell is no longer active, which suggests limited organic solar cell endurance despite material stability.

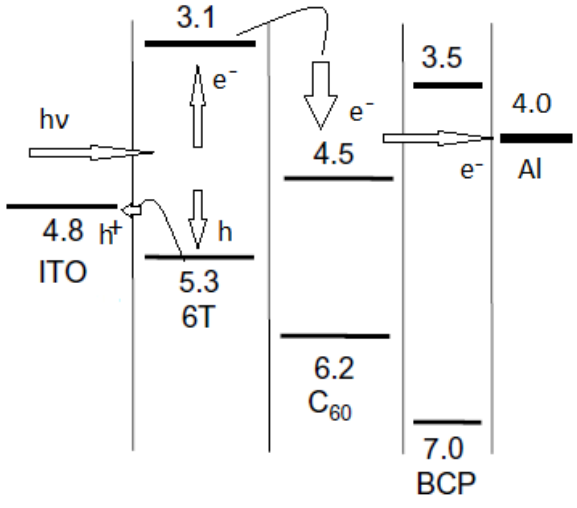

Figure 6.16 Energy level diagram of the a-6T/C_{60} OSC.

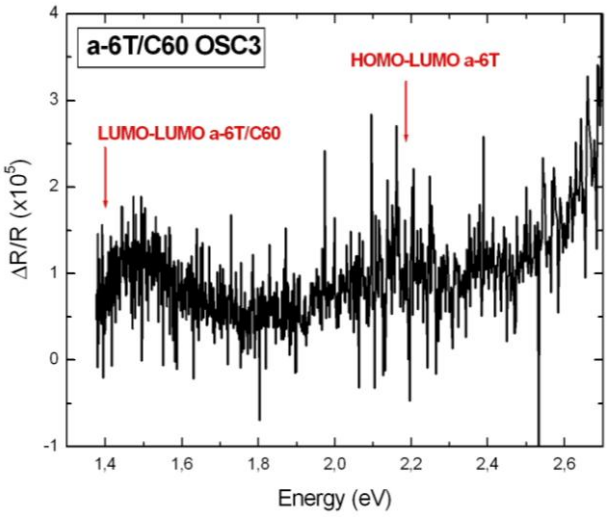

Figure 6.17 ER-spectrum of a-6T/C60 OSC.

Chapter 7 Molecular orientation on semiconductor surfaces

In this chapter, we present the investigation of molecular adsorption on inorganic semiconductor surfaces within the **Experimental Nanophysics and Photonics Group under the Direction of Prof. Dr. M. Kneissl and the Assistance of Dr. P. Vogt, at the Institute of Solid State Physics of Technische Universität Berlin (TUB)**. **Published research of Dr. T. Bruhn [36-37] and Phd candidate L. Riele [38] is used as reference.** The basic tools for this research are Scanning Tunneling Microscopy (STM), Scanning Tunneling Spectroscopy (STS) and Reflectance Anisotropy Spectroscopy (RAS). The experimental setup was described in Chapter 5.

Of great significance over the past few years is the investigation of fundamental parameters influence of molecular adsorption on semiconductor surfaces. Basic Research and Novel Applications in Electronic and Optoelectronic Devices, such as organic field-effect transistors (OFETs), organic light emitting diodes (OLEDs, displays), organic solar cells, and gas sensors are the apparent motivation of this investigation. Reflectance Anisotropy Spectroscopy (RAS) provides a non-destructive in-situ observation of the growth of ultra-thin molecular layers in sub-monolayer range. Scanning Tunneling Microscopy (STM) is used for imaging of the organic-inorganic interface and Scanning Tunneling Spectroscopy (STS) enables the electronic investigation of single molecules and molecular films.

Reflectance Anisotropy Spectroscopy is sensitive to anisotropic optical surface transitions. Moreover, it is extremely sensitive for different kinds of surface modification, like the adsorption of organic molecules or adsorbates such as hydrogen. It can also monitor the time dependent behavior of adsorption processes. In recent years, the application of RAS was extended to molecular layers, because it was shown that intramolecular transitions can contribute to the RAS signal of anisotropically ordered molecular films. In this case, RAS is used as a tool for the preparation and in-situ characterization of molecular adlayers in sub-monolayer range. The goal is to identify molecular orientation within the layer. This is crucial in organic semiconductors such as metal phthalocyanines (MPc), because it affects the electrical conductivity along with other parameters, for instance substrate temperature, evaporation rate, and post evaporation annealing or the atomic structure of the substrate surface.

Among metal phthalocyanines, the orientation of lead-phthalocyanine molecules (PbPc) deposited as sub-monolayers and thicker layers on different reconstructed GaAs surfaces is presented in the following: The reconstruction of the GaAs surface leads to different atomic surface structures. PbPc is an organic ring-molecule composed of four isoindole groups with a central Pb^{2+} ion standing out of the macrocycle as shown in **Figure 7.1**. The out-of-plane position of the Pb ion gives rise to an optical anisotropy and leads to different possible adsorption geometries such as the Pb ion pointing either toward or away from the surface.

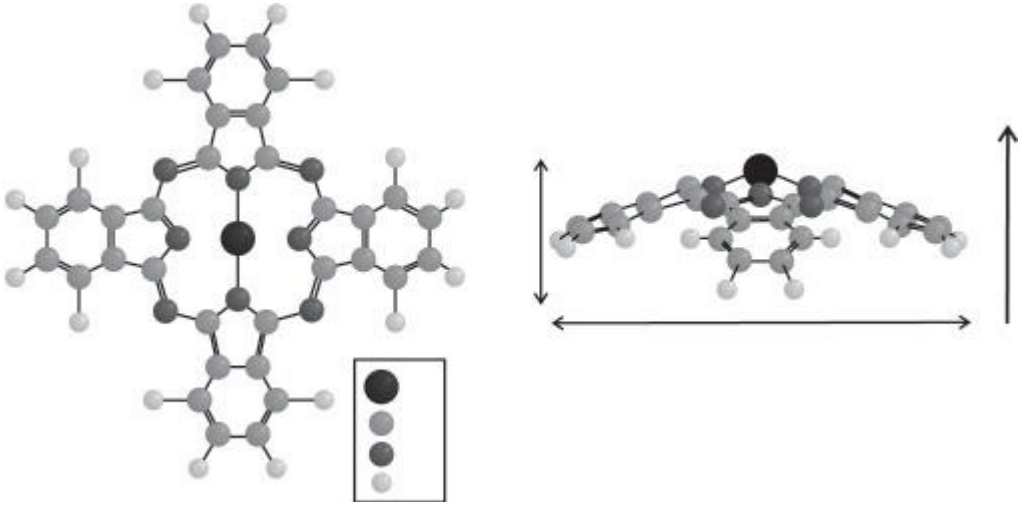

Figure 7.1 Structure model (top and side views) of PbPc.

GaAs $c(4\times4)$ and (2×4) *surface reconstructions*

The GaAs (001) surface offers various stable and well ordered reconstructions with different surface symmetries. Adsorption experiments on these surfaces revealed that the atomic structure of the GaAs (001) surface can influence the adsorption process of smaller organic molecules significantly. Within this investigation, PbPc molecules were deposited on two As-rich GaAs (001) surface reconstructions $c(4\times4)$ and (2×4). For the preparation of reconstructed substrates, GaAs (001) epilayers doped with Si (n = 3.5 × 10^{17} cm^{-3}) were grown by molecular beam epitaxy (MBE). A capping layer of amorphous arsenic protected the surface for contamination-free transfer through air. The clean GaAs (001) / $c(4\times4)$ surface reconstruction is obtained by thermal desorption of the amorphous protection layer at 350 °C (±20 °C) inside an UHV chamber. The (2×4) reconstructed surface is prepared by further annealing up to 430 °C (±20 °C). Reconstruction of the surface is verified by

Low Energy Electron Diffraction (LEED), which shows well ordered *c*(4×4) and (2×4) pattern. [38]

PbPc deposition on GaAs (001)-c(4 x 4)

A thick layer of 20nm PbPc was deposited on the GaAs (001)-c(4x4) with the adsorption process being monitored by RAS. **Figure 7.2(a)** shows the RAS spectra in the range from 1.45 to 5.0 eV with increasing coverage up to about 20 nm. With increasing PbPc coverage, the characteristic RAS signature of the clean *c*(4×4) reconstructed surface disappears. At the same time, new negative anisotropies arise at 1.5, 2.0, 2.6, 3.45, and 4.5 eV, which increase steadily with increasing PbPc layer thickness. Up to this thickness, no saturation of the RAS intensity, at these energies, is observed. For better visualization of the changes in the RAS signature upon adsorption, **Figure 7.2(b)** shows the spectrum calculated from the difference between the spectrum of the clean surface and the spectrum of the thick PbPc layer on the GaAs(001)-*c*(4×4) substrate.[38]

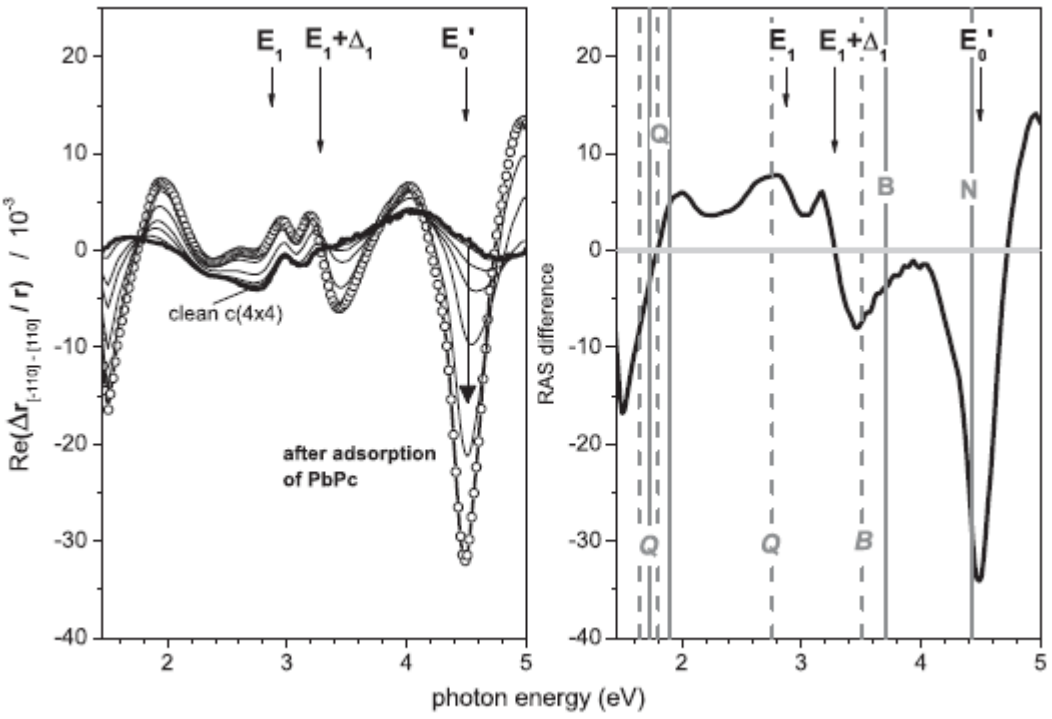

Figure 7. 2 (a)RAS spectra of clean GaAs(001)-*c*(4×4) (black line) and after deposition of 20nm PbPc (open circles). (b) Difference spectra between RAS after adsorption of 20nm PbPc and RAS of clean GaAs(001)-*c*(4×4). Energies of molecular absorption bands of PbPc in vapor phase (solid grey lines) and on quartz glass (dashed grey lines) are shown. The new anisotropies after PbPc adsorption can be attributed to intramolecular transitions. [38]

Since the optical transition moment lies in the plane of the Pc ring, the PbPc is in-plane optically isotropic, but exhibits an optical anisotropy in *z* direction. The observed molecule induced anisotropies, in the RAS spectra, can thus only result from a tilting of the molecules within the layer with respect to the surface normal. Since the intensities of the observed anisotropies increase with increasing coverage, it is assumed that the molecules in all layers are tilted following the first monolayer. STM measurements in sub-monolayer coverage verify this assumption. Figure 3 shows an STM image of a PbPc sub-monolayer on GaAs (001)-*c*(4×4) recorded at a voltage of −2.94 V and current of 0.52 nA.[38]

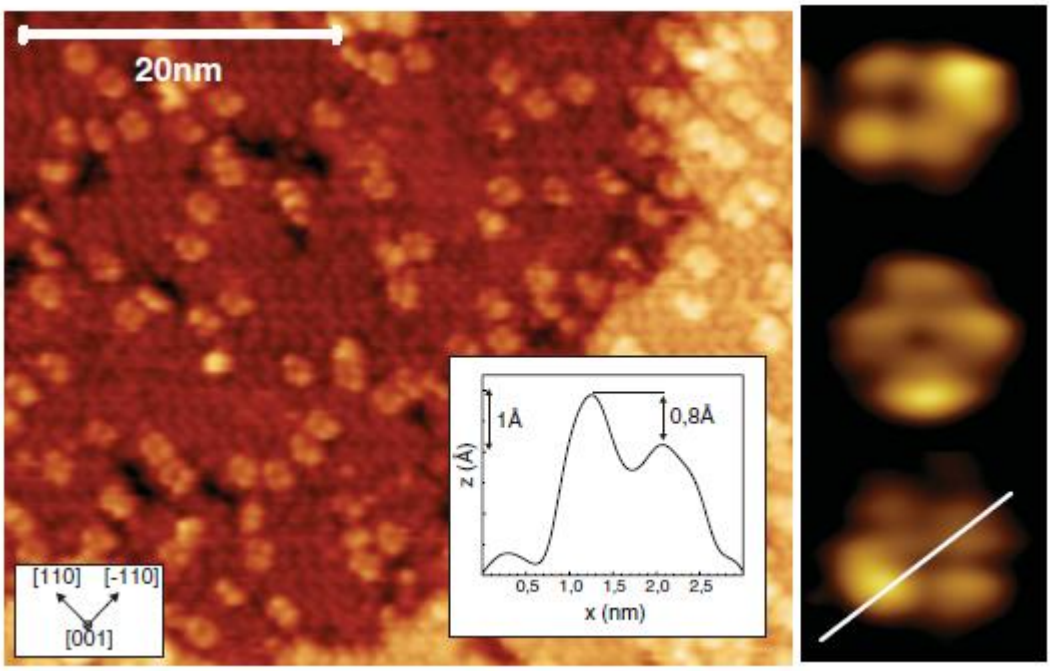

Figure 7.3 (Color online) STM images of single PbPc molecules adsorbed on GaAs (001)-*c*(4×4) (*UG* = −2.94 V). All molecules show a dark center indicating an adsorption geometry with the Pb atom pointing toward the surface. Also, one isoindole group always appears brighter than the others, revealing a tilting angle of approximately 6◦. [38]

The brickstone-like structure observed in the image is typical of the As-As dimer triplets of the *c*(4×4) surface. Besides the structures of the GaAs surface, several objects can be observed in the STM image and each object consists of four smaller protrusions giving rise to a four-leaf clover shape. These bright protrusions are typical for the four isoindole groups of the PbPc molecule. All adsorbed PbPc molecules show a dark center in the middle between the four isoindole groups, a fact meaning that all molecules are adsorbed with the Pb atom pointing toward the *c*(4×4) surface. [38] The three detail images of single adsorbed molecules show that, within one molecule, one isoindole group always appears brighter than the other three isoindole groups. A line scan across such brighter isoindole groups reveals a

height difference of approximately 0.08 nm, as depicted in **Figure 7.3**. The observed contrast difference could result from two different effects: If the PbPc molecules form a chemical bond to the topmost surface layer with one of the isoindole groups, this group could appear brighter due to a charge transfer to the molecule caused by the bond formation. On the other hand, in this case, the optical anisotropy would not increase with the deposition, since only the first molecular layer could form such bonds. However, as such an increase is observed in **Figure 7.3**, only a geometric tilting of the single molecules can explain, that one of the isoindole groups appears brighter, as a result of a true height difference. A quantitative evaluation of 50 molecules, observed in a large scale STM measurement, shows that the molecular plane experiences an average tilting angle of $6^{\circ}(\pm 1.5^{\circ})$ with respect to the surface. A statistical analysis of the azimuthal molecular orientation in the STM image shows that the diagonally opposite isoindole groups of the molecules do not align along the $\left[110\right]$ and $\left[\bar{1}10\right]$ crystalline axes of the GaAs substrate, but more likely 45◦ rotated to them. This observation gives evidence for a preferential orientation within the molecular layer which explains the observed anisotropies in the RAS spectrum. [38]

PbPc deposition on GaAs (001)-(2 x 4)

In a similar way as in the previous case, a thick PbPc layer of approximately 20nm (≈80 monolayers) was deposited on a GaAs (001)-(2x4) substrate and monitored by RAS. **Figure 7.4** shows the RAS spectra recorded for increasing PbPc coverage. The development of the RAS spectra shows a behavior that is significantly different from the spectra recorded at the *c*(4×4) surface. Since the molecule is optically isotropic in the molecular plane, but anisotropic in *z* direction, the RAS spectra in **Figure 7.4** indicate that the adsorbed molecules are oriented with their plane parallel to the substrate surface. Another explanation for the observed optical isotropy of the PbPc layer on GaAs (001)-(2×4) could be domains where the respective anisotropies cancel each other out. However, on a homogenous substrate surface, as in the case of GaAs (2×4), the evolution of such domains seems rather unlikely. Also, an arrangement of differently oriented molecular domains is not known for PbPc. Thus, it is assumed that the observed optical isotropy results from a molecular layer consisting of PbPc molecules with the molecular plane parallel to the surface. [38]

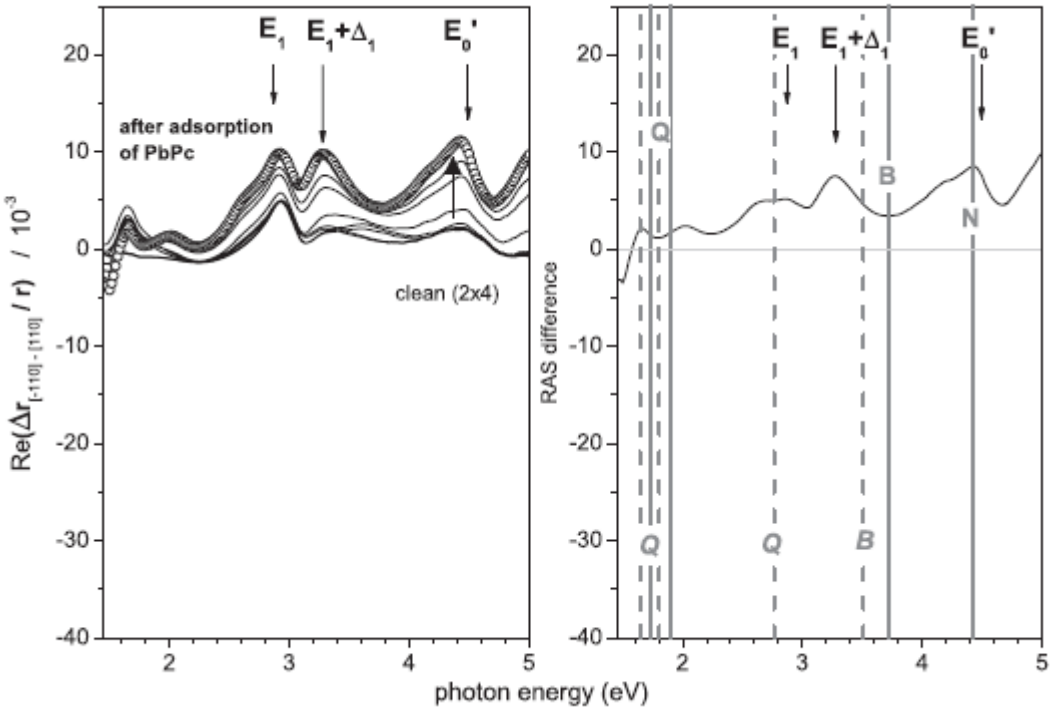

Figure 7.4 (a) RAS spectra of clean GaAs (001)-(2×4) (black line) and after deposition of 20nm PbPc (open circles). (b) Difference spectra between the RAS after adsorption of 20nm PbPc and the clean GaAs (001)-(2×4). Energies of molecular absorption bands of PbPc in vapor phase (solid grey lines) and on quartz glass (dashed grey lines) are shown. After PbPc adsorption, there are no new anisotropies that relate to intramolecular transitions of the adsorbed PbPc.

Once more, STM measurements on a sub-monolayer of PbPc adsorbed on the GaAs (001)-(2×4) surface, shown in **Figure** 7.5, verify the RAS spectra. The image was taken at bias voltage of −4.81 V and current of 0.07 nA. It shows the typical dimer rows of the (2×4) surface. Additionally, bright protrusions can be observed on top of the rows. These protrusions have an average height of 0.27 nm and an average diameter of 1.7 nm. Considering the theoretical height of 0.24 nm and width of 1.4 nm of the domed molecule, these dimensions allow the bright protrusions to be identified as single adsorbed PbPc molecules lying on the surface with their normal perpendicular to the surface. All of the adsorbed PbPc molecules appear with a bright center and no visible substructure of the molecule. The molecular center is the highest point of the molecule as shown in the respective line scan in **Figure** 7.5. These observations differ significantly from the STM measurements at the *c*(4×4) surface and suggest an adsorption geometry with the Pb^{+2} ion above the molecular plane. [38]

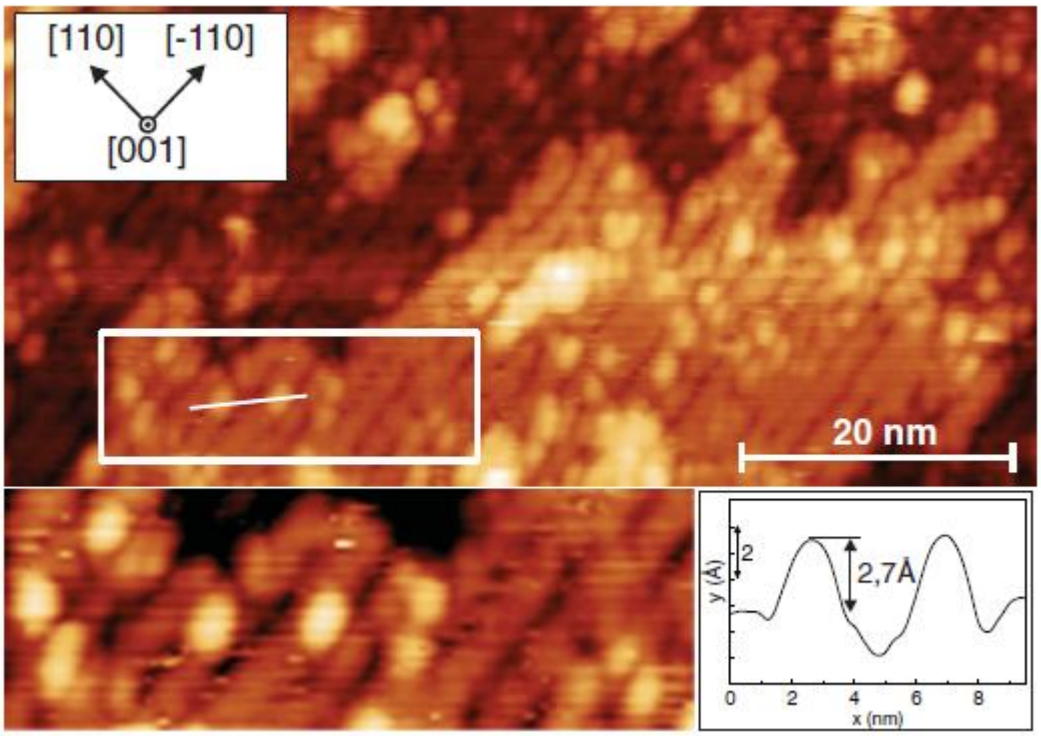

Figure 7.5 STM images of PbPc adsorbed on GaAs(001)-(2×4) (*UG* = −4.81 V). All molecules show a bright center indicating an adsorption geometry with the Pb atom pointing away from the surface. [38]

It is clear now that molecular orientation is affected strongly by the atomic structure of the substrate. In **Figure 7.6,** is presented a growth model that corresponds to molecular orientation of PbPc layers on different GaAs reconstructed surfaces.

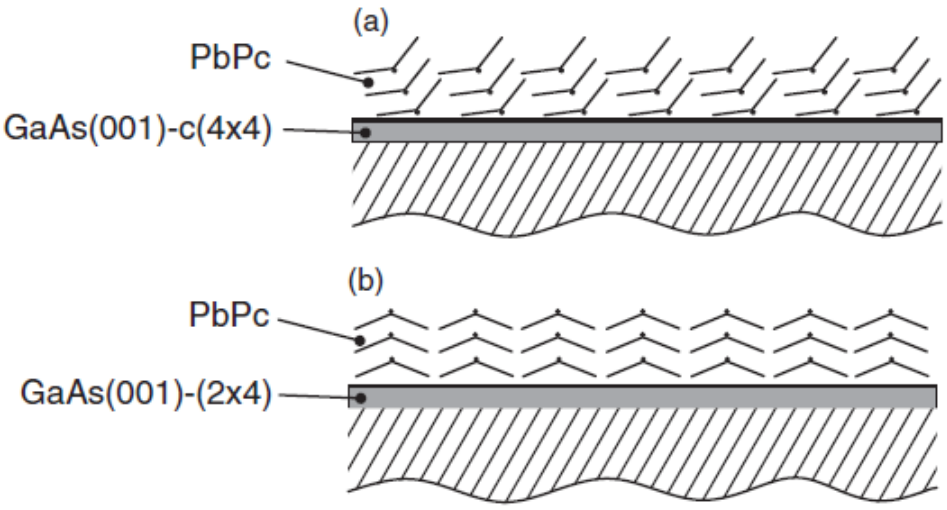

Figure 7.6 Adsorption model for the epitaxial-like growth of thicker PbPc layers on the GaAs(001)-*c*(4×4) (a) and (2×4) (b) reconstruction with tilted and flat lying molecules, respectively. In (a) a higher angle than the experimentally determined 6° was chosen for demonstrative reasons. [38]

Chapter 8 Conclusions

The aim of this thesis was to study the physical properties of organic semiconductors along with organic thin film growth and development of organic solar cells (OSCs) based on these semiconductors. The study includes properties and performance of OSCs.

- **Thin films of organic semiconductor alpha-sexithiophene (a-6T)** were initially grown under high vacuum thermal evaporation on SiO_2 wafers and glass substrates. Atomic force microscopy measurements revealed a rod-like growth and a homogeneous surface structure. The grown structures exhibited different behavior by variation of growth parameters such as substrate pre-deposition chemical etching, substrate temperature during deposition, post deposition annealing, growth rate, etc.

- **The optical properties of alpha-sexithiophene (a-6T) and Fullerene(C_{60}) organic thin films** were studied by UV/VIS Spectroscopy at each stage of the layer stack growth until the fabrication of a complete solar cell. Absorption was enhanced upon completion of the a-6T/C_{60} bi-layer, maintained its value by BCP addition, and was lowered after front contact deposition possibly because of "shadowing" effects of the underlying organic solar cell absorber by the deposited Al-contacts. Thin films of a-6T grown on substrates heated at 90 ^{o}C exhibited lower absorbance possibly because of interruption (or cancellation) of the oriented rod-like growth of a-6T that is assumed to favor absorption.

- **Organic Solar Cells (OSCs) based on alpha-sexithiophene(a-6T)/Fullerene(C_{60}) bi-layer heterojunctions were developed with efficiencies up to 0.76%.** The **a-6T/C_{60} OSCs exhibited high reproducibility** of their I-V characteristics.

- **The basic principles of Organic Solar Cell Operation** have been extensively discussed with detailed diagrams referring to three different examples of the developed a-6T/C_{60} OSCs.

- **Electroreflectance Spectroscopy has been applied in the optical characterization of a-6T/C_{60} OSCs** in a late phase of their life-time. The ER-spectra are indicative of molecular transitions as expected for a-6T/C_{60} bi-layer structure, which points out the high sensitivity and high capacity of modulation techniques for applications in the optical characterization of organic semiconductor materials and devices.

- **Orientation effects of Organic Semiconductor Molecular films** have been studied by combined **Scanning Tunneling Microscopy (STM) and Reflectance Anisotropy Spectroscopy (RAS).** The orientation of PbPc molecules on reconstructed GaAs (001) c(4×4) and (2×4) surfaces was revealed.

Organic solar cells possess a number of advantages, such as low cost, production in large area scale, flexibility in insertion, and controllability through orientation. In order to make the most of organic solar cells, disadvantages such as limited life-times and instabilities should be eliminated, so they become competitive in a commercially production scale. The increase of their electrical performance can be achieved through controlled film structure and the use of novel materials and configurations.

As a future prospect, it would be of interest to investigate the structural changes of organic thin films grown on heated substrates by detailed analysis of the structure by combined STM, RAS, and LEED techniques, as demonstrated in the frame of the present Diploma-thesis. Despite the observed decrease in the optical absorption through heating during growth, there are certain publications indicating the improvement of organic layer structure and increase of device performance. [39]

Bibliography

[1] ***Mechanisms of Growth and Structural Properties of Di-indenoperylene on Metal, Dielectric, and Organic Surfaces,*** XueNa Zhang, PhD-thesis, Universitaet Stuttgart, Stuttgart 2008.

[2] ***Organic Materials for Electronic Devices,*** Lichang Zeng, **,** PhD-thesis, University of Rochester, New York 2010.

[3] ***Principles of solar cells, LEDs, and diodes: the role of the PN junction,*** Adrian Kitai, J. Wiley & Sons (2011) (ISBN: 9781119974550).

[4] ***Order and Symmetries of Sexithiophene within Thin Films Studied by Angle Resolved Photoemission,*** Cynthia Heiner, Diploma-thesis, Freie Universitaet Berlin, Berlin 2004.

[5] ***Efficient oligothiophene: fullerene bulk heterojunction organic photovoltaic cells,*** J. Sakai, T. Taima, K. Saito, Organic Electronics 9 (2008) 582–590.

[6] ***Fullerene chemistry for materials science applications*** M. Prato, J. Mater. Chem. 7(7) (1997) 1097–1109.

[7] ***Organic Solar Cells, Chapter 8. Exciton solar cells,*** Tom J. Savenije, .

[8] ***Growth and Characterization of Sexithiophene Single Crystals,*** G. Horowitz, B. Bachet, A. Yassar, P. Lang, F..Demanze, J.-L. Fave, F. Garnier, Chem. Mater. **7 (**1995) 1337-1341.

[9] ***Atomistic Processes in the Early Stages of Thin-Film Growth,*** Z. Zhang and M. G. Lagally, Science 276 (1997) 377-383.

[10] ***Nucleation and Growth of Thin Films,*** K. Reichelt, Vacuum 38(12) (1988) 1083-1099.

[11] ***Nucleation and growth of thin films,*** J. A. Venables, G. D. T. Spiller and M. Hanbucken, Rep. Prog. Phys. 47 (1984) 399-459.

[12] ***Supramolecular organization in ultra-thin films of α-sexithiophene on silicon dioxide,*** M.A. Loi, E. Da Como, F. Dinnelli, M. Murgia, R. Zamboni, F. Biscarini, M. Muccini, Nature Materials 4 (2005) 81-85.

[13] ***Polymorphism and Charge Transport in Vacuum-Evaporated Sexithiophene Films,*** B. Servet, G. Horowitz, S. Ries, O. Lagorsse, P. Alnot, A. Yassar, F. Deloffre, P. Srivastava, R. Hajlaoui, P. Lang, F. Gamier. *Chem. Mater*. 6(10) (1994) 1809-1815.

[14] ***X-ray diffraction investigations of well-ordered sexithiophene films deposited on flexible substrates***, J.Y. Mua, Z.X. Chenb, T.T.T. Luongb, Journal of Materials Processing Technology 209 (2009) 1491–1494.

[15] ***Weak Epitaxy Growth Affording High-Mobility Thin Films of Disk-Like organic Semiconductors,*** *H. Wang, F. Zhu, J. Yang, Y. Geng, D. Yan,* Adv. Mater. 19 (2007) 2168–2171

[16] ***Standing and flat lying a-6T molecules probed by imaging photoelectron spectroscopy,*** T. Wagner, D. R. Fritz, P. Zeppenfeld, Organic Electronics 12 (2011) 442–446.

[17] ***Molecular and Polymer Semiconductors, Conductors, and Superconductors: Overview,*** D. Fichou and G. Horowitz, Encyclopedia of Materials: Science and Technology, Elsevier Science (2001) pp. 5748-5758 (ISBN: 0-08-0431526).

[18] ***High-Efficient Low-Cost Photovoltaics – Recent Developments,*** V. Petrova-Koch, R. Hezel, A. Goetzberger, Springer Series in Optical Sciences (2009) (ISBN: 978-3-540-79359-5).

[19] ***p-Conjugated Polymers for Photovoltaics,*** A. P. Zoombelt, PhD-thesis, Eindhoven University of Technology, Eindhoven

[20] ***Organic photovoltaics,*** Bernard Kippelen and Jean-Luc Bredas, Energy & Environmental Science 2(3) (2009) 241–332.

[21] ***http://www.heliatek.com***

[22] ***Solar cell efficiency tables (version 41),*** M. A. Green, K. Emery, Y. Hishikawa, W. Warta, E. D. Dunlop, Prog. Photovolt: Res. Appl. 21 (2013) 1–11.

[23] ***Characterization of the PEDOT-PSS system by means of X-ray and ultraviolet photoelectron spectroscopy,*** G. Greczynski, Th. Kugler, W.R. Salaneck , Thin Solid Films 354 (1999) 129-135.

[24] ***The characteristics of the small molecule organic solar cells with PEDOT:PSS/LiF double anode buffer layer system, X***. Xi, Q. Meng, F. Li, Y. Ding, J. Ji, Z. Shi, G. Li, Sol. Energy Mater. Sol. Cells 94 (2010), 623-628.

[25] ***Stability/degradation of polymer solar cells,*** M. Jorgensen, K. Norrman, F. C. Krebs, Sol. Energy Mater. Sol. Cells, 92 (2008), 686-714.

[26] ***Organic solar cells: An overview,*** J. Mater. Res. 19(7) (2004)

[27] ***On the Role of Bathocuproine in Organic Photovoltaic Cells***, H. Gommans, B. Verreet, P. Rand, R. Muller, J. Poortmans, P. Heremans, J. Genoe, Adv. Funct. Mater. 18 (2008) 3686–3691.

[28] ***Organic solar cells: Their developments and potentials,*** N. Yeh, P. Yeh, Renewable and Sustainable Energy Reviews 21 (2013) 421–431.

[29] ***Scanning Probe Microscopy,*** S. M. Salapaka and M. Salapaka, IEEE Control Systems Magazine (2008) 65-81.

[30] ***SPM Training Notebook 2003 Veeco Instruments Inc.***

[31] ***Photoreflectance spectroscopy of low-dimensional semiconductor structures***, J. Misiewicz, R. Sitarek, G. Sek, Opto-Electronics Review 8(1) (2000) 1-24.

[32] ***The Spectroscopy of Semiconductors,*** David G. Seiler and Christopher L. Littler, Academic Press 1992, Vol. 36 (ISBN: 0-12-752136-4).

[33] ***In situ IR, NMR, EPR, and UV/VIS Spectroscopy,*** M. Hunger, J. Weitkamp, Angew. Chem. Int. Ed. 40(16) (2001) 2954-2971

[34] ***MSU Chemistry – UV-Visible Spectroscopy***

[35] **Ultraviolet-Visible (UV-Vis) Spectroscopy – Principle**

[36] ***In-situ optical spectroscopy and electronic properties of pyrrole sub-monolayers on Ga-rich GaAs(001),*** T. Bruhn, M. Ewald, B. O. Fimland, M. Kneissl, N. Esser, P. Vogt, Nanopart. Res. 13 (2011) 5847–5853.

[37] ***Pyrrole adsorption on GaAs(001)-c(4X4): The role of surface defects,*** T. Bruhn, B. O. Fimland, N. Esser, P. Vogt, Phys. Rev. B 85 (2012) 075322.

[38] ***Reconstruction dependent growth of lead phthalocyanine layers on GaAs(001) surfaces,*** L. Riele, T. Bruhn, V. Rackwitz, R. Passmann, B. O. Fimland, N. Esser, P. Vogt, Phys. Rev. B 84 (2011) 205317.

[39] ***Increase in internal quantum efficiency in small molecular oligothiophene: C60 mixed heterojunction solar cells by substrate heating,*** D. Wynands, M. Levichkova, K. Leo, C. Uhrich, G. Schwartz, D. Hildebrandt, M. Pfeiffer, M. Riede, Appl. Phys. Lett. 97 (2010) 073503.

[40] ***Approaching the ultimate open circuit voltage in thiophene based single junction solar cells by applying diindenoperylene as acceptor,*** U. Hörmann, J. Wagner, M. Gruber, A. Opitz, W. Brütting, Phys. Status Solidi RRL 5(7) (2011) 241-243.

KONSTANTINOS T. DESPOTELIS *2013 Curriculum Vitae*

Education

2003-2013	National Technical University of Athens, Greece School of Applied Mathematical & Physical Sciences Department of Physics
Subject area	Photovoltaic Technology Materials Science Optoelectronics & Lasers

Diploma Thesis

	National Technical University of Athens Supervisor: Assist. Professor Dr. Papadimitriou D.
	Technische Universität Berlin Co-supervisor: Dr. Habil. Vogt P. (Work-Group: Prof. Dr. Kneissl M.)
	Hemholtz Zentrum Berlin für Materialien & Energie Co-supervisor: Dr. Fostiropoulos K. (Work-Group: Prof. Dr. Lux-Steiner M.-Ch.)
Entitled	Organic Photovoltaic Technology : Development of organic solar cells based on Thiophene-Fullerene (a-6T/C60) heterojunctions.

Methods	Atomic Force Microscopy Scanning Tunnelling Microscopy Optical Absorption Measurements Modulation Spectroscopy Power Conversion Efficiency Measurements

Publications

[1] K. Despotelis, D. Papadimitriou, K. Fostiropoulos, and M.-Ch. Lux-Steiner, ***Structural, optical and electrical investigation of alpha-sexithiophene thin films and alpha sexithiophene:fullerene based organic solar cells*** in ***Fuelling the future: advances in science and technologies for energy generation, transmission and storage,*** (ed. A. Mendez-Vilas), Brown Walker Press (USA 2012) p. 247-250

[2] S. Kassavetis, T. Mete, K. Despotelis, G. Peschel, M. Toepel, D. Papadimitriou, K. Fostiropoulos, ***Thickness and temperature effect on the properties of alpha-sexithiophene (a-6T) and efficiency of a-6T/C_{60} solar cells,*** 9th Int. Conf. on Nanosciences & Nanotechnologies (NN12), Thessaloniki 2012

Projects

"Si Electron Emitters Fabricated by UV Laser Pulses"

Supervisor: Assistant Professor Zergioti I.

Working Experience

03.2011 – 02.2012 Helmholtz Zentrum Berlin, Wannsee
Organic Solar Cells Group

01.2009 – 01.2010 OTE S.A.
(Hellenic Telecommunications Organization)
Technical Support & Web Services

11.2007 – 12.2007 European Synchrotron Radiation Facility (ESRF)
Grenoble, France
High resolution Diffraction Topography Beamline

Technical & Computer Skills

- General
  Origin, Office (Excel, Word, PowerPoint), Windows

- Programming
  Matlab, Mathematica, Java, Fortran, HTML, WSxM(AFM software)

Languages

- English (Fluent)
  "First Certificate in English", University of Cambridge

- Deutsch (Basic)
  "Zertifikat Deutsch", Goethe Institut